POSITION-SENSORLESS CONTROL OF PERMANENT MAGNET SYNCHRONOUS MACHINES OVER WIDE SPEED RANGE

DISSERTATION

Presented in Partial Fulfillment of the Requirements for the Degree Doctor of Philosophy in the Graduate School of The Ohio State University

By

Song Chi, M.S.E.E

* * * * *

The Ohio State University

2007

Dissertation Committee:

Professor Longya Xu, Adviser

Professor Vadim I. Utkin

Professor Donald G. Kasten

Approved by

Adviser

Graduate Program in Electrical and Computer Engineering

ABSTRACT

Permanent-magnet-synchronous-machine (PMSM) drives have been increasingly applied in a variety of industrial applications which require fast dynamic response and accurate control over wide speed ranges. However, there still exist challenges to design position-sensorless vector control of PMSM operating in a wide speed range, which covers both constant-torque and constant-power region. Thus, two control techniques are proposed in this dissertation for PMSM drives, namely flux-weakening control incorporating speed regulation and sliding mode observer with feedback of equivalent control. The research objectives are to extend the operating speed range of the PMSM drive system and improve its control robustness and adaptability to variations of operating conditions as well as dynamic performance.

First, a robust flux-weakening control scheme of PMSM is studied. With a novel current control strategy, i.e., adjusting the direct-axis voltage but fixing the applied quadrature-axis voltage of PMSM at a specific value, the demagnetizing stator current required for the flux-weakening operation can be automatically generated based on the inherent cross-coupling effects in PMSM between its direct-axis and quadrature-axis current in the synchronous reference frame. The proposed control scheme is able to achieve both flux-weakening control and speed regulation simultaneously by using only

one speed/flux-weakening controller without the knowledge of accurate machine parameters and dc bus voltage of power inverter. Moreover, no saturation of current regulators occurs under any load conditions, resulting in control robustness in the flux-weakening region.

Secondly, a sliding mode observer is developed for estimating rotor position of PMSM without saliency, by means of which position-sensorless vector control can be achieved. A concept of feedback of equivalent control is applied to extend the operating range of sliding mode observer and improve its angle-estimation performance. Compared to conventional sliding mode observers, the proposed one features the flexibility to design parameters of sliding mode observer operating in a wide speed range. The estimation error of rotor position can be reduced in the low-speed range and fast convergence of the observer guaranteed in the high-speed range by properly selecting the feedback gain of equivalent control. In addition, a flux-based sliding mode observer with adaptive feedback gain is investigated. The constant magnitude of equivalent control makes it easier to design the switching gain of discontinuous control in the sliding mode observer. As a result, the problematic chattering phenomenon normally prevailing at low speeds due to high switching gains can be mitigated or even eliminated.

The feasibility and effectiveness of the control techniques addressed in this dissertation are verified by both computer simulation and experimental results.

Dedicated to my wife and my parents

ACKNOWLEDGMENTS

I wish to express my deep gratitude to my adviser, Professor Longya Xu, for his guidance, encouragement, and support during my graduate study. His creative thinking, knowledge and expertise on electric machines and controls were the "power supply" and "feedback" of my conducted researches. So will be in my future professional career.

I would like to thank Professor Vadim Utkin and Professor Donald Kasten for being committee members of my graduate study. They provided me many insightful comments and constructive suggestions in the review of my research proposal and dissertation. My special thanks go to Professor Stephen A. Sebo as well for his invaluable advice in my Candidacy Exam.

I am also grateful to Dr. Zheng Zhang and all other motor group members of AEA, Whirlpool for their kindly help during my experimental data collection.

My thanks are extended to my fellow colleagues majoring in electrical engineering, who built an academic and friendly research environment that made my study at Ohio State most enjoyable. I cherish the friendship with them since my first arrival at this continent and meeting with: Mr. J. Hu, Dr. J. Liu, Dr. J. Li, Dr. M. Dai, Dr. W. Lu, Dr. S. Li, Dr. M. Konghirun, Dr. M. Comanescu, Dr. R. Esmaili, Dr. X. Liu, Ms. D. Das, Ms. Y. Zhang and Mr. B. Guan.

Last but not least, I am always indebted to all my family members, especially my parents and my wife, for their endless support and love. I greatly appreciate the sacrifices and understanding of my beloved wife Xiaoyan during my struggling years, without which the completion of my study would not have been possible.

VITA

June 1993…………………………...………..……..……....B.S. Electrical Engineering

Northeast University (NEU)
Shenyang, China

July 1993 – February 2002 …………..……………...………....Engineer and Researcher

Automation Research Institute of
Metallurgical Industry (ARIM)
Beijing, China

June 2000……………………….……..…..………....…M.S. Electrical Engineering

Tsinghua University, China

April 2002 – June 2006 …………...…………Graduate Research and Teaching Associate

The Ohio State University
Columbus, Ohio

July 2006 – present…………...…………………………………………...……Engineer

Whirlpool Corporation
Benton Harbor, Michigan

FIELDS OF STUDY

Major Field: Electrical Engineering

TABLE OF CONTENTS

LIST OF TABLES

Table Page

LIST OF FIGURES

NOMENCLATURE

$e_{\alpha s}$	α-axis stator back-EMF in the stationary reference frame
$e_{\beta s}$	β-axis stator back-EMF in the stationary reference frame
f_c	Cutoff frequency of LPF
$i_{\alpha s}$	Instantaneous stator current of phase-A
i_{bs}	Instantaneous stator current of phase-B
i_{cs}	Instantaneous stator current of phase-C
$i_{\alpha s}$	α-axis stator current in the stationary reference frame
$i_{\beta s}$	β-axis stator current in the stationary reference frame
i_{ds}	Direct-axis stator current in the rotor reference frame
i_{qs}	Quadrature-axis stator current in the rotor reference frame
k_i	Integral gain of current regulators
k_p	Proportional gain of current regulators
k_{i_FWC}	Integral gain of SFWC
k_{p_FWC}	Proportional gain of SFWC
k	Switching gain for the discontinuous control in SMO
k_s	Slope of saturation function
l	Feedback gain of equivalent control in SMO
$v_{\alpha s}$	α-axis stator voltage in the stationary reference frame

$v_{\beta s}$	β-axis stator voltage in the stationary reference frame
v_{ds}	Direct-axis stator voltage in the rotor reference frame
v_{qs}	Quadrature-axis stator voltage in the rotor reference frame
λ_m	Rotor permanent-magnet flux
ω_c	Cutoff angular velocity
ω_r	Rotor angular velocity
θ_r	Rotor position angle
$z_{\alpha s}$	α-axis discontinuous control in SMO
$z_{\beta s}$	β-axis discontinuous control in SMO
$z_{eq\alpha}$	α-axis equivalent control in SMO
$z_{eq\beta}$	β-axis equivalent control in SMO
μ	Time constant of LPF
E_0	Width of boundary layer
I	Steady-state value of variable i
L_d	Direct-axis stator inductance of PMSM
L_{md}	Direct-axis magnetizing inductance of PMSM
L_q	Quadrature-axis magnetizing inductance of PMSM
L_{mq}	Quadrature-axis magnetizing inductance of PMSM
L_{ms}	Stator magnetizing inductance of PMSM
L_s	Stator inductance of PMSM

L_{ls}	Stator leakage inductance of PMSM
P	Number of pole pairs
R_s	Stator resistance
T	Transformation operation matrix
T_s	Sampling period
V	Steady-state value of variable v
$\boldsymbol{f}_{abcs}$, or $\vec{f}_{abcs}$	Vector variable f in the stationary reference frame
Δf	Deviation of variable f in small-signal model
r_{abcs}	Stator resistance matrix
L_{abcs}	Stator inductance matrix
$\hat{f}_{abcs}$, or $\vec{\hat{f}}_{abcs}$	Estimate of vector variable f

LIST OF ABBREVIATIONS

ac	alternating current
dc	direct current
μP	microprocessor
rpm	revolution per minute
s	second
ADC	Analog-to-Digital Converter
ANN	Artificial Neural Network
ASIC	Application Specific Integrated Circuit
Back-EMF	Back Electromagnetic Force
BP	Back Propagation
CPPM	Consequent-Pole Permanent Magnet
DD	Direct Drive
DSP	Digital Signal Processor
EKF	Extended Kalman Filter
EMI	Electro-Magnetic Interference
EV	Electrical Vehicle
FF	Feedforward
FFT	Fast Fourier Transform

HEV	Hybrid Electrical Vehicle
IPM	Interior Permanent Magnet motor
LPF	Low-Pass Filter
MRAC	Model Reference Adaptive Control
OSU	The Ohio State University
PC	Personal Computer
PI	Proportional-Integral
PLL	Phase-Locked Loop
PM	Permanent Magnet
PMSM	Permanent Magnet Synchronous Machine
PWM	Pulse Width Modulation
SFWC	Speed/Flux-Weakening Controller
SI	International System of Units
SMO	Sliding Mode Observer
SPM	Surface-mounted Permanent Magnet motor
SVPWM	Space-Vector Pulse Width Modulation
VC	Vector Control

CHAPTER 1

INTRODUCTION

1.1 Background of the Study

Electrical ac machines have been playing an important role in industry progress during the last few decades. All kinds of electrical ac drives have been developed and applied, which serve to drive manufacturing facilities such as conveyor belts, robot arms, cranes, steel process lines, paper mills, waste water treatment and so on. With the advances in power semiconductor devices, converter topologies, microprocessors, application specific ICs (ASIC) and computer-aided design techniques since 1980s, ac drives are currently making tremendous impact in the area of variable speed motor control systems [1-7].

Among the ac drives, permanent magnet synchronous machine (PMSM) drives have been increasingly applied in a wide variety of industrial applications. The reason comes from the advantages of PMSM: high power density and efficiency, high torque to inertia ratio, and high reliability. Recently, the continuous cost reduction of magnetic materials with high energy density and coercitivity (e.g., samarium cobalt and neodymium-boron iron) makes the ac drives based on PMSM more attractive and competitive. In the high-performance applications, the PMSM drives are ready to meet sophisticated requirements such as fast dynamic response, high power factor and wide operating speed range. This has opened up new possibilities for large-scale application of PMSM. Consequently, a continuous increase in the use of PMSM drives will surely be witnessed in the near future [3, 5, 6].

In general, PM synchronous machines with approximately sinusoidal back electromotive force (i.e., back-EMF) can be broadly categorized into two types: 1) interior (or buried) permanent magnet motors (IPM) and 2) surface-mounted permanent magnet motors (SPM). In the first category, magnets are buried inside the rotor. Due to this interior-permanent structure, the equivalent air gap is not uniform and it makes saliency effect obvious, although the IPM motor physically looks like a smooth-air-gap machine. As a result, the quadrature-axis synchronous inductance of IPM is larger than its direct-axis inductance, i.e., $L_q > L_d$, which significantly changes the torque production mechanism. Therefore, both magnetic and reluctance torque can be produced by IPM motor. In the second category, the magnets are mounted on the surface of the rotor. Because the incremental permeability of the magnets is 1.02-1.20 relative to external fields, the magnets have high reluctance and accordingly the SPM motor can be considered to have a large and uniform effective air gap. This property makes the saliency effect negligible. Thus the quadrature-axis synchronous inductance of SPM equals its direct-axis inductance, i.e., $L_q = L_d$. As a result, only magnet torque can be produced by SPM motor, which arises from the interaction of the magnet flux and the quadrature-axis current component (i.e., i_{sq}) of stator currents. Compared to SPM motors, the IPM motor has a mechanically robust and solid structure since the magnets are physically contained and protected. In addition, due to their reluctance torque production, the IPM motors are more suitable for traction applications which requires constant power output at high speeds over a wide range [1].

With the rapid development of microprocessors (μC) and digital signal processors (DSP), vector control is becoming a common technique for PMSM drive systems, especially in low-cost applications such as home appliance and machine tools. The vector control (or called field-oriented control) of ac machines was introduced in the late 1960s by Blaschke, Hasse, and Leonhard in Germany. Following their pioneering work, this technique, allowing for the quick torque response of ac machines similar to that of dc machines, has achieved a high degree of maturity and become popular in a broad variety of applications. It is also widely applied in many areas where servo-like high performance plays a secondary role to reliability and energy savings.

To achieve the field-oriented control of PMSM, knowledge of the rotor position is required. Usually the rotor position is measured by a shaft encoder, resolver, or Hall sensors. However, the presence of such sensors not only increases the cost and encumbrance of the overall drive system but also reduces its control robustness and reliability. Furthermore, it might be difficult to install and maintain a position sensor due to the limited assembly space and rigid working environment with severe vibration and/or high temperature. Therefore, various position-sensorless control schemes have been developed for the estimation of rotor position and speed, especially during the last decade [8-12].

The advantages of PM machines recently make them highly attractive candidates for "direct drive" applications, such as hybrid electrical vehicles (HEV) or electrical vehicles (EV) and washing machines, which are illustrated in Figure 1.1. By this technology, the rotating working unit of a direct drive system, such as the basket or drum of a washing machine, is coupled to the motor shaft without transmission assembly, which may include clutches, belts, pulleys and/or gearboxes. The power is directly delivered to the working unit by the motor. The concept of direct drive enables the high dynamic response, increased efficiency, low acoustic noise, and long lifetime due to the elimination of the transmission components. Such direct drive systems normally require large shaft torque at standstill (i.e., zero speed) and low speeds as well as constant output power over wide speed range. In order to meet such requirements, the PM machines are designed to operate not only in the constant torque mode when their speed is below the base (or rated) speed but also in the constant power mode when above the base speed. In this way, the cost and size of overall drive system can be significantly reduced. The constant torque operation of PM motor can be easily achieved by conventional vector control. However, when the speed is above the base speed, the back-EMF of PM motor is larger than the line voltage and then the motor suffers from the difficulty to continuously produce torque due to voltage and current constraints. Thanks to the flux-weakening technology, the operating speed range can be extended by applying negative magnetizing current component to weaken the air-gap flux [13, 14].

Extensive researches on PMSM drive systems in laboratories as well as at industrial sites have been conducted and various sensorless and flux-weakening control methods have been developed so far. However, within the large volume of such researches, few practical solutions have been given to the sensorless control of PMSM over wide speed range including flux-weakening region.

This dissertation will address issues of control techniques with special attention to wide speed-range operation of PM synchronous machines.

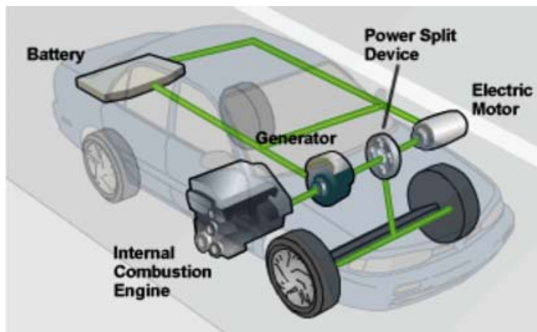

(a)

(b)

Figure 1.1: Applications of PMSM direct drive system:
(a) HEV, (b) washing machine.

1.2 Objectives of the Study

This research is expected to contribute new practical techniques to the design of sensorless vector control of PMSM over wide speed range, covering both constant-torque and constant-power region under current and voltage constraints imposed by power inverter. On this purpose, an experimental PMSM drive system was designed and built at The Ohio State University (OSU). In the drive system, both an IPM and an SPM motor were used as the control target to verify the proposed control algorithms.

The main objectives of this research work include:

- Develop a robust flux-weakening control scheme that is easily implemented in a low-cost DSP-based digital controller.
- Investigate the flux-weakening control scheme in terms of efficiency and stability of operation at high speeds.
- Develop an observer for estimating the rotor position angle of SPM motor that is able to work over wide speed range.
- Investigate the observer in terms of estimation error, convergence and adaptive capability.

1.3 Dissertation Organization

The dissertation is organized as follows:

Chapter 1 introduces the background for this dissertation research, the significance of the study and the research objectives.

Chapter 2 reviews the state of the art and recent developments, in general, of flux weakening and position-sensorless control of PM machines.

Chapter 3 addresses the mathematical modeling and control strategies of two major varieties of permanent-magnet synchronous machines. Moreover, basic operation principles of PM synchronous machines are discussed whereupon vector control is briefly investigated.

Chapter 4 presents a robust flux-weakening control scheme of PMSM integrating speed regulation. The main aspects discussed for the developed speed/flux-weakening controller include: linear relationship between direct- and quadrature-axis current, small-signal method used to investigate the flux and torque controllability, current vector trajectories in the rotor reference frame under various scenarios, and optimum design of the speed/flux-weakening controller based on selection of a voltage constant.

Chapter 5 proposes a sliding mode technique for position-sensorless control of PMSM over wide speed range. A control concept of feedback of equivalent control is highlighted and the selection of feedback gain discussed for the speed adaptation. Existence condition of sliding mode and proof of its stability will be dealt with by using Lyapunov method.

Chapter 6 gives the overall conclusions of the research and recommendations for future work.

CHAPTER 2

LITERATURE REVIEW

Over the years, considerable development efforts have been devoted to the application of various classes of advanced control techniques to PMSM drives. More specially, there have been many literatures focused on the position-sensorless control and flux weakening operation of PM machines, which relate to state observers, sliding mode, adaptive control, fuzzy logic, expansion of speed range, optimum design of PM motor, and etc. The following sections will briefly review the state of the art and recent developments for each of the above techniques.

2.1 Flux-Weakening Control of PM Synchronous Machines

As discussed previously, PM synchronous machines are attractive and desirable for ac drives due to the advantages of high power density and efficiency. However, the fixed field excitation provided by permanent magnets limits the controllability and high-speed capability of PMSM drives. Moreover, the current and voltage constraints of power inverter result in difficulties of current regulation and the decreased torque production as speed increases. To extend their operating speed ranges, PM motors are generally operated in such a way that the armature currents with large negative direct-axis component partially demagnetize the magnetic field and thus weaken the air-gap flux achieving the so-called flux weakening [15-17]. However, this approach involves the risk of demagnetizing the permanent magnets irreversibly and generates significant heat due to copper losses of stator windings. If the ambient temperature and the reverse flux are sufficiently high to move the magnetic operating point near or below the knee of normal demagnetization point, the permanent magnets will never be able to recoil back to the original operating point after the demagnetizing current is removed. Therefore, without demagnetizing the magnets, how to fully utilize the limited current and voltage capability of power inverter to extend the speed range of PMSM is always of great interest as well as a challenge [18].

To avoid the irreversible demagnetization of permanent magnets, many solutions have been reported in terms of various rotor structures of PM motors [18-20]. L. Xu et al. proposed a new design concept of PM machine for flux-weakening operation, which was aimed at minimizing the required demagnetizing current for a given level of flux weakening. By the way of altering the flux path of magnets, not only was the copper losses reduced but also the risk of damaging the permanent magnets eliminated [18].

Tapia et al. explored a magnetic structure termed the consequent-pole PM (CPPM) machine which had inherent field weakening capability. It was concluded that the machine combined the fixed excitation of rare-earth permanent magnet with the variable flux given by a field winding located on the stator, and thus the air-gap flux could be controlled over a wide range with minimum conduction losses and little demagnetization risk for the PM pieces [19].

In addition, comprehensive design methods were reviewed in [19]: 1) connecting groups of the stator winding in different configurations by which the induced voltage could be adjusted accordingly; 2) a stator-mounted PMSM where the flux weakening was operated by changing the reluctance path of the magnets; 3) using a field winding to add or subtract flux from the magnets; and 4) a PM motor with two-section rotor with field weakening where the reluctance of the direct-axis flux path was varied with changing the ratio between each section.

Soong and Miller concluded that for the maximum torque field-weakening control, the optimal high-saliency interior PM motor design was most promising for applications requiring a wide field-weakening range [20].

The above efforts were made on the different types of PM motor design, which obviously resulted in the increased manufacturing cost due to the additional windings and/or complicated rotor structure. On the other hand, many control strategies and algorithms have been developed for flux-weakening operation of PMSM and published during the last decade [21-31].

Macminn and Jahns presented two control techniques to enhance the performance of IPM drives over an extended speed range. Although the proposed feedforward current regulator compensation and flux-weakening control algorithms combine to improve the torque production capability of the IPM motor at high speeds, full effectiveness of the techniques strongly depends on accurate machine parameters used in control functions.

And the control performance is degraded gracefully as errors between the programmed and actual parameters are increased [21].

Sebastian and Slemon [22] investigated the maximum torque per ampere (MTPA) operation of PMSM up to a break-point speed with optimum alignment of the stator and magnet field. Operation at higher speeds with reduced torque was achieved by the adjustment of current angle to reduce the effective magnet flux, i.e., the equivalent of field weakening.

Dhaoudi and Mohan researched a current-regulated flux-weakening method by introducing a negative current component to create direct-axis flux in opposition to that of the rotor flux by magnets, resulting in a reduced air-gap flux. This armature reaction effect was used to extend the operating speed range of PMSM and relieve the current regulator from saturation that is subject to occurring at high speeds [23]. Similarly, not only a current vector control to expand the operating limits under the constant inverter capacity but also the improvement by the feedforward decoupling compensation were proposed in [24, 25] respectively by Morimoto et al. In these flux-weakening schemes, the demagnetizing current command was calculated based on the mathematical model of the PM motor and, consequently, the performance of the PMSM drive system was strongly dependent on the motor parameters and sensitive to operating conditions.

Sudhoff et al set forth a flux-weakening control for SPM motors, which was relatively simple and did not require the knowledge of the machine and inverter parameters. Moreover, the miscellaneous voltage drops such as semiconductors voltage drops, current sensor voltage drops, and those caused by the dead time in the switching strategy were automatically included into the calculation of the direct-axis current. The calculated direct-axis current command, i.e., demagnetizing current command, was proportional to the current error of quadrature-axis current. Unfortunately, because the proposed feedback control is proportional, there always exists control error. Even though the error can be reduced by selecting high feedback gain, the control instability of the overall drive system would be a problem [26].

Sozer and Torrey [27] presented an approach for adaptive control of the surface mounted PM motor over its entire speed range. The adaptive flux-weakening scheme was able to determine the right amount of direct-axis current without knowing the load torque and inverter parameters. The level of demagnetizing current was obtained by using the current error between the actual and reference currents that gave a measure of inverter saturation. Integration of this error by an additional integrator with a forgetting factor drove the direct-axis current.

Y. S. Kim et al, J. M. Kim et al and J. H. Song et al proposed a flux-weakening control method based on a voltage regulator using the voltage error signals between the allowable maximum output voltage and the voltage command [28-30]. The output of the voltage regulator determines the required amount of the demagnetizing current. In addition, the onset of flux weakening could be adjusted to prevent the saturation of the current regulators required by the vector control of PM motors.

Both current-error- and voltage-error-based flux-weakening control methods require an additional PI regulator or integrator to generate the demagnetizing current command, which, in turn, causes the increased complexity of the overall control system. Furthermore, the added controller could only operate properly under well-tuned conditions, which is not easily reached.

Conventionally, two current regulators of the direct- and quadrature-axis current in the rotating reference frame are required to achieve the torque and flux control simultaneously as in [31]. Unfortunately the direct- and quadrature-axis current cannot be truly controlled independently due to their cross-coupling effects inside the PM motor. The cross-coupling effects will increase with rotor speed and become dominant in the high-speed range. As a result, the dynamic performance of current and torque response is degraded at high speeds without decoupling control.

2.2 Position-Sensorless Control of PM Synchronous Machines

To control a PM motor with fast dynamic response, accurate speed regulation and high efficiency, it is necessary to know the rotor position for the implementation of vector control, or field-oriented control. Traditionally the rotor position is obtained from a shaft-mounted optical encoder, revolver or Hall sensors. However, it is desirable to eliminate such sensors in PMSM drives to reduce system costs and total hardware complexity, to increase the mechanical robustness and reliability, to reduce the maintenance requirements, to ensure that the inertia of the system is not increased, and to have noise immunity [32-63]. For these purposes, researches have been widely conducted in the past two decades. Several main techniques of sensorless control of PMSM drives have been extensively studied, which can be categorized into the following:

1) Flux estimation based on the voltage model of PMSM [32, 33];

2) Estimators based on inductance variation due to geometrical and saturation effects [34-40];

3) State observers [41-46];

4) Extended Kalman filters [47-49];

5) Model reference adaptive schemes (MRAS) [50-53];

6) Sliding mode observers [54-63]; and

7) Fuzzy-logic, neural network and artificial intelligence-based estimators [64-66].

Both Wu et al and Xu et al respectively presented a flux estimator based on the voltage model of PMSM. Two line-to-line voltages and two stator currents were measured and the stator flux linkage vector was obtained by integrating the terminal voltages minus the stator ohmic drops. The angle of the stator flux was then calculated and the rotor speed derived from the first-time derivative of the flux angle. It is obvious that the control performance of the PMSM drive adopting this method depends greatly on the accuracy of the estimated stator flux-linkage components, which, however, depend on the accuracy of the measured voltages and currents, and also on the selected integration algorithm. Although many drift compensation approaches have been reported so far, the pure integration in the software or hardware circuits can still be problematic at low frequencies, where the stator voltage becomes very small and are dominated by the ohmic voltage drops [32, 33].

The rotor position can be estimated by using inductance variations due to magnetic saturation and/or geometrical effects of PMSM. Techniques based on this idea are playing an important role on the sensorless control of ac drives requiring standstill and low-speed operation with full load. An “INFORM” method was proposed by Schroedl, which was based on real-time inductance measurements using saliency and saturation effects. During a short time interval, the “complex INFORM reactance” was calculated for estimating flux angle [34]. On the other hand, Corley and Lorenz investigated a high-frequency signal injection method in such a way that carrier-frequency voltages were applied to the stator windings of PMSM, producing high-frequency currents of which the magnitude varies with rotor position. The sensed currents were then processed with a heterodyning technique that produced a signal approximately proportional to the difference between the actual and the estimated rotor position [35]. However, all these methods require high-precision and high-bandwidth (fast) measurement and fast signal processing capability, which inevitably increase the complexity and cost of control system. The injected high-frequency voltages may also cause more torque ripple, shaft vibration and audible noises. Furthermore, due to the constraints of the maximum PWM switching frequency and the geometry of rotor, such methods usually work to some specific motors in the limited operating speed range, i.e., only at standstill and low speeds.

Classical control designs based on state equations of linear time-invariant system have received widespread research and development interests. Lim et al proposed a pair of cascaded Luenberger observers, of which the faster one was for the estimation of rotor position using current measurements and the slower one for estimating angular velocity. A linearized augmented motor model for the fast position observer was considered approximately time-invariant within one sample period of the slower velocity observer on the assumption that the system mechanical time constant is much larger than the electrical one. Kim et al also proposed a Luenberger observer which provided a simple estimation process as a kind of reduced-order state observer to obtain back-EMF information. Consequently, the rotor position angle and speed could be obtained from the machine voltage equations in the stationary reference frame. In addition, a non-linear state-feedback linearization for full-order observer and a D-state observer were introduced in [44] and [46] respectively to attenuate parameter variations and external disturbances to a certain extent. However, the poles and zeros of system transfer function could vary due to parameter variations, and model uncertainties may degrade the performances of these observers.

The Extended Kalman Filter (EKF) is able to provide optimum filtering of the noises in measurement and inside the system if the covariances of these noises are known. It is an optimal stochastic observer in the least-square sense for estimating the states of dynamic non-linear systems. Hence it is a viable candidate for the on-line determination of the rotor position and speed of PMSM [47-49]. However, none of the practical industry applications of EKF-based sensorless PMSM control has been reported due to the technical difficulties, which may include: 1) detailed dynamic model of PMSM with initial rotor position; 2) formulation of the EKF model in closed form; 3) discrete-time model of the overall controlled system and details of power electronics circuitry and implementation; 4) complex methods for correcting the rotor flux variations; 5) initial speed position convergence; 6) computational expense, specific design, tuning criteria and so on.

Adaptive control seems to be the most promising one of various modern control strategies reported in the literatures as [50-53]. Cerruto et al proposed an adaptive control scheme, namely Model Reference Adaptive Control (MRAC), characterized by a reduced amount of computation. The MRAC approach was able to compensate the variations of the system parameters, such as inertia and torque constant. A disturbance torque observer was employed to balance the required load torque and reduce the complexity of the adaptive algorithm. Baik et al investigated the MRAC-based adaptation mechanisms for the estimation of slowly varying parameters using the Lyapunov stability theory. A linearized and decoupled model was derived, which includes the influence of inertia variation and speed measurement error on the nonlinear speed control of PMSM. Researches carried out in these references show that the adaptive control can improve the robustness of PMSM drives. However, system identification and state estimation require complex computations. Moreover, they are based on the assumption that the structure of the system model is specified and especially motor/load dynamics are well understood, which cannot be guaranteed in practice.

Among the existing sensorless approaches, sliding mode has been recognized as the prospective control methodology for electric machines. Previous studies show that sliding mode observers (SMO) have attractive advantages of robustness to disturbances and low sensitivity to parameter variations [54-63].

The concept of equivalent control of discontinuous components in sliding mode is introduced by professor Utkin, which plays a key role on the theory of sliding mode. It originates from the observation of physical systems, providing an additional source of information to the control design and reducing the complexity of the overall system. It is concluded that sliding mode techniques combined with asymptotic observers are considered as extension of the traditional control techniques like hysteresis control [2].

Peixoto et al proposed a speed control for a PMSM drive system. In the control, the sliding mode was used to estimate the induced back-EMF, rotor position and speed. A sliding mode observer was built based on the electrical dynamic equations. The back-

EMF information was obtained from the filtered switching signals relative to current estimation error. It can be seen that it could be a challenging job to design the switching gain over a wide speed range based on this observer model [56].

Han et al presented a method to estimate the speed of PMSM using sliding mode observer. Lyapunov functions were chosen for determining the adaptive law for the speed and stator resistance estimator. It is found that the existence condition of sliding mode cannot be easily guaranteed for the convergence by this method. Also the integration of rotor angular velocity may bring more error on the estimated rotor position angle [57].

Elbuluk et al investigated a sliding mode observer for estimating the rotor position and speed of PMSM. Instead of directly using filtered switching signals by a low-pass filter, an observer was designed to undertake the filtering task for the estimated back-EMF. It is stated that the observer has the structure of an extended Kalman filter and is expected to have high filtering properties [62]. Unfortunately, no experimental results were presented. Similar technique has also been discussed in [2].

Kang et al proposed an iterative sliding mode observer for the estimation of back-EMF and thus the rotor position of PMSM in high-speed range. By iterating the conventional SMO recursively several times within a sample period of PI current regulators, chatting components superimposed on the estimated currents and back-EMF were reduced. However, this method doesn’t help much for the low-speed operation [63].

In addition, fuzzy-logic, neural network and artificial intelligence-based estimators have been presented for the sensorless control of PMSM [64-66]. These methods use artificial neural network (ANN), diagonally recurrent neural network or fuzzy-neural network combined with adaptive technique. They are completely different from traditional model-based estimation methods as discussed above. For a PMSM drive system, to some degree, the plant model of PMSM is normally known with neglect of the nonlinear factors such as saturation. This approximation is acceptable in most industry applications. On this point of view, artificially intelligent estimators provide a fresh alternative to the sensorless control of PMSM. But the parameters in the machine model and their variation with environmental changes may not be easily known accurately. In order to make such intelligent estimators practical and effective for real-time implementation, there are still many aspects to consider. For example, as a normal multilayer feedforward artificial neural network (FANN) deals with static problems, inherently, the conventional static training algorithm known as error back propagation (BP) severely restricts its use for applications requiring real-time adaptation [66]. Moreover, artificially intelligent estimators are relatively complicated and require large computation time, which must be implemented in a high-performance and expensive microprocessor or DSP that is not suitable for cost-effective drive systems.

2.3 Summary

Two major aspects on the control issues of PM machines have been reviewed comprehensively in terms of flux weakening and position-sensorless control. The related techniques are briefly discussed and their double sides, i.e., pros and cons, provided to outline the state of the art and potential trends of technology development in these areas. Moreover, many control fundamentals and basic ideas are introduced meanwhile in this chapter on which the conducted dissertation studies are based.

CHAPTER 3

MODELING, OPERATION AND CONTROL OF PERMANENT MAGNET SYNCHRONOUS MACHINES

The aim of this chapter is to systemically review mathematic models of the two major varieties of permanent-magnet synchronous machines, namely interior PM motors and surface-mounted PM motors, before proceeding to design control and observation algorithms for them. Transformations of variables are used to deal with the time-varying machine inductances, referring to the coefficients of differential equations (e.g., voltage equations) that describe the performance and behavior of the PM motors. Moreover, basic operation principles of PM synchronous machines are discussed whereupon vector control is briefly investigated. All the analysis and control methods presented in later chapters are based on these models.

3.1 Mathematical Model of PM Synchronous Machines in the Stationary Reference Frame

For the purpose of understanding and designing control schemes for PMSM drives, it is necessary to know the dynamic model of PMSM subjected to control. The machine models may vary when using them to design control and observation algorithms of PMSM. Mathematic models valid for instantaneous variation of voltage and current and adequately describing the performance of PMSM in both steady state and transient are commonly obtained by the utilization of space-phasor theory [1]. Figure 3.1 shows the cross-section view of a simplified symmetrical three-phase, two-pole PMSM with wye-connected concentrated identical stator windings. These, however, represent distributed windings which at every instant produce sinusoidal MMF waves centered on the magnetic axes of the respective phases. The phase windings are displaced by 120 electrical degrees from each other. In Figure 3.1, θ_r is the rotor position angle, which is between the magnetic axes of stator winding sA and rotor magnet flux (i.e., d-axis). The positive direction of the magnetic axes of the stator windings coincides with the direction of f_{as}, f_{bs} and f_{cs}. The angular velocity of rotor is calculated by $\omega_r=d\theta_r/dt$, and its positive direction is also shown.

It is assumed that the permeability of iron parts of PMSM under consideration is infinite and flux density is radial in the air-gap. The effects of iron losses, saturation and end-effects are neglected. The analysis given in this chapter is valid for linear magnetic circuits.

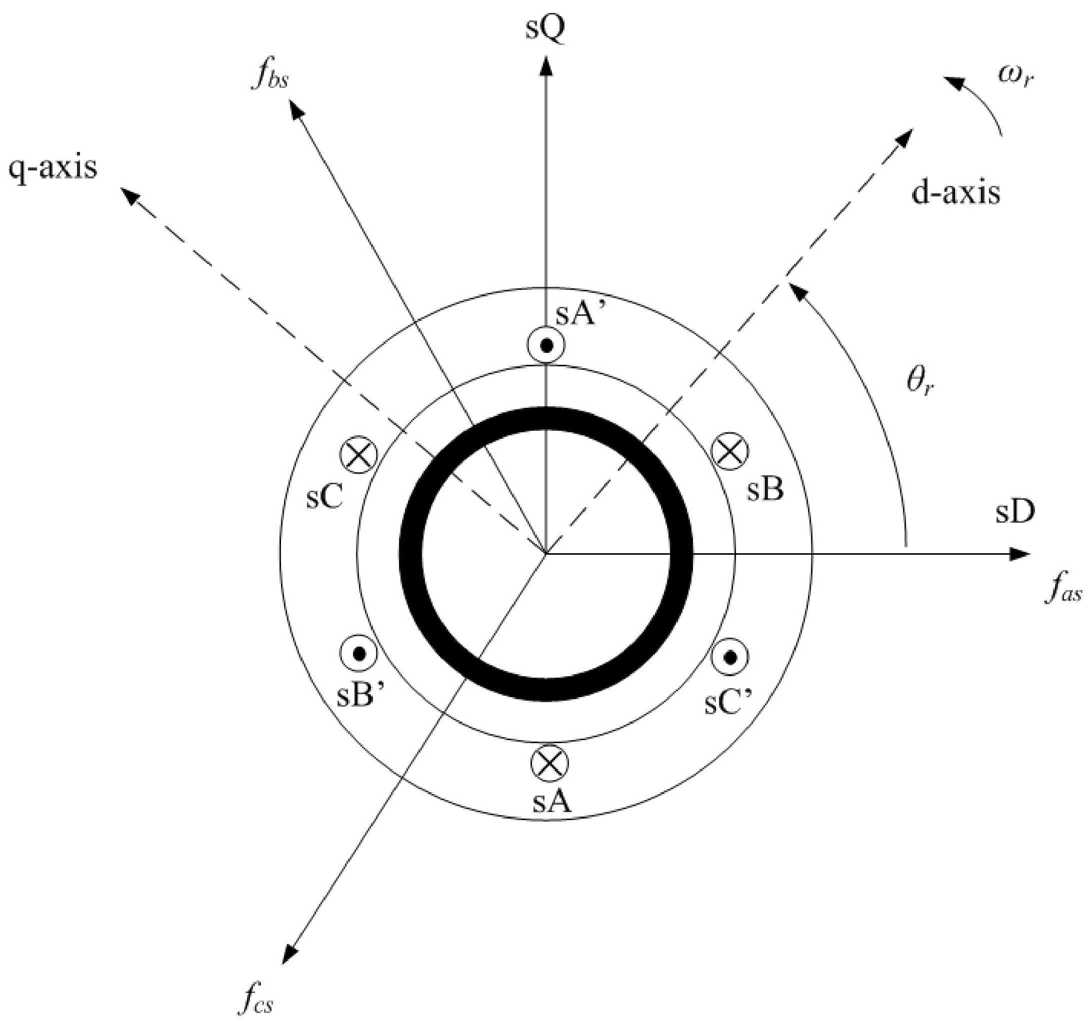

Figure 3.1: Cross-section view of a simplified symmetrical three-phase, two-pole PMSM.

3.1.1 General model of PMSM with saliency

By polarity convention for phase currents and voltages of a PMSM [1,67], its voltage equations can be expressed in terms of instantaneous currents and flux linkages by

$$\vec{v}_{abcs} = r_{abcs} \cdot \vec{i}_{abcs} + p \cdot \vec{\lambda}_{abcs} \tag{3.1}$$

where

$$\begin{aligned} \vec{v}_{abcs} &= [v_{as} \quad v_{bs} \quad v_{cs}]^T \\ \vec{i}_{abcs} &= [i_{as} \quad i_{bs} \quad i_{cs}]^T \\ \vec{\lambda}_{abcs} &= [\lambda_{as} \quad \lambda_{bs} \quad \lambda_{cs}]^T \end{aligned} \tag{3.2}$$

$$r_{abcs} = diag[R_s \quad R_s \quad R_s]$$

In the above, the s subscript denotes variables and parameters associated with the stator circuits, and r subscript denotes those with the rotor circuits. The operator p represents the differentiating operation d/dt. For a magnetically linear system, the flux linkages can be calculated as follows:

$$\vec{\lambda}_{abcs} = L_{abcs} \cdot \vec{i}_{abcs} + \vec{\lambda}_{abcm} \tag{3.3}$$

where

$$L_{abcs} = \begin{bmatrix} L_{aa} & L_{ab} & L_{ac} \\ L_{ba} & L_{bb} & L_{bc} \\ L_{ca} & L_{cb} & L_{cc} \end{bmatrix} \tag{3.4}$$

$$\vec{\lambda}_{abcm} = \lambda_m \begin{bmatrix} \cos\theta_r \\ \cos(\theta_r - 2\pi/3) \\ \cos(\theta_r + 2\pi/3) \end{bmatrix} \tag{3.5}$$

And the winding inductances are respectively

$$L_{aa} = L_{ls} + L_{0s} + L_{2s}\cos 2\theta_r \tag{3.6}$$

$$L_{bb} = L_{ls} + L_{0s} + L_{2s}\cos 2(\theta_r - \frac{2\pi}{3}) \tag{3.7}$$

$$L_{cc} = L_{ls} + L_{0s} + L_{2s}\cos 2(\theta_r + \frac{2\pi}{3}) \tag{3.8}$$

$$L_{ab} = L_{ba} = -\frac{1}{2}L_{0s} + L_{2s}\cos 2(\theta_r - \frac{\pi}{3}) \tag{3.9}$$

$$L_{ac} = L_{ca} = -\frac{1}{2}L_{0s} + L_{2s}\cos 2(\theta_r + \frac{\pi}{3}) \tag{3.10}$$

$$L_{bc} = L_{cb} = -\frac{1}{2}L_{0s} + L_{2s}\cos 2(\theta_r + \pi) \tag{3.11}$$

In the above, L_{ls} is the leakage inductance and L_{0s} and L_{2s} the magnetizing inductance components of the stator windings; λ_m is the flux linkage established by the rotor magnets. It should be noted that the magnetizing inductance components are functions of the rotor position; and the coefficient L_{2s} is negative while L_{0s} positive in the case of interior PM motors due to their unique rotor structure. Therefore, the quadrature-axis magnetizing inductance L_{mq} is larger than the direct-axis magnetizing inductance L_{md} of interior PM motor, which is opposite to general salient-pole synchronous machines.

The flux linkage equation can be extended to the form of

$$\begin{bmatrix} \lambda_{as} \\ \lambda_{bs} \\ \lambda_{cs} \end{bmatrix} = \begin{bmatrix} L_{aa} & L_{ab} & L_{ac} \\ L_{ba} & L_{bb} & L_{bc} \\ L_{ca} & L_{cb} & L_{cc} \end{bmatrix} \begin{bmatrix} i_{as} \\ i_{bs} \\ i_{cs} \end{bmatrix} + \lambda_m \begin{bmatrix} \cos\theta_r \\ \cos(\theta_r - 2\pi/3) \\ \cos(\theta_r + 2\pi/3) \end{bmatrix} \tag{3.12}$$

By two-axis theory, an equivalent quadrature-phase machine is used to represent the three-phase machine, in which the direct- and quadrature-axis currents, fictitious components, are flowing in virtual windings and are related to the actual three-phase stator currents as follows:

$$\vec{i}_{\alpha\beta 0s} = T_{abc\to\alpha\beta 0} \cdot \vec{i}_{abcs} \tag{3.13}$$

where

$$T_{abc\to\alpha\beta 0} = \frac{2}{3}\begin{bmatrix} 1 & -1/2 & -1/2 \\ 0 & \sqrt{3}/2 & -\sqrt{3}/2 \\ 1/2 & 1/2 & 1/2 \end{bmatrix} \tag{3.14}$$

The above transformation of variables is also known as Clark Transformation. Then the new stationary reference frame referring to the quadrature-phase machine is called (*α*-*β*) frame. Whereas, the previous stationary frame is called (*a*-*b*-*c*) frame.

Similarly, voltage and flux linkage variables can be transformed from (*a*-*b*-*c*) frame to (*α*-*β*) frame and consequently the voltage equations expressed in the (*α*-*β*) frame as

$$\vec{v}_{\alpha\beta 0s} = r_{\alpha\beta 0s} \cdot \vec{i}_{\alpha\beta 0s} + p \cdot \vec{\lambda}_{\alpha\beta 0s} \tag{3.15}$$

where

$$\begin{aligned} \vec{v}_{\alpha\beta 0s} &= [v_{\alpha s} \quad v_{\beta s} \quad v_{0s}]^T \\ \vec{i}_{\alpha\beta 0s} &= [i_{\alpha s} \quad i_{\beta s} \quad i_{0s}]^T \\ \vec{\lambda}_{\alpha\beta 0s} &= [\lambda_{\alpha s} \quad \lambda_{\beta s} \quad \lambda_{0s}]^T \end{aligned} \tag{3.16}$$

The flux linkages in (3.3) change to

$$\vec{\lambda}_{\alpha\beta 0s} = L_{\alpha\beta 0s} \cdot \vec{i}_{\alpha\beta 0s} + \vec{\lambda}_{\alpha\beta 0m} \tag{3.17}$$

where

$$L_{\alpha\beta 0s} = \begin{bmatrix} L_{ls} + \frac{3}{2}(L_{0s} + L_{2s}\cos 2\theta_r) & \frac{3}{2}L_{2s}\sin 2\theta_r & 0 \\ \frac{3}{2}L_{2s}\sin 2\theta_r & L_{ls} + \frac{3}{2}(L_{0s} - L_{2s}\cos 2\theta_r) & 0 \\ 0 & 0 & L_{ls} \end{bmatrix} \tag{3.18}$$

$$\vec{\lambda}_{\alpha\beta 0m} = \lambda_m \begin{bmatrix} \cos\theta_r \\ \sin\theta_r \\ 0 \end{bmatrix} \tag{3.19}$$

Provided that the stator windings are in wye-connected arrangement with floating neutral point and supplied with three-phase currents, which vary arbitrarily in time, the sum of the three phase currents are always equal to zero regardless of three-phase balanced condition. As a result, the 0-axis component of current variable in the (α-β) frame, i.e., i_{0s}, is zero and so are the 0-axis components of voltage and flux linkage variables. Therefore, the equations (3.15 – 3.19) can be reduced to

$$\vec{v}_{\alpha\beta s} = r_{\alpha\beta s} \cdot \vec{i}_{\alpha\beta s} + p \cdot \vec{\lambda}_{\alpha\beta s} \tag{3.20}$$

$$\begin{aligned} \vec{v}_{\alpha\beta s} &= [v_{\alpha s} \quad v_{\beta s}]^T \\ \vec{i}_{\alpha\beta s} &= [i_{\alpha s} \quad i_{\beta s}]^T \\ \vec{\lambda}_{\alpha\beta s} &= [\lambda_{\alpha s} \quad \lambda_{\beta s}]^T \end{aligned} \tag{3.21}$$

$$\vec{\lambda}_{\alpha\beta s} = L_{\alpha\beta s} \cdot \vec{i}_{\alpha\beta s} + \vec{\lambda}_{\alpha\beta m} \tag{3.22}$$

where

$$L_{\alpha\beta s} = \begin{bmatrix} L_{ls} + \frac{3}{2}(L_{0s} + L_{2s}\cos 2\theta_r) & \frac{3}{2}L_{2s}\sin 2\theta_r \\ \frac{3}{2}L_{2s}\sin 2\theta_r & L_{ls} + \frac{3}{2}(L_{0s} - L_{2s}\cos 2\theta_r) \end{bmatrix} \tag{3.23}$$

$$\vec{\lambda}_{\alpha\beta m} = \lambda_m \begin{bmatrix} \cos\theta_r \\ \sin\theta_r \end{bmatrix} \tag{3.24}$$

3.1.2 General model of PMSM without saliency

For a magnetically symmetrical PMSM, e.g., surface-mounted PM motor, the effective air gap is considered to be uniform, which makes the effects of saliency negligible. Thus the direct-axis magnetizing inductance L_{md} is equal to the quadrature-axis magnetizing inductance L_{mq}, i.e., $L_{md} = L_{mq} = L_{ms}$ (namely stator magnetizing inductance). And the inductance matrix expressed in (3.4) and (3.23) changes respectively to

$$L_{abcs} = \begin{bmatrix} L_{ls} + L_{ms} & -\frac{1}{2}L_{ms} & -\frac{1}{2}L_{ms} \\ -\frac{1}{2}L_{ms} & L_{ls} + L_{ms} & L_{bc} \\ -\frac{1}{2}L_{ms} & -\frac{1}{2}L_{ms} & L_{ls} + L_{ms} \end{bmatrix} \tag{3.25}$$

$$L_{\alpha\beta 0s} = \begin{bmatrix} L_s & 0 & 0 \\ 0 & L_s & 0 \\ 0 & 0 & L_0 \end{bmatrix} \tag{3.26}$$

where

$$L_s = L_{ls} + \frac{3}{2}L_{ms}$$

It is interesting to note that the transformed inductance matrix by Clark Transformation and Park Transformation (discussed in the next section) may reduce to a diagonal matrix, which, in effect, magnetically decouples the substitute or transformed variables in every reference frame other than the (a-b-c) frame.

For a wye-connected PMSM without saliency, the reduced voltage equation in the (α-β) frame is often of the form

$$\vec{v}_{\alpha\beta s} = r_{\alpha\beta s} \cdot \vec{i}_{\alpha\beta s} + L_{\alpha\beta s} \cdot \dot{\vec{i}}_{\alpha\beta s} + \vec{e}_{\alpha\beta s} \tag{3.27}$$

where

$$r_{\alpha\beta s} = \begin{bmatrix} R_s & 0 \\ 0 & R_s \end{bmatrix} \tag{3.28}$$

$$L_{\alpha\beta s} = \begin{bmatrix} L_s & 0 \\ 0 & L_s \end{bmatrix} \tag{3.29}$$

$$\vec{e}_{\alpha\beta s} = \begin{bmatrix} e_{\alpha s} \\ e_{\beta s} \end{bmatrix} = \omega_r \lambda_m \cdot \begin{bmatrix} -\sin(\theta_r) \\ \cos(\theta_r) \end{bmatrix} \tag{3.30}$$

In the above, the last item on the right, i.e., $\vec{e}_{\alpha\beta s}$, represents the induced back EMF in the windings of the fictitious quadrature-phase machine.

By selecting the stator currents as independent variables, we rewrite the voltage equation given in (3.27) and get the state or differential equation of PMSM in the (α-β) frame as

$$\dot{\vec{i}}_{\alpha\beta s} = -L_{\alpha\beta s}{}^{-1} r_{\alpha\beta s} \cdot \vec{i}_{\alpha\beta s} + L_{\alpha\beta s}{}^{-1} (\vec{v}_{\alpha\beta s} - \vec{e}_{\alpha\beta s}) \tag{3.31}$$

More commonly, a matrix form is used like

$$\begin{bmatrix} \dot{i}_{\alpha s} \\ \dot{i}_{\beta s} \end{bmatrix} = \begin{bmatrix} -R_S/L_S & 0 \\ 0 & -R_S/L_S \end{bmatrix} \begin{bmatrix} i_{\alpha s} \\ i_{\beta s} \end{bmatrix} + \begin{bmatrix} 1/L_S & 0 \\ 0 & 1/L_S \end{bmatrix} \left(\begin{bmatrix} v_{\alpha s} \\ v_{\beta s} \end{bmatrix} - \begin{bmatrix} e_{\alpha s} \\ e_{\beta s} \end{bmatrix} \right) \tag{3.32}$$

The above equations will be referred to as dynamic model of PMSM when designing sliding mode observer for sensorless control algorithms in later chapters.

3.2 Mathematical Model of PM Synchronous Machines in the Rotating Reference Frame

In the late 1920s, R. H. Park introduced a new approach to implement change of variables, which replaces the variables (voltages, currents, and flux linkages) associated with stator windings of a synchronous machine with variables associated with fictitious windings rotating with the rotor. Park's transformation eliminates all time-varying inductances from the voltage equations of the synchronous machine which occur due to electric circuits both in relative motion and with varying magnetic reluctance [67]. The transformation, namely Park Transformation, and its inversion can be mathematically expressed in the following:

$$f_{dq0s} = T_{abc\to dq0} \cdot f_{abcs} \tag{3.33}$$

where

$$T_{abc\to dq0} = T_{\alpha\beta 0\to dq0} T_{abc\to\alpha\beta 0} = \frac{2}{3}\begin{bmatrix} \cos\theta & \cos(\theta - 2\pi/3) & \cos(\theta - 4\pi/3) \\ -\sin\theta & -\sin(\theta - 2\pi/3) & -\sin(\theta - 4\pi/3) \\ 1/2 & 1/2 & 1/2 \end{bmatrix} \tag{3.34}$$

$$T_{\alpha\beta 0\to dq0} = \begin{bmatrix} \cos\theta & \sin\theta & 0 \\ -\sin\theta & \cos\theta & 0 \\ 0 & 0 & 1 \end{bmatrix} \tag{3.35}$$

And

$$f_{abcs} = T_{dq0\to abc} \cdot f_{dq0s} \tag{3.36}$$

where

$$T_{dq0\to abc} = (T_{abc\to dq0})^{-1} = \begin{bmatrix} \cos\theta & -\sin\theta & 1 \\ \cos(\theta - 2\pi/3) & -\sin(\theta - 2\pi/3) & 1 \\ \cos(\theta - 4\pi/3) & -\sin(\theta - 4\pi/3) & 1 \end{bmatrix} \tag{3.37}$$

In the above equations, ***f*** can represent either voltage, current or flux linkage vector variables. The angular displacement θ should be continuous; however, the angular velocity is unspecified and can be selected arbitrarily to expedite the solution of system equations or to satisfy system constraints. The frame of reference may rotate at any constant or varying angular velocity or it may remain stationary as in the Clark Transformation.

For a three-phase balanced system, the transformation matrix in (3.33) can be reduced to

$$T_{abc\to dq} == \frac{2}{3}\begin{bmatrix} \cos\theta & \cos(\theta - 2\pi/3) & \cos(\theta - 4\pi/3) \\ -\sin\theta & -\sin(\theta - 2\pi/3) & -\sin(\theta - 4\pi/3) \end{bmatrix} \tag{3.38}$$

3.2.1 General model of PMSM with saliency

In terms of the variables in the rotating reference frame aligned with rotor flux, i.e., rotor reference frame, the voltage equation (3.15) becomes

$$\vec{v}_{dq0s} = r_s \cdot \vec{i}_{dq0s} + T_{abc\to dq0} \cdot p[(T_{abc\to dq0})^{-1}]\vec{\lambda}_{dq0s} + p\vec{\lambda}_{dq0s} \tag{3.39}$$

where

$$\begin{aligned} \vec{v}_{dq0s} &= [v_{ds} \quad v_{qs} \quad v_{0s}]^T \\ \vec{i}_{dq0s} &= [i_{ds} \quad i_{qs} \quad i_{0s}]^T \\ \vec{\lambda}_{dq0s} &= [\lambda_{ds} \quad \lambda_{qs} \quad \lambda_{0s}]^T \end{aligned} \tag{3.40}$$

The stator flux linkage viewed in the rotor reference frame is given by

$$\vec{\lambda}_{dq0s} = L_{dq0s} \cdot \vec{i}_{dq0s} + \vec{\lambda}_{dq0m} \tag{3.41}$$

where

$$\vec{\lambda}_{dq0m} = [\lambda_m \quad 0 \quad 0]^T \tag{3.42}$$

$$L_{dq0s} = \begin{bmatrix} L_d & 0 & 0 \\ 0 & L_q & 0 \\ 0 & 0 & L_0 \end{bmatrix} \tag{3.43}$$

$$L_d = L_{ls} + L_{md} = L_{ls} + \frac{3}{2}(L_{0s} + L_{2s}) \tag{3.44}$$

$$L_q = L_{ls} + L_{mq} = L_{ls} + \frac{3}{2}(L_{0s} - L_{2s}) \tag{3.45}$$

$$L_0 = L_{ls} \tag{3.46}$$

The relationship between L_d, L_q and L_{0s}, L_{2s} is

$$L_{md} = \frac{3}{2}(L_{0s} + L_{2s}) \tag{3.47}$$

$$L_{mq} = \frac{3}{2}(L_{0s} - L_{2s}) \tag{3.48}$$

$$L_{0s} = \frac{2}{3}\left(\frac{L_{md} + L_{mq}}{2}\right) = \frac{1}{3}(L_{md} + L_{mq}) \tag{3.49}$$

$$L_{2s} = \frac{2}{3}\left(\frac{L_{md} - L_{mq}}{2}\right) = \frac{1}{3}(L_{md} - L_{mq}) \tag{3.50}$$

Here, L_d is named as direct-axis stator inductance and L_q the quadrature-axis stator inductance.

It is easy to show that

$$p[(T_{abc\to dq0})^{-1}] = \omega_r \begin{bmatrix} -\sin\theta & -\cos\theta & 0 \\ -\sin(\theta - 2\pi/3) & -\cos(\theta - 2\pi/3) & 0 \\ -\sin(\theta - 4\pi/3) & -\cos(\theta - 4\pi/3) & 0 \end{bmatrix} \tag{3.51}$$

Thus

$$T_{abc\to dq0}\, p[(T_{abc\to dq0})^{-1}] = \omega_r \begin{bmatrix} 0 & -1 & 0 \\ 1 & 0 & 0 \\ 0 & 0 & 0 \end{bmatrix} \tag{3.52}$$

Equation (3.39) is often written in expanded form as

$$v_{ds} = R_s i_{ds} + L_d \frac{di_{ds}}{dt} - \omega_r L_q i_{qs} \tag{3.53}$$

$$v_{qs} = R_s i_{qs} + L_q \frac{di_{qs}}{dt} + \omega_r (L_d i_{ds} + \lambda_m) \tag{3.54}$$

$$v_{0s} = R_s i_{0s} + L_0 \frac{di_{0s}}{dt} \tag{3.55}$$

Under balanced steady-state conditions, the electrical angular velocity of rotor ω_r is considered constant and equal to that of the synchronously rotating reference frame. In this mode of operation, with the time rate of change of all flux linkages neglected, the steady state versions of (3.53), (3.54) and (3.55) become

$$V_{ds} = R_s I_{ds} - \omega_r L_q I_{qs} \tag{3.56}$$

$$V_{qs} = R_s I_{qs} + \omega_r (L_d I_{ds} + \lambda_m) \tag{3.57}$$

$$V_{0s} = R_s I_{0s} = 0 \tag{3.58}$$

Here the uppercase letters are used to denote steady state quantities.

Electromagnetic torque can be expressed with the stator variables in the rotor reference frame as

$$T_e = \left(\frac{3}{2}\right)\left(\frac{P}{2}\right)\left(\lambda_{ds} i_{qs} - \lambda_{qs} i_{ds}\right) \tag{3.59}$$

where P is the number of poles.

Appropriate substitution of (3.41) into the above torque equation yields

$$T_e = \left(\frac{3}{2}\right)\left(\frac{P}{2}\right)\left[\lambda_m i_{qs} - (L_q - L_d) i_{qs} i_{ds}\right] \tag{3.60}$$

3.2.2 General model of PMSM without saliency

Similarly as in 3.1.2, for a PMSM without saliency, the inductance matrix used in the rotor reference frame is in the form of

$$L_{dq0s} = \begin{bmatrix} L_s & 0 & 0 \\ 0 & L_s & 0 \\ 0 & 0 & L_0 \end{bmatrix} \tag{3.61}$$

It is noted that L_s and L_0 in the matrix L_{dq0s} are the same as in (3.26).

Therefore, the voltage and torque equations can be obtained respectively by

$$v_{ds} = R_s i_{ds} + L_s \frac{di_{ds}}{dt} - \omega_r L_s i_{qs} \tag{3.62}$$

$$v_{qs} = R_s i_{qs} + L_s \frac{di_{qs}}{dt} + \omega_r (L_s i_{ds} + \lambda_m) \tag{3.63}$$

$$V_{ds} = R_s I_{ds} - \omega_r L_s I_{qs} \tag{3.64}$$

$$V_{qs} = R_s I_{qs} + \omega_r (L_s I_{ds} + \lambda_m) \tag{3.65}$$

$$T_e = \left(\frac{3}{2}\right)\left(\frac{P}{2}\right)\lambda_m i_{qs} \tag{3.66}$$

By examining (3.60) and (3.66), it is worth noting that both direct-axis and quadrature-axis current component of a PMSM with saliency are involved in the production of electromagnetic torque while only the quadrature-axis current component contributes in a PMSM without saliency. This implies that different current control strategies are required by the two types of PM machines for torque production.

3.3 Operation of PM Synchronous Machines

In general, an inverter-fed PM synchronous machine, in an electrical ac drive system, can operate as either a motor or generator in both rotating directions, i.e., four-quadrant operation. On the other hand, constant torque can be delivered by a PM synchronous motor as long as the inverter output voltage doesn't reach its limit. Once the PM motor reaches its rated speed or base speed, the induced back-EMF in the stator windings approaches the maximum available terminal voltage. The torque would drop rapidly with speed increasing. To extend its operating speed range of PMSM, demagnetizing phase currents are generally applied to weaken the air-gap flux. This is known as flux-weakening control and thus the motor is operated in the flux-weakening region. As the speed continuously increases, the maximum output power may decrease due to the limited terminal voltages applied by the power inverter. With proper current control, instead, constant output power of PMSM can be achieved, referring to constant-power operation. Figure 3.2 shows a typical torque/power vs. speed characteristics curve of PMSM drive system. It can be seen that the large torque for starting and low-speed operation is required while the constant power over wide high-speed range preferred because it can significantly reduce the cost and size of the PMSM drive system. Accordingly, the speed range with respect to above operations is named constant-torque region and constant-power region in this dissertation.

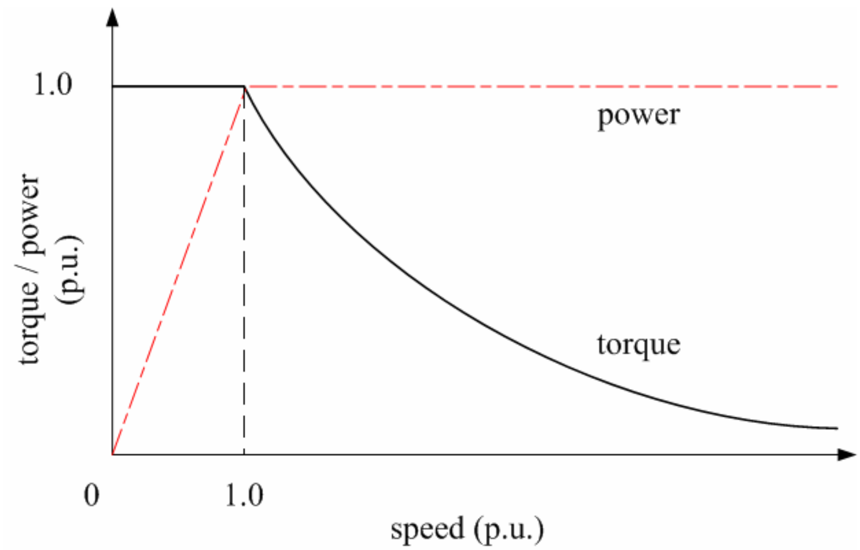

Figure 3.2: Typical characteristics curve of torque/power vs. speed of PMSM.

3.3.1 Constant-torque operation

In a PM machine, torque control can be achieved, similarly to that of a dc machine [1]. As presented previously in (3.60) and (3.66), the electromagnetic torque consists of: 1) magnet torque, which is proportional to the product of the magnet flux linkage (i.e., rotor flux in the rotor reference frame) and the quadrature-axis stator current (i.e., torque-producing stator current component); 2) reluctance torque only for PM machines with saliency, which is dependent on the saliency ratio and the product of the direct-axis and the quadrature-axis stator current component. Hence the electromagnetic torque of PMSM can be controlled instantaneously through controlling the stator currents in the rotating reference frame, to meet load torque requirements.

If the stator currents are set to their maximum permissible value then, from (3.66), it is easy to see the maximum torque of SPM motors

$$T_{e,\max} = \left(\frac{3}{2}\right)\left(\frac{P}{2}\right)\lambda_m I_{s\max} \tag{3.67}$$

where the quadrature-axis current component $I_{qs,maxT}$ equals the maximum current I_{smax} while the direct-axis component $I_{ds,maxT}$ is kept zero as

$$\begin{cases} I_{ds,\max T} = 0 \\ I_{qs,\max T} = I_{s\max} \end{cases} \tag{3.68}$$

As to IPM motors, in contrast, the maximum torque is produced when the stator current reaches its maximum but both its direct-axis and quadrature-axis component, $I_{ds,maxT}$ and $I_{qs,maxT}$ respectively, have values in agreement with torque optimization, which can be expressed by

$$\begin{cases} I_{ds,\max T} = \dfrac{\lambda_m}{4(L_q - L_d)} - \sqrt{\dfrac{\lambda_m{}^2}{16(L_q - L_d)^2} + \dfrac{I_{s\max}{}^2}{2}} \\ I_{qs,\max T} = \sqrt{I_{s\max}{}^2 - I_{ds,\max T}{}^2} \end{cases} \tag{3.69}$$

Therefore, with current control in the rotor reference frame, the PM motors can produce the maximum torque constantly at variable speeds until the maximum stator current cannot be applied.

3.3.2 Constraints of stator currents and voltages

In general, a PM machine is fed by a Voltage Source Inverter (VSI) [1]. The dc bus of VSI is maintained as voltage stiff by the use of large capacitors in the dc link. Therefore, the bus voltage of VSI is fixed or varies only within a small range. With the speed of the PM motors going up, the voltage applied to the motor must increase accordingly to counteract the speed-proportional induced back EMF in the stator windings as defined in (3.27). When the speed reaches the rated value, eventually, the voltage applied to the PMSM cannot be further increased to maintain the current required by torque production. On the other hand, considering the current capability, the maximum stator current is limited by the current rating of inverter as well as the thermal rating of stator windings. Therefore, the maximum output torque and power developed by PMSM is ultimately determined by the maximum current and voltage which inverter can apply to the machine.

Assume that the voltage applied to the PM motor reaches its limit. The maximum stator voltage, V_{smax}, is determined by the available dc bus voltage and PWM strategy. Considering (3.53) and (3.54), it must satisfy,

$$v_{ds}^{2} + v_{qs}^{2} \le V_{s\max}^{2} \tag{3.70}$$

Hence, at high speeds, the voltage vector should remain on the locus of a circle with radius V_{smax} for maximum-power output.

Neglecting the ohmic voltage drop of stator resistance for high-speed operation, the limit by the maximum stator voltage is expressed in terms of steady-state currents as

$$(-\omega_r L_q I_{qs})^2 + (\omega_r L_d I_{ds} + \omega_r \lambda_m)^2 \le V_{s\max}^{2} \tag{3.71}$$

The above inequation can be rearranged to form

$$\left(\frac{I_{qs}}{L_d / L_q}\right)^2 + \left(I_{ds} + \frac{\lambda_m}{L_d}\right)^2 \leq \left(\frac{V_{s\max}}{\omega_r L_d}\right)^2 \tag{3.72}$$

And further

$$\left(\frac{I_{qs}}{a}\right)^2 + \left(\frac{I_{ds} + \lambda_m / L_d}{b}\right)^2 \leq 1 \tag{3.73}$$

It can be seen that the current vector trajectories in the rotor reference frame are constrained by an ellipse at a specific speed, corresponding to the critical condition of (3.72) or (3.73). Referring to IPM motors, of which the quadrature-axis stator inductance is larger than the direct-axis inductance, i.e., $L_q > L_d$, the minor axis length of the ellipse, a, is $V_{smax}/(\omega_r L_q)$ and the length of major axis, b, is $V_{smax}/(\omega_r L_d)$. The eccentricity of the ellipse is defined by

$$e = \frac{\sqrt{b^2 - a^2}}{b} = \frac{\sqrt{\left(V_{s\max} / \omega_r L_d\right)^2 - \left(V_{s\max} / \omega_r L_q\right)^2}}{V_{s\max} / \omega_r L_d} = \sqrt{1 - \left(\frac{L_d}{L_q}\right)^2} \tag{3.74}$$

Figure 3.3 shows the voltage-limited ellipses with respect to different operating speeds in the flux-weakening region. As illustrated, the constraint equation (3.73) determines a series of nested ellipses, i.e., concentration ellipses, centering at Point A ($-\lambda_m / L_d$, 0) in the i_{ds}-i_{qs} plane, i.e., the rotor reference frame. As the maximum voltage V_{smax} is fixed, the ellipse shrinks inversely with rotor speed ω_r. It should be noted that the shape of the ellipses depends upon the saliency ratio, which is defined as L_q/L_d. For all non-saliency PM machines, e.g., surface-mounted PM motors, the voltage-limited ellipses change to circles and the corresponding inequation is

$$\left(I_{qs}\right)^2 + \left(I_{ds} + \frac{\lambda_m}{L_s}\right)^2 \le \left(\frac{V_{s\max}}{\omega_r L_s}\right)^2 \tag{3.75}$$

On the other hand, the current I_{ds} and I_{qs} must satisfy

$$I_{qs}{}^2 + I_{ds}{}^2 \le I_{s\max}{}^2 \tag{3.76}$$

where I_{smax} is the allowable maximum stator current.

This expression represents a current-limited circle centering at the origin, i.e., Point O, but with the radius of I_{smax} as shown in Figure 3.3.

It should be noticed that this current-limited circle remains constant for any speed and the instantaneous current i_{ds} and i_{qs} must apply to the constraint equation (3.76) also.

In the i_{ds}-i_{qs} plane, any combination of values of current component i_{ds} and i_{qs} generates a directed current vector from the origin. To a given rotor speed, the current vector can reach anywhere inside or on the boundary of the overlap area between the associated voltage-limited ellipse/circle and the current-limited circle during steady-state operation -- but not outside it. The overlap area becomes smaller and smaller even disappears when the rotor speed keeps increasing, indicating progressively smaller ranges for the current vector in the flux-weakening region.

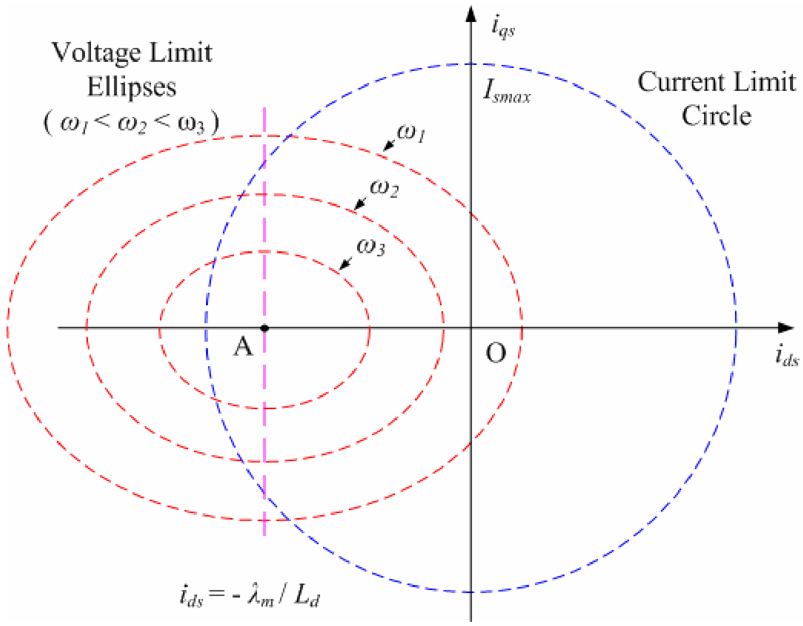

(a)

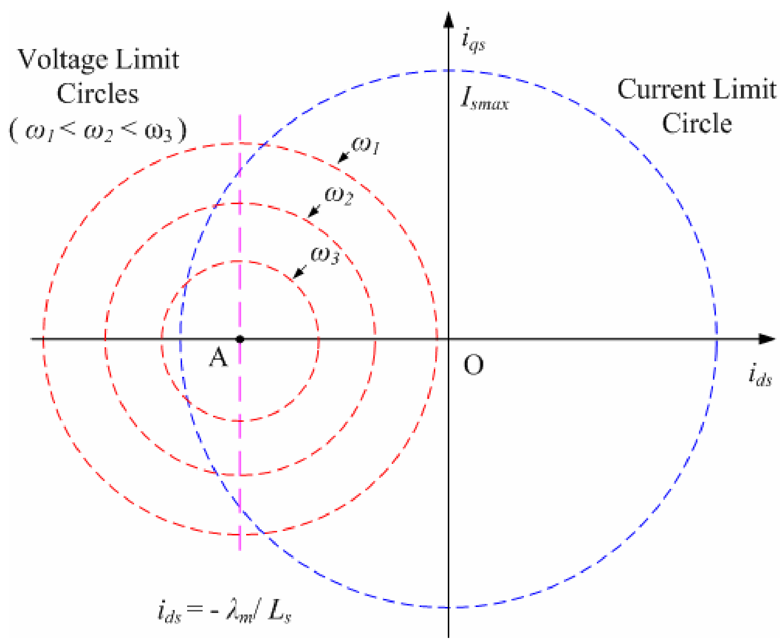

(b)

Figure 3.3: Current and voltage limits of PMSM drive system: (a) IPM, (b) SPM.

3.3.3 Constant-power operation

As a further advantage, constant-power output of PM machines can be achieved over an extended speed range by means of flux weakening. Such extended-speed characteristics make the PM machine, especially the IPM motor, a candidate for applications requiring constant-power operation such as traction and spindle drives.

Two commonly used constant-power control methods are [75]:

1) Constant-Voltage Control; and

2) Constant-Current Control.

The first method is based on assuming the steady-state voltage vector constant in the rotor reference frame. And then the reference i_{ds} and i_{qs} current components can be derived from voltage equations. When the stator currents are accurately controlled tracking the current references, the vertex of the current vector moves along a line with the slope value of i_{qs}/i_{ds} until reaching the current limit circle.

In the second method, on the contrary, the reference i_{ds} and i_{qs} current components are set with fixed values due to keeping the output power constant. Therefore, the current vector stays constant in the rotor reference frame while the vertex of the voltage vector moves along a vertical line until reaching the voltage limit.

Regarding the complexity, the first one is easier to implement due to the linear relationship between i_{ds} and i_{qs}. However, the second one doesn't depend on motor parameters, featuring higher control robustness.

3.4 Vector Control of PM Synchronous Machines

On the previous discussions, the key to controlling the PM motors is the accurate current regulation either for the constant-torque operation or the constant-power operation in the flux-weakening region. As in other high-performance ac drive systems, vector control is conventionally selected for PMSM drive systems to control torque and flux simultaneously. Among various PMSM vector control strategies, the rotor-oriented control scheme is relatively simple but practical. The excitation flux is frozen to the direct axis of the rotor and thus no loss of synchronization could happen. Furthermore, the phase current can truly be controlled in both magnitude and its position angle by means of decoupling the direct-axis and quadrature-axis current component in the rotating reference frame aligned with the rotor flux. Therefore, the direct-axis and quadrature-axis current can be controlled independently, corresponding to the flux and torque respectively. A block diagram of the rotor-oriented vector control of PMSM is shown in Figure 3.4. It is assumed that there is no phase lag of current regulation.

According to equations (3.64) and (3.65), steady-state phasor diagrams shown in Figures 3.5(a), (b) can be plotted, which are for PMSM without saliency, e.g., SPM. The phasor diagram in Figure 3.5(a) corresponds to the case where there is no direct-axis current component (i.e., I_{ds}=0) for the constant-torque operation of PM motors without saliency. In Figure 3.5(b) the phasors are shown for the operation above the base speed in the flux-weakening region where I_{ds} <0. The angle between the back EMF and the stator voltage is the load angle δ, and the displacement angle of the stator current is ϕ.

Similarly, steady-state phasor diagrams for PMSM with saliency, e.g., IPM motor, are also shown in Figures 3.5 (c), (d).

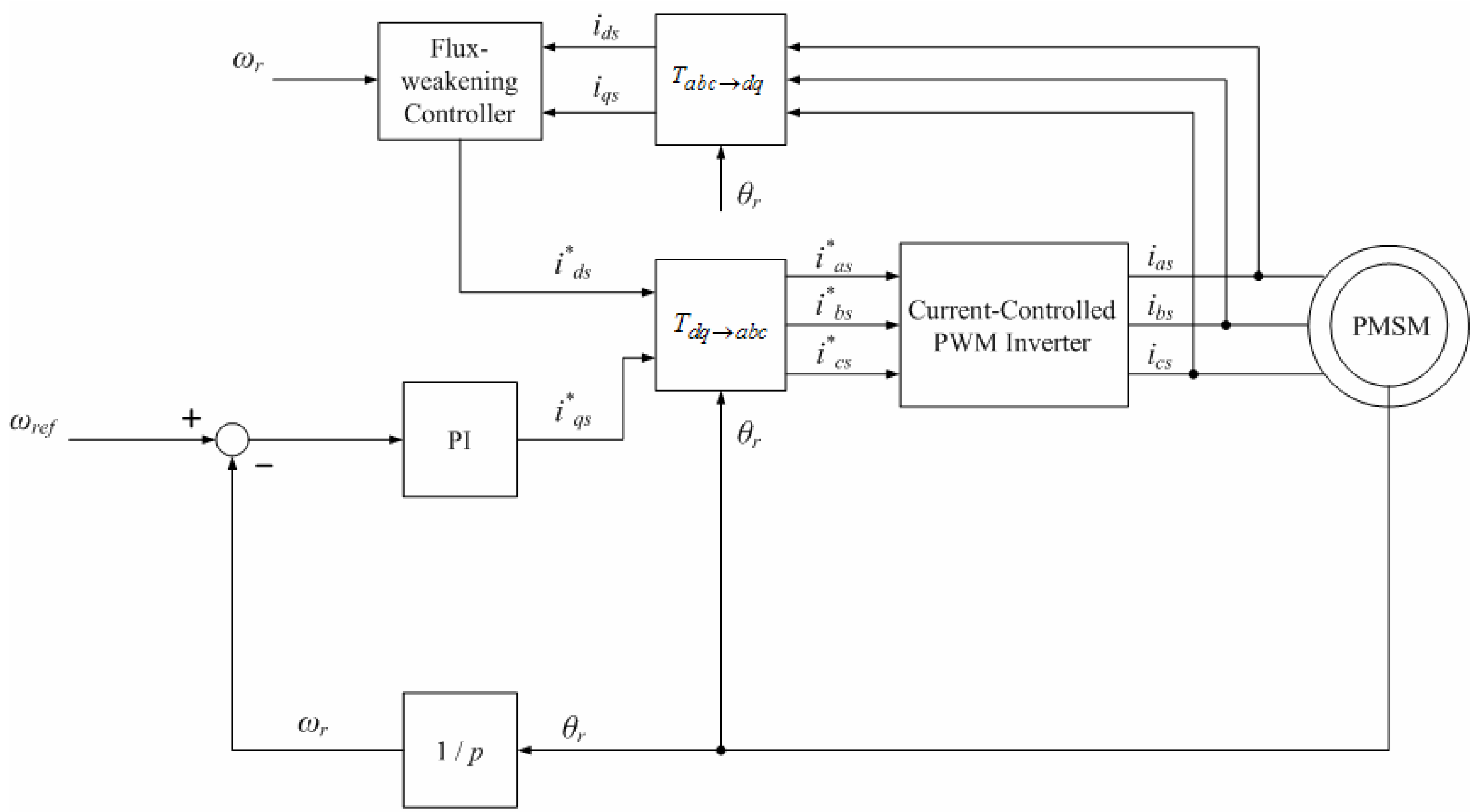

Figure 3.4 Block diagram of rotor-oriented vector control of PMSM

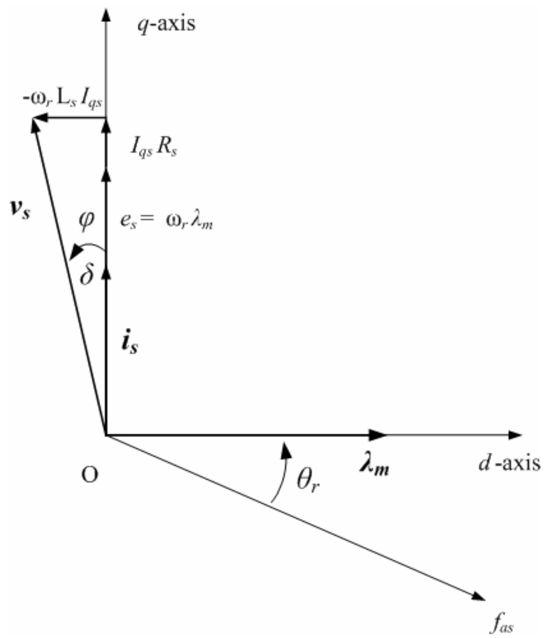

(a) Operation of SPM below base speed.

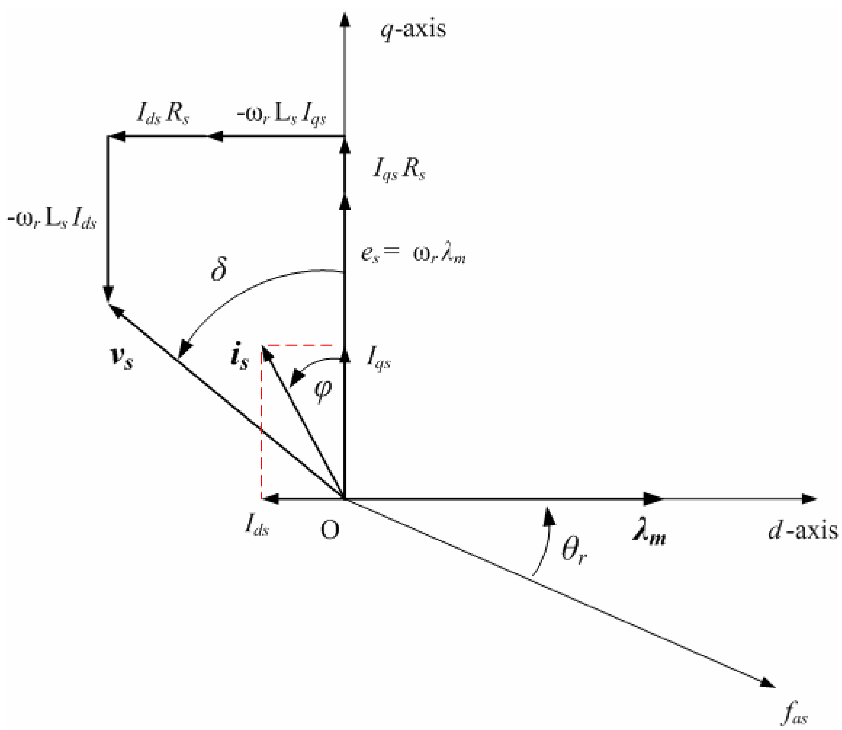

(b) Operation of SPM above base speed.

Figure 3.5: Steady-state phasor diagrams of PMSM.

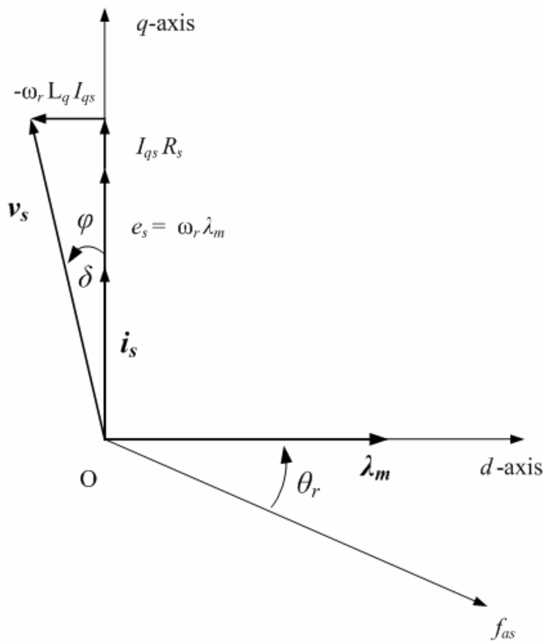

(c) Operation of IPM below base speed.

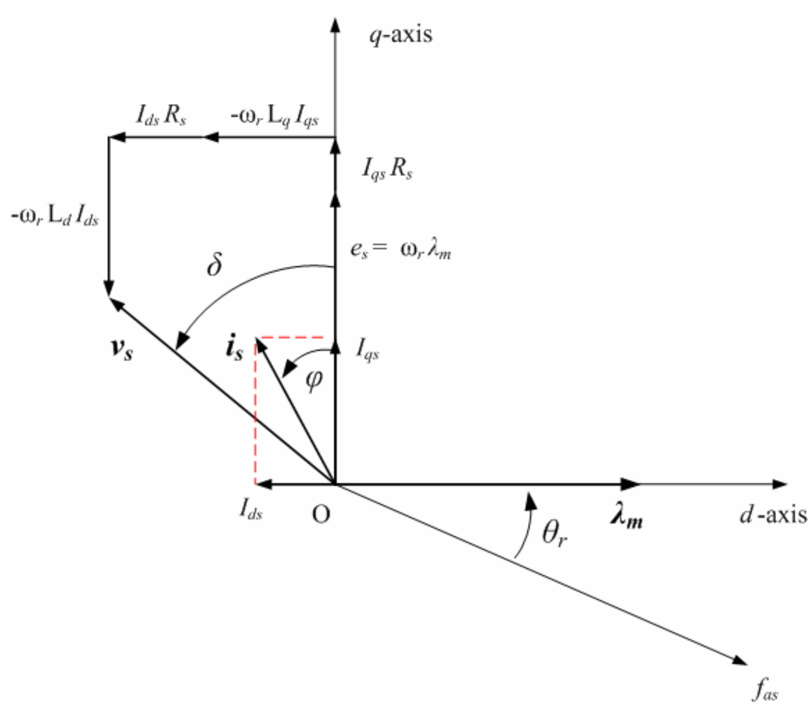

(d) Operation of IPM above base speed

Figure 3.5 (continued): Steady-state phasor diagrams of PMSM.

3.5 Control Modes – MTPA, LVMT

The maximum electromagnetic torque and output power developed by PM machines is ultimately dependent on the allowable inverter current rating and the maximum output voltage which the inverter can apply to the machine. Considering the limited current and voltage capabilities, a specific control scheme may be desirable which yields attractive characteristics of performance including large delivered torque, fast dynamic response, and high efficiency. Two control modes are usually considered for the constant-torque and flux-weakening operation respectively. They are:

1) Maximum Torque per Ampere (MTPA); and
2) Limited-Voltage Maximum Torque (LVMT).

In a PM machine, which operates at a given speed and torque, optimal efficiency can be obtained by the application of an optimal voltage that minimizes power losses. At low speeds, this optimum will coincide with the condition of maximum torque per stator ampere, assuming the core losses negligible. Such operation leads to minimal copper losses of stator windings and power losses of semiconductor switches in power inverter. Furthermore, minimization of the stator current for the given maximum torque results in lower current rating of the inverter and thus the coverall cost of the PMSM drive system is reduced. Therefore, in most cases, the MTPA control mode is preferred for the constant-torque operation of PM machines. The relationship between the reference i_{ds} and i_{qs} current components for the MTPA control can be derived and expressed as

$$i_{ds} = \frac{\lambda_m}{2(L_q - L_d)} - \sqrt{\frac{\lambda_m{}^2}{4(L_q - L_d)^2} + i_{qs}{}^2} \qquad (3.77)$$

or

$$\begin{cases} i_{ds} = 0 \\ i_{qs} = I_s \end{cases} \tag{3.78}$$

where I_s is the magnitude of the stator current. Equation (3.77) applies to the IPM motors while (3.78) to SPM motors. Figure 3.6 shows the current trajectories for MTPA and LVMT control of PM machines with and without saliency in the i_{ds}-i_{qs} plane, assuming

$$\begin{cases} \lambda_m / L_s < I_{s\max} \quad or \\ \lambda_m / L_d < I_{s\max} \end{cases} \tag{3.79}$$

It can be seen that the torque-per-ampere ratio in the SPM motors is maximized by setting the direct-axis reference current component i_{ds} to zero for all values of torque. So the sinusoidal stator currents are always in-phase with the induced back-EMF. In contrast, the MTPA current trajectory for IPM initially moves along the quadrature-axis for low values of torque before swinging symmetrically into the second or third quadrant along 45° asymptotes reflecting the nature of saliency.

At high speeds in the flux weakening region, maximum output power is achievable by means of the LVMT control. For a given speed, the maximum torque under both current and voltage constraints leads to the maximum output power. The current vector trajectory of maximum torque control in the i_{ds} - i_{qs} plane is selected as follows:

Region I ($\omega_r < \omega_{c1}$ or $\omega_r = \omega_{c1}$): the current component i_{ds} and i_{qs} are with constant values as given in (3.68) or (3.69). The stator current vector is fixed at Point B in Figure 3.6. The maximum rotor speed for the constant-torque operation with maximum torque corresponds with ω_{c1}, at which the terminal voltage reaches the limited value of V_{smax}.

$$\omega_{c1} = \frac{V_{s\max}}{\sqrt{(\lambda_m + L_d I_{ds,\max T})^2 + (L_q I_{qs,\max T})^2}} \tag{3.80}$$

Region II ($\omega_{c1} < \omega_r < \omega_{c2}$ or $\omega_r = \omega_{c2}$): the selection of i_{ds} and i_{qs} relates to the intersection of the current-limit circle and the voltage-limited ellipse or circle. Thus the current vector will move from Point B to C along the current-limited circle as the rotor speed ω_r increases up to ω_{c2}, which is the minimum speed for the LVMT control. At the speed ω_{c2}, the voltage-limited ellipse or circle includes Point C which is the intersection of the LVMT trajectory and the current-limited circle. Below this speed, the LVMT operating point cannot be reached, because the LVMT trajectory intersects the voltage-limited ellipses or circles outside the current-limited circle.

Within this region, the relationship between i_{ds} and i_{qs} is derived from (3.72):

$$I_{ds} = -\frac{\lambda_m}{L_d} + \frac{1}{L_d}\sqrt{\left(\frac{V_{s\max}}{\omega_r}\right)^2 - \left(L_q I_{qs}\right)^2} \tag{3.81}$$

where $\left|I_{qs}\right| \le V_{s\max} / (\omega_r L_q)$.

To SPM motors, the relationship is

$$I_{ds} = -\frac{\lambda_m}{L_s} + \frac{1}{L_s}\sqrt{\left(\frac{V_{s\max}}{\omega_r}\right)^2 - \left(L_s I_{qs}\right)^2} \tag{3.82}$$

where $\left|I_{qs}\right| \le V_{s\max} / (\omega_r L_s)$.

Region III ($\omega_r > \omega_{c2}$): the current vector moves from Point C to A along the LVMT trajectory. Note that the LVMT trajectory of IPM agrees with a hyperbola whose vertex is Point A ($-\lambda_m / L_d$, 0) while the LVMT trajectory of SPM changes to a vertical line through Point A ($-\lambda_m / L_s$, 0).

Region I corresponds to the operating condition of $I_s = I_{smax}$ and $V_s < V_{smax}$, where V_s is the magnitude of phase voltage. Region II corresponds to $I_s = I_{smax}$ and $V_s = V_{smax}$. And Region III corresponds to $I_s < I_{smax}$ and $V_s = V_{smax}$. If the value of λ_m / L_d is larger than I_{smax} , Point A will be outside of the current-limited circle. So is the LVMT trajectory. Therefore, Region III does not apply for real operation, and the output power will become zero at the speed $\omega_r = \omega_{c3}$:

$$\omega_{c3} = \frac{V_{s\max}}{\lambda_m - L_d I_{s\max}} \tag{3.83}$$

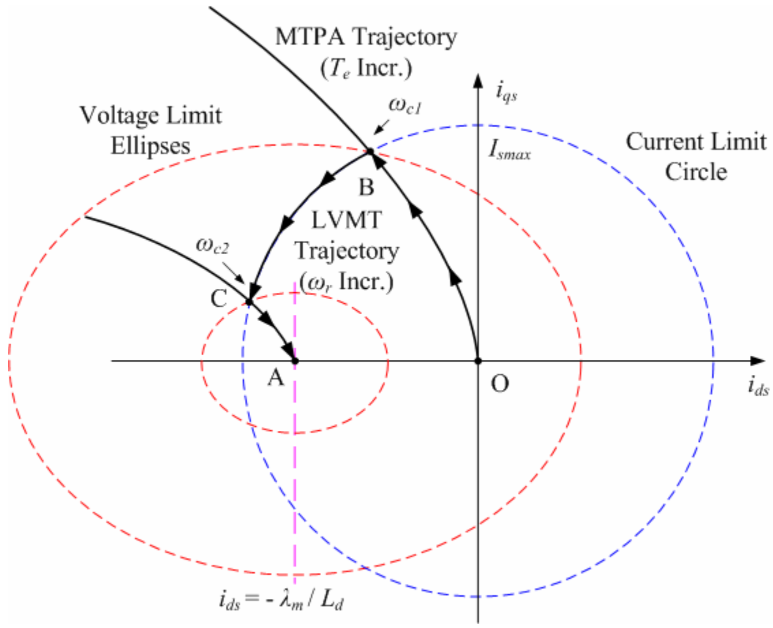

(a)

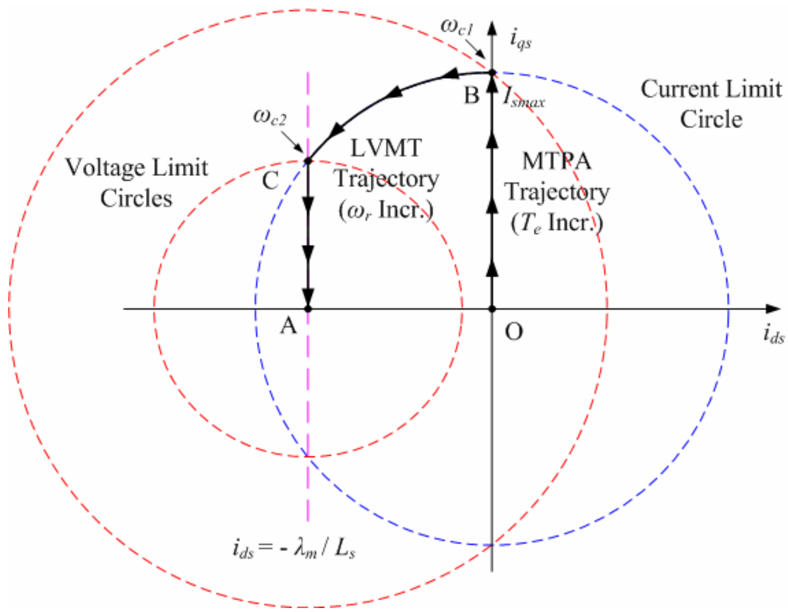

(b)

Figure 3.6: Current trajectories for MTPA and LVMT control of PM machines in the i_{ds}-i_{qs} plane: (a) with saliency; (b) without saliency.

3.6 Summary

In this chapter, mathematical models of PM machines are established in both stationary reference frame and the rotating reference frame with respect to the PM motors with and without saliency, e.g., IPM and SPM. By using the Park's transformation, all time-varying inductances in the voltage equations are eliminated and in turn the models are simplified and vector control algorithms can be implemented.

Constant-torque and constant-power operation are introduced in a PMSM drive system. After discussing the voltage and current constraints imposed by both power inverter and motor itself, the flux weakening of PM machines at high speeds is elaborated. Two constant-power control methods are reviewed.

Based on the vector control of PM machines, two optimal current control schemes can be achieved: one is the Maximum Torque per Ampere (MTPA) control and the other Limited-Voltage Maximum Torque control. By these means, the PM motor can operate with optimal efficiency at low speeds and deliver the maximum power in the flux-weakening region.

It is worth noting that the discussions in later chapters based on the developed models require adoption of a set of standard assumptions for linear magnetic circuits. Modification of the models to reflect the effects of magnetic saturation will not be included in this dissertation. Magnetic saturation effects clearly demand consideration if one is attempting to analyze the performance and design accurate control for the operations at low speeds. However, the net impact of saturation on motor performance is relatively smaller if the stator current is not quite large. At increasing speeds, the peak currents are limited due to the higher motor reactance and back-EMF magnitudes.

Therefore, the principles and concepts proposed in this dissertation are only weakly influenced by magnetic saturation, permitting its exclusion.

CHAPTER 4

FLUX-WEAKENING CONTROL OF PERMANENT MAGNET SYNCHRONOUS MACHINES

In this chapter, a robust flux-weakening control scheme of PM synchronous machines is studied. Based on a novel current control concept, a speed/flux-weakening controller (SFWC) is proposed for the flux-weakening control of PMSM. Comprehensive analysis is conducted on the operations of PMSM controlled by SFWC in the flux-weakening region. Small-signal method is used to investigate the flux and torque controllability of SFWC. The current vector trajectories are modeled and illustrated in the rotor reference frame, with special attention to SPM motors. Efficiency-optimized design is performed on the selection of a newly introduced voltage constant. Simulation and experimental results are provided to demonstrate the feasibility of the proposed control concept.

4.1 Practical Considerations on Flux-Weakening Control

More generally, flux-weakening control of PM machines is achieved through effective current regulation. The relationships between the current reference, torque command and rotor speed is preliminarily obtained by computer simulation based on the knowledge of machine parameters; and then stored in the memory of microprocessors as a lookup table. The current reference such as the direct-axis and quadrature-axis current command is determined by the required torque and the speed feedback using the lookup table. Alternatively, the current reference can be calculated on-line based on closed-form equations, e.g., equation (3.77), deducted from the machine model. To enforce the tracking of the current reference will then be the key to accomplishing the desired flux-weakening control.

However, the current regulators would be saturated and lose their controllability at high speeds due to the mismatch of the current reference under the limited operating conditions. Performance degradation, e.g., decreased maximum output torque or deteriorated dynamic response, would result associated with current regulator saturation. Moreover, the dc bus voltage may fluctuate caused either by line voltage sags/swells or change of the load. And the base speed of PMSM is severely influenced by the rotor flux linkage which varies with magnets' temperature and the quadrature-axis inductance subject to saturation with large excited currents. The stator resistance may enlarge much with temperature rise due to high demagnetizing current in the flux-weakening region and become non-negligible. Therefore, the onset of flux weakening operation and the demagnetizing current level should be selected adaptive to operating conditions and insensitive to variation of machine parameters.

In the real implementation of flux-weakening control algorithms, software execution time would pose problems due to the limited control bandwidth, especially in cost-effective drive systems employing low-end microprocessors or digital signal processors

(DSP). On the other hand, special efforts would be made to tune the current regulators, conventionally two PI regulators, and mitigate the cross-coupling effects between direct-axis and quadrature-axis current to improve dynamic performance and prevent saturation of the current regulation, which are prevailing at high speeds in the flux-weakening region.

4.2 Relationship of Direct-axis and Quadrature-axis Current in the Rotor Reference Frame

In general, the dynamic equations of a PMSM in the rotor reference frame can be given in the matrix form as

$$\begin{bmatrix} v_{ds} \\ v_{qs} \end{bmatrix} = \begin{bmatrix} R_s + pL_d & -\omega_r \cdot L_q \\ \omega_r \cdot L_d & R_s + pL_q \end{bmatrix} \cdot \begin{bmatrix} i_{ds} \\ i_{qs} \end{bmatrix} + \omega_r \lambda_m \cdot \begin{bmatrix} 0 \\ 1 \end{bmatrix} \tag{4.1}$$

where $L_d \neq L_q$.

In steady state, the equations reduce to

$$\begin{bmatrix} V_{ds} \\ V_{qs} \end{bmatrix} = \begin{bmatrix} R_s & -\omega_r \cdot L_q \\ \omega_r \cdot L_d & R_s \end{bmatrix} \cdot \begin{bmatrix} I_{ds} \\ I_{qs} \end{bmatrix} + \omega_r \lambda_m \cdot \begin{bmatrix} 0 \\ 1 \end{bmatrix} \tag{4.2}$$

Then, the electromagnetic torque of PMSM is expressed in terms of steady-state currents, i.e., I_{ds} and I_{qs}, as

$$T_e = \left(\frac{3}{2}\right)\left(\frac{P}{2}\right)\left[\lambda_m I_{qs} - (L_q - L_d) I_{qs} I_{ds}\right] \tag{4.3}$$

To SPM motors, the steady-state voltage equations are

$$\begin{bmatrix} V_{ds} \\ V_{qs} \end{bmatrix} = \begin{bmatrix} R_s & -\omega_r \cdot L_s \\ \omega_r \cdot L_s & R_s \end{bmatrix} \cdot \begin{bmatrix} I_{ds} \\ I_{qs} \end{bmatrix} + \omega_r \lambda_m \cdot \begin{bmatrix} 0 \\ 1 \end{bmatrix} \tag{4.4}$$

and the torque

$$T_e = \left(\frac{3}{2}\right)\left(\frac{P}{2}\right)(\lambda_m I_{qs}) \tag{4.5}$$

From (4.2) and (4.4), we can find the relationship between the direct-axis current I_{ds} and quadrature-axis current I_{qs} of PMSM, which is partially expressed in

$$I_{qs} = -\frac{\omega_r \cdot L_d}{R_s} I_{ds} + \frac{V_{qs} - \omega_r \lambda_m}{R_s} \tag{4.6}$$

or

$$I_{qs} = -\frac{\omega_r \cdot L_s}{R_s} I_{ds} + \frac{V_{qs} - \omega_r \lambda_m}{R_s} \tag{4.7}$$

Equations (4.6) and (4.7) can be rewritten into

$$I_{qs} = K_{i_q - i_d} I_{ds} + B_{i_q - i_d} \tag{4.8}$$

where the coefficients are

$$K_{i_q - i_d} = -\frac{\omega_r \cdot L_d}{R_s} \text{ or } K_{i_q - i_d} = -\frac{\omega_r \cdot L_s}{R_s}, \text{ and } B_{i_q - i_d} = \frac{V_{qs} - \omega_r \lambda_m}{R_s}.$$

It is clearly shown in (4.8) that the linear relationship exists between the steady-state currents I_{qs} and I_{ds} at a specific speed, i.e., when the rotor speed, ω_r, is constant but nonzero. This is regarded as the cross-coupling effect in PM motors. When the speed changes, this relationship still keeps on but the coefficient $K_{iq\text{-}id}$, i.e., $-\frac{\omega_r \cdot L_d}{R_s}$ or $-\frac{\omega_r \cdot L_s}{R_s}$, will be changed with the speed ω_r. It can be seen that the cross-coupling effect becomes stronger and stronger when the rotor speed goes higher, reflected by the increased coefficient. Therefore, in the flux-weakening region, the cross-coupling effect is dominant and should be dealt with properly for current regulation.

4.3 Conventional Current Regulation in Flux-Weakening Region

Conventionally, two current regulators are used to control the direct-axis and quadrature-axis current of PMSM respectively in the synchronous rotating reference frame. Thus both the magnitude and the angle of stator current vector can be controlled according to the vector control theory as discussed in Chapter 3. The type of current regulators is normally but not limited to proportional-integral (namely PI) controller. In a speed-controlled PMSM drive system, another speed regulator is required for the speed regulation, which is illustrated in Figure 4.1. The output of the speed regulator is the torque command based on the system mechanical dynamic equation specified by

$$\frac{d\omega_r}{dt} = \frac{1}{J}(T_e - T_L - B\omega_r) \tag{4.9}$$

where J is the inertia momentum of drive system; T_L is load torque; and B is viscous friction coefficient.

According to the given torque and operating speed, the direct-axis and quadrature-axis current reference can be obtained from (3.60) and (3.81), or (3.66) and (3.82).

On the principle of vector control, it is expected that the torque and the stator flux of PM machines can be controlled independently. To SPM motors, this is achievable through controlling the decoupled quadrature-axis and direct-axis current, i_{qs} and i_{ds}, respectively in the rotor reference frame. However, the current i_{qs} and i_{ds} can not be controlled independently due to the cross coupling effects, only by the voltage $v_{ds\text{-}PI}$ and $v_{qs\text{-}PI}$ which are the outputs of the two current regulators respectively, and expressed by

$$\begin{cases} v_{ds-PI} = k_p(1+\dfrac{1}{k_i s})(i^*{}_{ds} - i_{ds}) \\ v_{qs-PI} = k_p(1+\dfrac{1}{k_i s})(i^*{}_{qs} - i_{qs}) \end{cases} \tag{4.10}$$

where k_p is the proportional gain and k_i the integral constant of current PI-regulators.

Therefore, the dynamic performance of current response as well as torque response is strongly affected by the cross coupling effects in the high-speed flux-weakening region.

By using feedforward compensation [24], the cross coupling might be cancelled in the steady state as shown in Figure 4.1. Thus the voltage commands are determined by the outputs of current regulators and the decoupling feedforward compensation, $v_{ds\text{-}FF}$ and $v_{qs\text{-}FF}$:

$$\begin{cases} v_{ds-FF} = -\omega_r L_q i_{qs} \\ v_{qs-FF} = \omega_r \lambda_m + \omega_r L_d i_{ds} \end{cases}$$

or

$$\begin{cases} v_{ds-FF} = -\omega_r L_s i_{qs} \\ v_{qs-FF} = \omega_r \lambda_m + \omega_r L_s i_{ds} \end{cases} \tag{4.11}$$

Hence, the direct-axis and quadrature-axis current loops can be linearized by the above decoupling method.

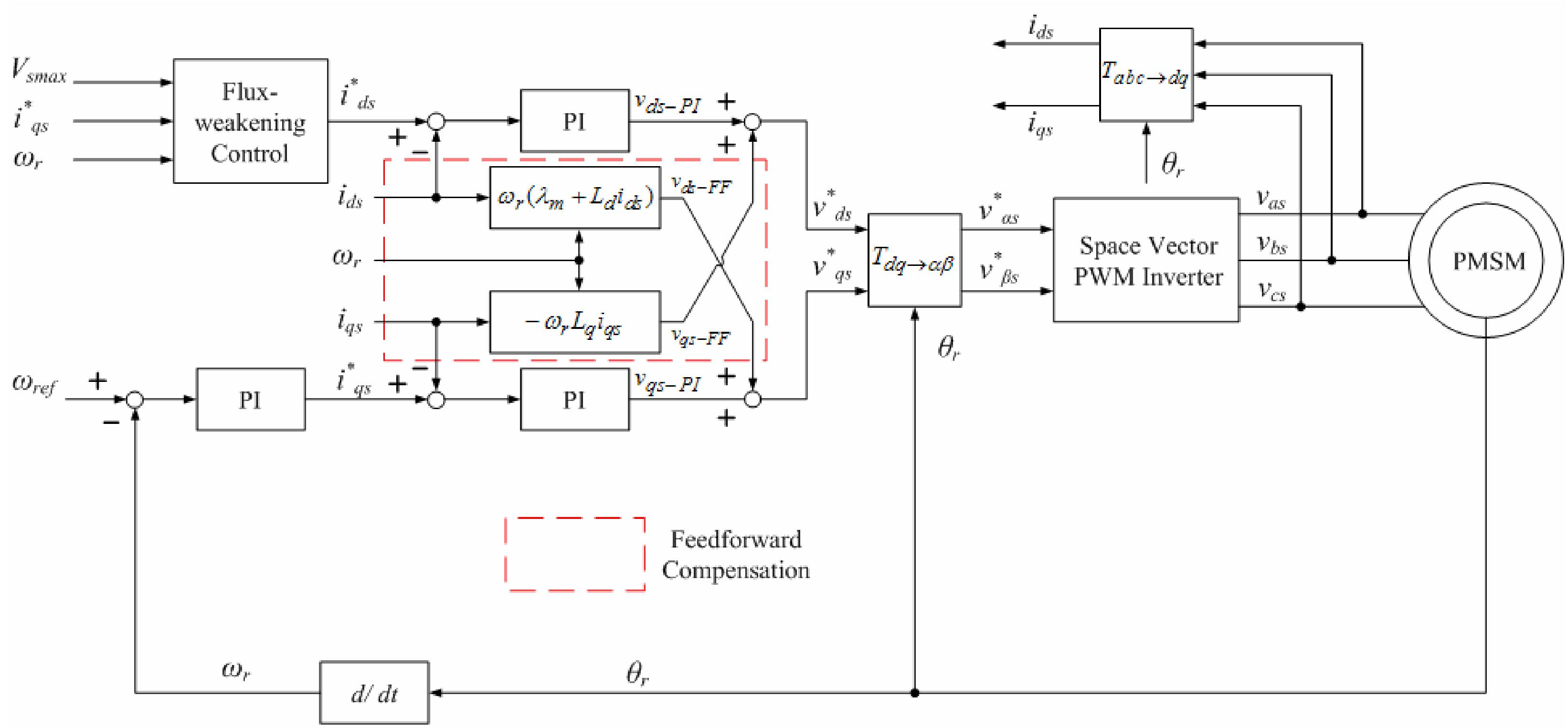

Figure 4.1 Block diagram of speed-regulated PMSM drive system with flux-weakening control.

4.4 Design of Speed/Flux-Weakening Controller

Define a positive voltage constant, V_{FWC}, which is less than the maximum phase voltage V_{smax}, i.e., $0 < V_{FWC} < V_{smax}$.

Let the quadrature-axis voltage of PMSM equal the voltage constant V_{FWC}. Considering (4.8), we get that all the following coefficients are constant at a given speed:

$$K_{i_q - i_d} = -\frac{\omega_r \cdot L_d}{R_s} \text{ or } K_{i_q - i_d} = -\frac{\omega_r \cdot L_s}{R_s},$$

and $B_{i_q - i_d} = \dfrac{V_{FWC} - \omega_r \lambda_m}{R_s}$.

As a result, the linear relationship between the steady-state currents I_{qs} and I_{ds} at the speed ω_r, as shown in (4.8), suggests a control strategy that the quadrature-axis current, or torque, can be controlled by means of controlling the direct-axis current. This, actually, utilizes the inherent cross-coupling effects inside the PM motor instead of cancelling them as in the system shown in Figure 4.1. By fixing the quadrature-axis voltage V_{qs}, the quadrature-axis current regulator can be eliminated. Therefore, only one direct-axis current regulator is required for the torque and flux control in the flux-weakening region. It should be noticed that this I_{ds}–based torque control method may work in the constant-torque region below the base speed but it would not be current-efficient, resulting in excessive copper losses.

Integrating speed regulation, a flux-weakening control scheme is illustrated in Figure 4.2 which includes a speed/flux-weakening controller, namely SFWC. A speed-regulated PMSM drive system including the SFWC is also shown in Figure 4.3. The speed/flux-weakening controller is designed with but not limited to a PI-regulator. The input of

SFWC is speed error, $\Delta\omega = \omega_{ref} - \omega_r$, and the output is the direct-axis current reference i^*_{ds}. The generated direct-axis current reference is negative, i.e., $i^*_{ds} < 0$, which consists of two components: one is the required demagnetizing current; and the other is the torque component referring to the demanded torque by the speed regulation through the cross coupling effect. It implies that the demagnetizing current can be automatically generated which is adaptive to the rotor speed and operating conditions such as load level or dc bus voltage. With applying the fixed quadrature-axis voltage v_{qs}, the direct-axis current is controlled by adjusting the direct-axis voltage v_{ds} through the direct-axis current regulator. Therefore, only two PI-regulators are used for both flux and speed (or torque) control while three PI-regulators used as shown in Figure 4.1.

The transfer function of the speed/flux-weakening controller can be expressed as

$$i^*_{ds} = -k_{p\_FWC}\left(1 + \frac{1}{k_{i\_FWC} \cdot s}\right)(\omega_{ref} - \omega_r) \tag{4.12}$$

where k_{p_FWC} and k_{i_FWC} are the proportional gain and the integral constant respectively.

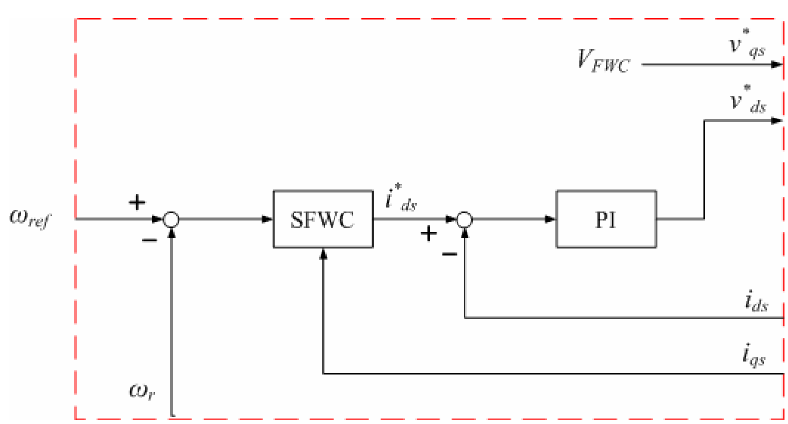

Figure 4.2: Block diagram of flux-weakening control with SFWC.

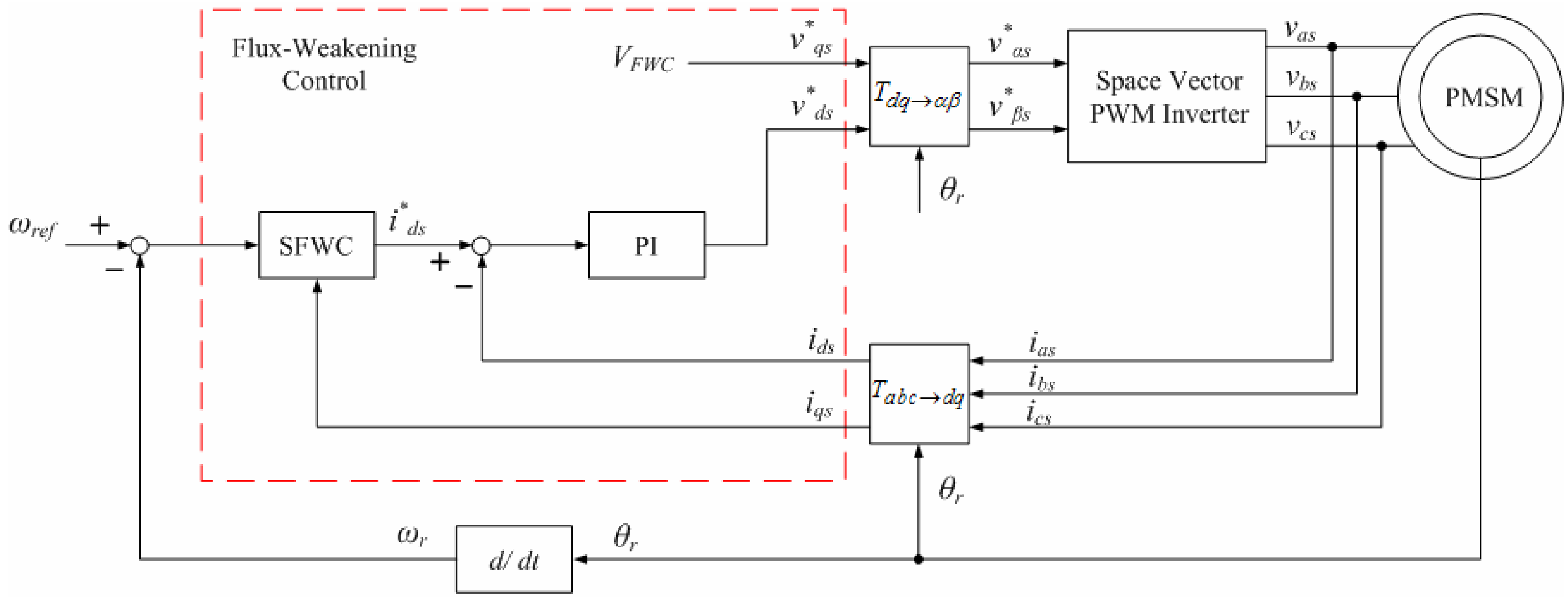

Figure 4.3 Block diagram of speed-regulated PMSM drive system with SFWC in the flux-weakening region.

4.5 Analysis of Flux and Torque Controllability of SFWC

By substituting V_{qs} with the voltage constant V_{FWC}, the equations in (4.2) are rearranged in the expanded form as

$$V_{ds} = R_s I_{ds} - \omega_r L_q I_{qs} \tag{4.13}$$

$$V_{FWC} = R_s I_{qs} + \omega_r (L_d I_{ds} + \lambda_m) \tag{4.14}$$

From (4.14), the quadrature-axis current I_{qs} can be expressed as

$$I_{qs} = -\frac{\omega_r \cdot L_d}{R_s} I_{ds} + \frac{V_{FWC} - \omega_r \lambda_m}{R_s} \tag{4.15}$$

Under no load condition, i.e., $I_{qs} = 0$, the required direct-axis current I_{ds} at the given speed ω_r will be

$$I_{ds,I_{qs}=0} = I_{ds,0} = \frac{V_{FWC} - \omega_r \lambda_m}{\omega_r \cdot L_d} = -\frac{\lambda_m}{L_d} + \frac{V_{FWC}}{L_d} \cdot \frac{1}{\omega_r} \tag{4.16}$$

where $I_{ds,0}$ is the required demagnetizing current at the speed ω_r with respect to $V_{qs} = V_{FWC}$. It is seen that $I_{ds,0}$ is inversely proportional to the speed. This is similar to the flux-weakening operation of other electric machines such as induction machines. When the speed is high enough to satisfy the condition $V_{FWC} << \omega_r \lambda_m$, the demagnetizing current $I_{ds,0}$ will approach the limit value $-\lambda_m/L_d$, regardless of V_{FWC}. It is equivalent to

$$\lim_{\omega_r \to \infty} I_{ds,0} = -\frac{\lambda_m}{L_d} \tag{4.17}$$

Figure 4.4 shows the relationship between the required demagnetizing current $I_{ds,0}$ and the speed ω_r.

For the flux-weakening operation of PMSM, the demagnetizing current is expected to be negative, i.e., $I_{ds,0} < 0$. So the minimum speed ω_{FWC} for the flux weakening is calculated:

$$\omega_{FWC} = \frac{V_{FWC}}{\lambda_m} \tag{4.18}$$

It is explained by (4.18) that when the back-EMF equals the preset quadrature-axis voltage $V_{qs} = V_{FWC}$ under no load condition should be the time of onset for the flux weakening operation.

Furthermore, equation (4.15) can be rewritten in terms of $I_{ds,0}$ into

$$I_{qs} = -\frac{\omega_r \cdot L_d}{R_s}(I_{ds,0} + I_{ds,T}) + \frac{V_{FWC} - \omega_r \lambda_m}{R_s} \tag{4.19}$$

where $I_{ds} = I_{ds,0} + I_{ds,T}$ and $I_{ds,0}$ represents the demagnetizing component with respect to operating speed ω_r, while $I_{ds,T}$ represents the torque component of the direct-axis current.

Applying small-signal method allows the analysis of the torque controllability of PMSM based on the fixed-V_{qs} control concept.

From (4.14), the deviation of I_{qs} can be expressed in terms of that of I_{ds} as

$$\Delta I_{qs} = -\frac{\omega_r L_d}{R_s}\Delta I_{ds} \tag{4.20}$$

Similarly, we can obtain from (4.13) that

$$\Delta V_{ds} = R_s \Delta I_{ds} - \omega_r L_q \Delta I_{qs} = R_s(-\frac{R_s}{\omega_r L_d}\Delta I_{qs}) - \omega_r L_q \Delta I_{qs} = -\Delta I_{qs}(\frac{R_s^{\ 2} + \omega_r^{\ 2} L_d L_q}{\omega_r L_d})$$

$$\Rightarrow \Delta V_{ds} = -\Delta I_{qs}\frac{Z_s^{\ 2}}{X_d}$$

(4.21)

where $Z_s = \sqrt{R_s{}^2 + \omega_r{}^2 L_d L_q}$ is called as equivalent phase impedance in this dissertation; and $X_d = \omega_r L_d$ as direct-axis reactance.

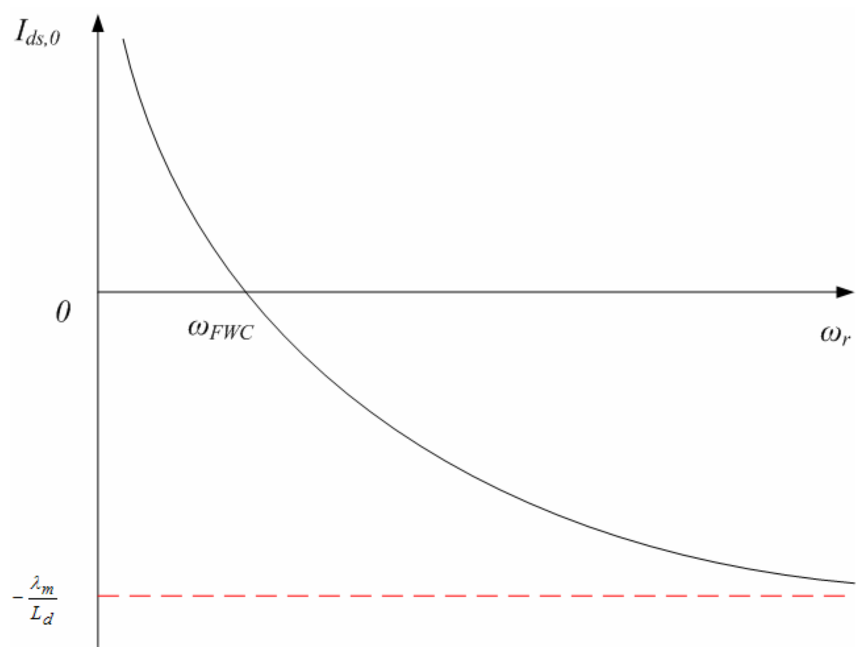

Figure 4.4: Relationship between the required demagnetizing current $I_{ds,0}$ and speed ω_r.

To simplify the further discussion, we now focus on SPM motors. Then, the inductance $L_s = L_d = L_q$ and $X_s = X_d = \omega_r L_s$.

According to (4.5), the torque variation is of

$$\Delta T_e = \left(\frac{3}{2}\right)\left(\frac{P}{2}\right)(\lambda_m \Delta I_{qs}) \tag{4.22}$$

Substituting (4.21) into (4.22), we get

$$\Delta T_e = \left(\frac{3}{2}\right)\left(\frac{P}{2}\right)(\lambda_m \frac{X_s}{Z_s{}^2})\Delta V_{ds} \tag{4.23}$$

Therefore, the above relationship hints at the possibility of controlling the torque by controlling I_{ds} and eventually through adjusting direct-axis voltage V_{ds}.

When the speed is high and $R_s << X_s$, i.e., $Z_s \approx X_s$, (4.23) is approximately expressed as

$$\Delta T_e = \left(\frac{3P}{4} \cdot \frac{\lambda_m}{L_s}\right)\left(\frac{1}{\omega_r}\right)\Delta V_{ds} \tag{4.24}$$

It indicates that the control gain of the torque T_e by V_{ds} decreases when the speed increases. Theoretically, the gain will be zero when the speed goes infinite, implying no cross coupling exists any more and then the torque cannot be controlled by V_{ds}. Hence, the torque controllability of SFWC will become weak with speed increasing. Accordingly, higher proportional gain k_p of current PI-regulator may be demanded for the same fast dynamic performance in the flux-weakening region as at lower speeds.

Let's look at another scenario, assuming $V_{ds} = V_{FWC}$.

Equations (4.13) and (4.14) then change to

$$V_{FWC} = R_s I_{ds} - \omega_r L_s I_{qs} \tag{4.25}$$

$$V_{qs} = R_s I_{qs} + \omega_r (L_s I_{ds} + \lambda_m) \tag{4.26}$$

And the direct-axis current I_{ds} can be expressed as

$$I_{ds} = \frac{\omega_r \cdot L_s}{R_s} I_{qs} + \frac{V_{FWC}}{R_s} \tag{4.27}$$

By the small-signal method, we get

$$\Delta I_{ds} = \frac{\omega_r L_s}{R_s} \Delta I_{qs} \tag{4.28}$$

$$\Delta V_{qs} = \Delta I_{ds} \frac{{Z_s}^2}{X_s} \tag{4.29}$$

Although equation (4.27) shows the linear relationship between I_{qs} and I_{ds} as well as (4.29) showing the possibility of flux control by V_{qs} , the fixed-V_{ds} method is subject to saturation of current regulation due to the positive feedback of load disturbance, leading to the limited flux-weakening operation [15]. For example, a SPM motor operates at a maintained speed in the flux-weakening region, corresponding to Point M as shown in Figure 4.5. When the load increases, i.e., $\Delta I_{qs} > 0$, the variation of I_{ds} will increase accordingly, resulting in the reduced magnitude of I_{ds}. Consequently the operating point will move toward outside the voltage-limited circle and eventually to a saturation point on the voltage-limited circle, Point N1. On the contrary, with the fixed-V_{qs} method, the operating point will move to Point N2 under the same load disturbance, which is still in the effective operating area in the i_{qs}-i_{ds} plane determined by both current and voltage constraints without any degradation of torque production.

In addition, the demagnetizing current I_{ds}, generated by the fixed-V_{ds} method, is constant and reaches its maximum value when I_{qs}=0, regardless of speed. This makes the motor suffer from low-efficiency operation and potential over-heating problem at lower speed with light or zero load.

Therefore, the fixed-V_{ds} method is not applicable for the flux-weakening control of PMSM.

It should be noted that, in this dissertation, PM machines are assumed to operate normally in motoring mode in the flux-weakening region, which relates to the operating points in the second quadrant of the i_{qs}-i_{ds} plane. As to regenerating or braking mode, some conclusions drawn in this section would be thought opposite.

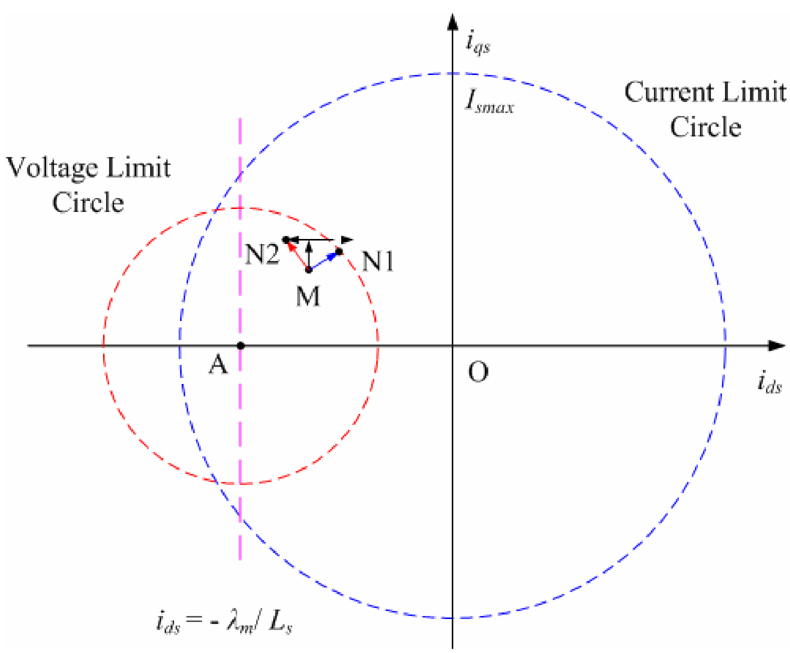

Figure 4.5: Illustration of operating point change of PMSM under load disturbance in the flux-weakening region.

4.6 Current Trajectory of PMSM Controlled by SFWC

The current trajectory of PMSM controlled by SFWC is specified by (4.15) and shown in Figure 4.6. The stator current vector moves along a straight line in the i_{qs}-i_{ds} plane between two points (i.e., Point M1 and E1) where the line crosses the voltage-limited ellipse/circle and the horizontal axis, i_{ds}-axis, respectively when the torque varies from zero to the available maximum at a given speed. From (4.15), the slope gradient of the line is $-\omega_r L_d / R_s$; and its intercept on the vertical line $i_{ds} = -\lambda_m / L_d$ is V_{FWC} / R_s . So the coordinate of the intercept Point F is ($-\lambda_m / L_d$, V_{FWC} / R_s). It can be seen that the location of Point F is fixed in the plane and not dependent on the rotor speed. The intercept on the i_{ds}-axis refers to Point E1 with coordinate ($I_{ds,0}$, 0), which moves away from the vertical axis, i_{qs}-axis, with the speed ω_r increasing. Point M1 is the point where the line crosses the voltage-limited ellipse/circle in the second quadrant. This straight line is sometimes called load line with respect to a specific rotor speed in this chapter.

In Figure 4.6, the constant-torque curve is also plotted (in bold dashed line), which is a horizontal line for SPM motors while a branch of hyperbola for IPM motors. Point S is the crossing point of the torque curve and the voltage-limited circle/ellipse, closer to the vertical axis than the other one. Point M is on the intersection of the two limit curves in the second quadrant.

For example, the current vector moves along the load line from Point E1 to M1 at speed ω_1 with torque T_e changing from zero to the allowable maximum. When the torque current equals i^*_{qs} at steady state, the PMSM will be running at the operating Point S1. It is noticeable that Point S is the ideal operating point regarding the minimum current at the given torque, namely "minimum-ampere-at-torque", with respect to speed ω_1. With the load increasing, Point S1 moves up and gets close to Point S and eventually meets Point S at Point M1. Point E1 indicates the minimum demagnetizing current required by the flux weakening operation at speed ω_1 under the control of SFWC. Point M1 is the operating point of the allowable maximum torque at speed ω_1, which is related to the location of Point F.

In addition, an ideal current trajectory is drawn in dotted-dash line, which is the circular segment of the voltage-limited curve intercepted by the current-limited circle in the second quadrant. On the ideal trajectory, the PM motor operates most efficiently with respect to the produced torque at a given speed. In other words, the magnitude of current vector is the smallest among all achievable operating points on the constant-torque curve. Moreover, the demagnetizing current for the flux weakening operation will be the minimum on the ideal current trajectory under same load condition.

Figure 4.7 shows the current trajectory of PMSM when speed increases from ω_1 to ω_2 , and the torque T_e keeps the same. As a consequence, the operating point moves from Point S1 to S2 along the constant torque curve. And the magnitude of the demagnetizing currents increases accordingly adaptive to the speeds.

Current trajectory of SPM controlled by SFWC with variation of dc bus voltage is shown in Figure 4.8. The dc bus voltage drops from V_{dc1} to V_{dc2}. Consequently, the operating point moves from Point S1 to S2 along the constant torque curve.

Current trajectory of PMSM is shown in Figure 4.9 with the load-torque increase from T_{e1} to T_{e2} at a specific speed. The operating point then moves from Point S1 to S2 along the load line.

From Figure 4.7 through 4.9, it is clearly seen that the speed/flux-weakening controller is able to work adaptive to rotor speed and other operating conditions such as the dc bus voltage and load level.

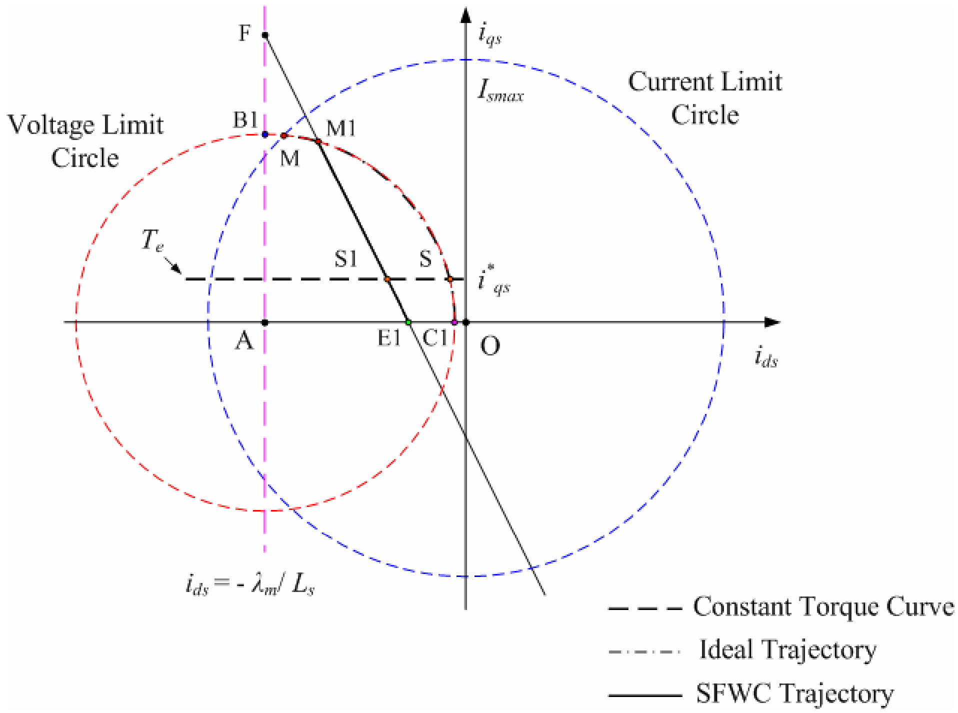

(a)

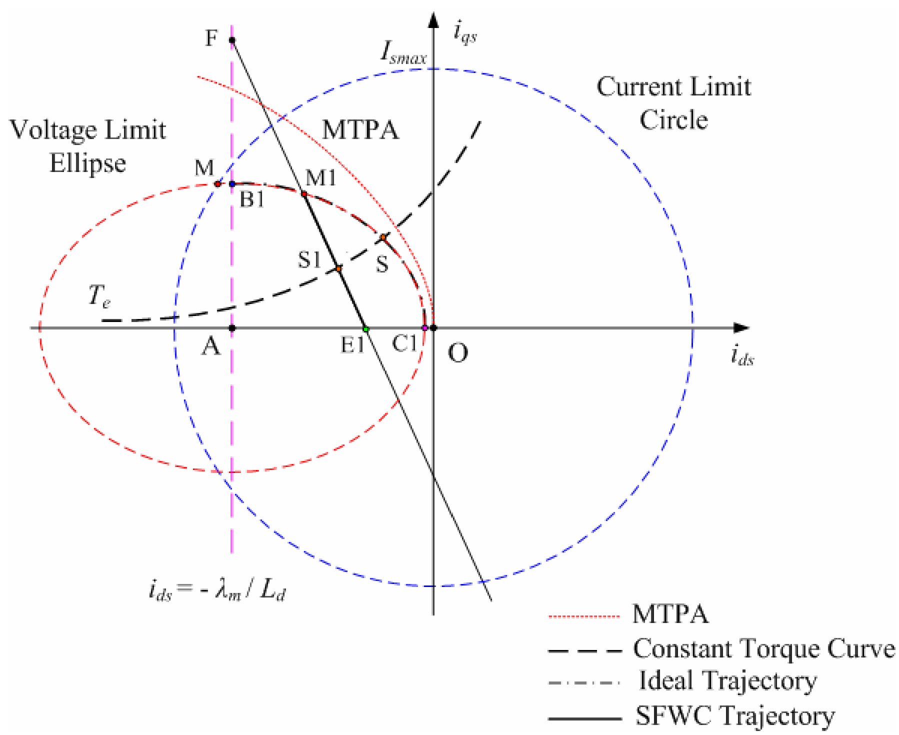

(b)

Figure 4.6: Current trajectory of PMSM controlled by SFWC:

(a) SPM; (b) IPM

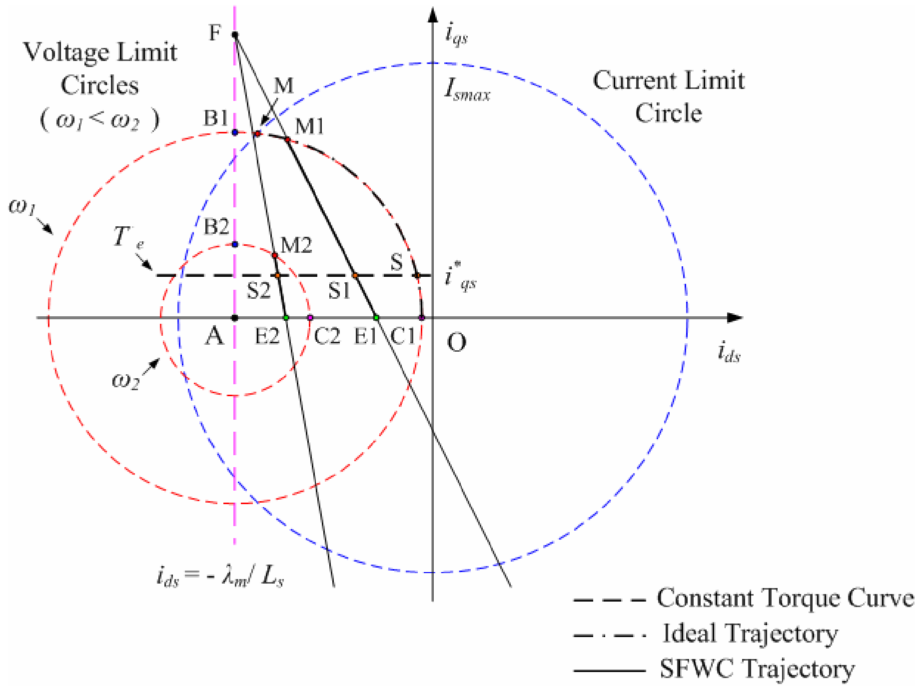

(a)

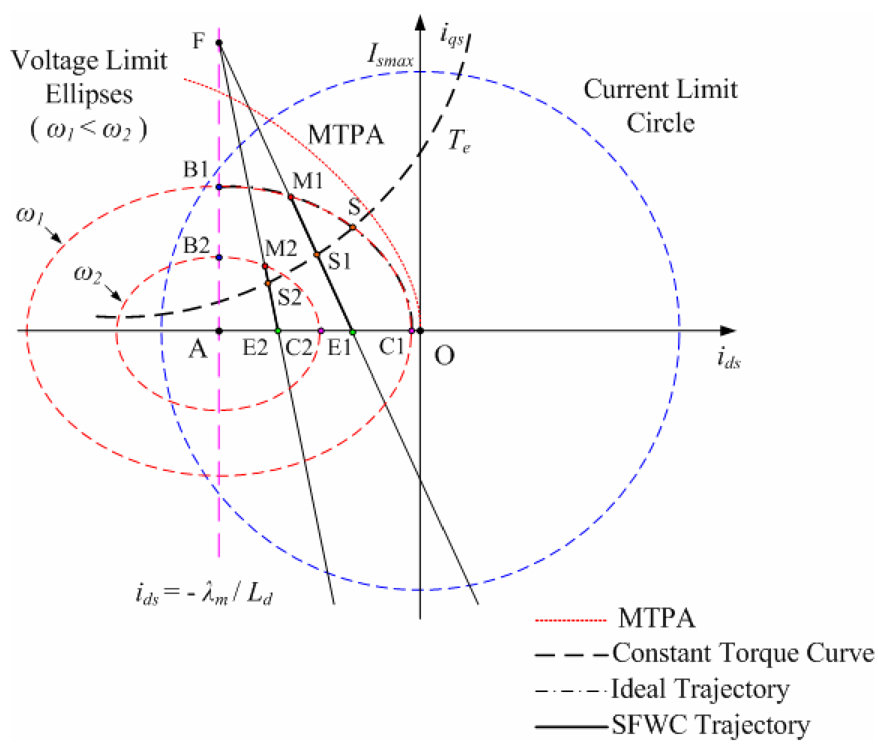

(a)

Figure 4.7: Current trajectory of PMSM controlled by SFWC with speed increase:

(a) SPM; (b) IPM

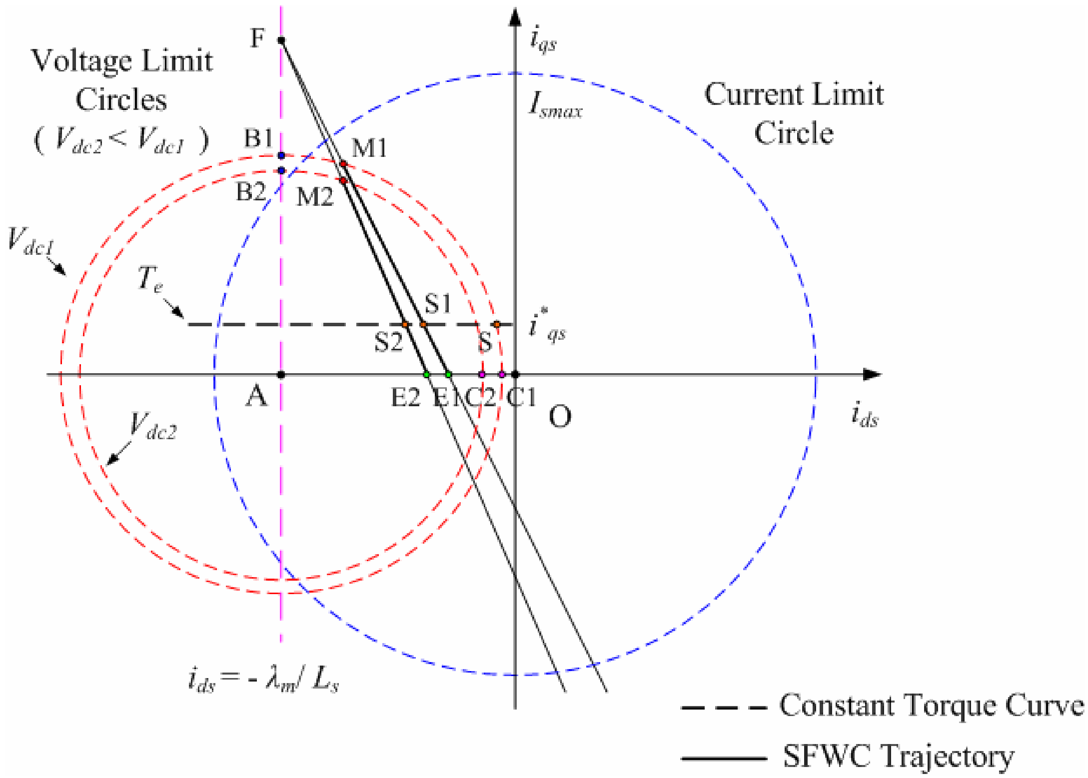

Figure 4.8: Current trajectory of SPM controlled by SFWC with variation of dc bus voltage.

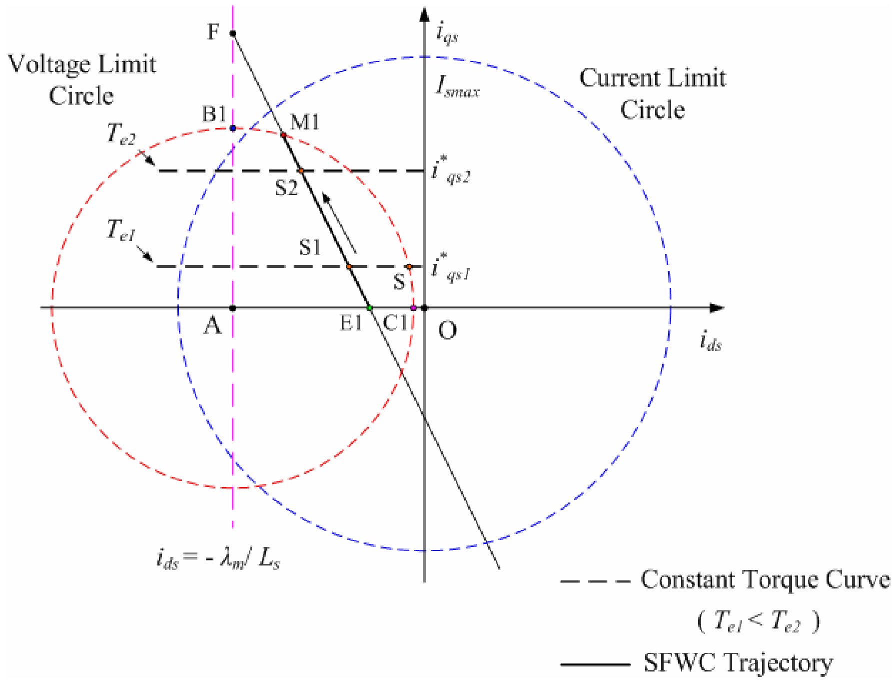

(a)

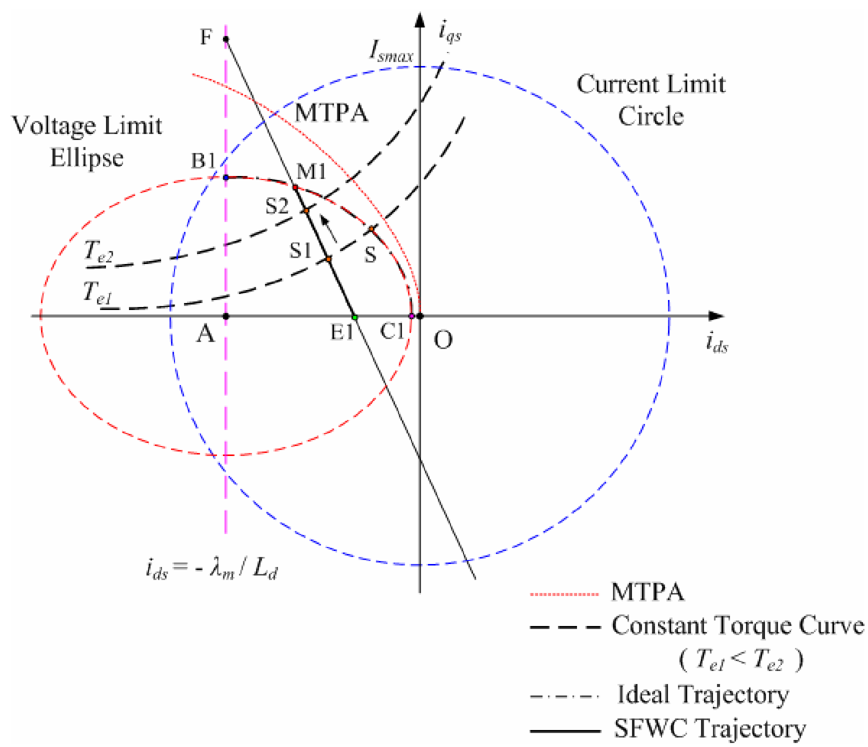

(b)

Figure 4.9: Current trajectory of PMSM controlled by SFWC with torque increase:

(a) SPM; (b) IPM.

4.7 Discussion on the Selection of Voltage Constant V_{FWC}

Now, we know that the location of Point M1 and E1 in the i_{qs}-i_{ds} plane reflects the allowable maximum torque and the required minimum demagnetizing current of PMSM controlled by SFWC at the given speed ω_1.

The coordinates of the two boundary points are listed in Table 4.1 as well as other meaningful intercept points with respect to SPM motors.

SFWC mode	i_{ds}	i_{qs}	Ideal mode	i_{ds}	i_{qs}
E1	$-\lambda_m / L_s + V_{FWC} / \omega_r L_s$	0	C1	$-\lambda_m / L_s + V_{smax} / \omega_r L_s$	0
M1	i_{ds1_M1}	i_{qs1_M1}	M	i_{ds1_M}	i_{qs1_M}
S1	i_{ds1_S1}	i^*_{qs1}	S	i_{ds1_S}	i^*_{qs1}
B1	$-\lambda_m / L_s$	$V_{smax} / \omega_r L_s$	A	$-\lambda_m / L_s$	0
F	$-\lambda_m / L_s$	V_{FWC} / R_s	O	0	0

Table 4.1: Coordinates of characteristic points in the i_{qs}-i_{ds} plane.

Note:

$$i_{ds1\_M} = \frac{1}{2}\left(\frac{(V_{s\max}/(\omega_r L_s))^2 - I_{s\max}^2}{\lambda_m / L_s} - \lambda_m / L_s \right)$$

$$i_{qs1\_M} = \sqrt{I_{s\max}^2 - \frac{1}{4}\left(\frac{(V_{s\max}/(\omega_r L_s))^2 - I_{s\max}^2}{\lambda_m / L_s} - \lambda_m / L_s \right)^2}$$

$$i_{ds1\_M1} = \frac{1}{2}\left(\frac{(V_{s\max}/(\omega_r L_s))^2 - I_{s\max}^2}{\lambda_m / L_s} - \lambda_m / L_s \right)$$

$$i_{qs1\_M1} = \frac{R_s V_{FWC} + \sqrt{V_{s\max}^2 [R_s^2 + (\omega_r L_s)^2] - V_{FWC}^2 (\omega_r L_s)^2}}{R_s^2 + (\omega_r L_s)^2}$$

$$i_{ds1\_S} = \frac{\sqrt{V_{s\max}^2 - (\omega_r L_s \cdot i^*{}_{qs1})^2}}{\omega_r L_s} - \lambda_m / L_s$$

$$i_{ds1\_S1} = \frac{V_{FWC} - R_s i^*{}_{qs1}}{\omega_r L_s} - \lambda_m / L_s$$

Observing the current trajectory shown in Figure 4.6, we can easily find that the necessary condition for the flux-weakening operation of PM motor: graphically Point E1 should be in the effective operating area contoured by both the current and voltage limit circles with respect to operating speed. It implies that Point E1 is on the left to Point C1 which is the ideal point on the boundary. By the help of the coordinates of Point E1 and C1, it can be mathematically expressed in

$$\begin{cases} \frac{V_{FWC}}{\omega_r L_s} - \lambda_m / L_s \le \frac{V_{s\max}}{\omega_r L_s} - \lambda_m / L_s \\ -I_{s\max} \le \frac{V_{FWC}}{\omega_r L_s} - \lambda_m / L_s \end{cases} \quad \text{i.e.,}$$

$$\omega_r \lambda_m - (\omega_r L_s) I_{s\max} \le V_{FWC} \le V_{s\max} \tag{4.30}$$

Equivalently, with definition of a new voltage factor, *m*, the above condition can be rewritten as

$$V_{FWC} = m V_{s\max} \qquad (m \le 1) \tag{4.31}$$

Normally, we consider the range $(0 < m < 1)$ for the analysis of PM machines in motoring mode in this dissertation.

When the voltage constant V_{FWC} becomes larger, Point F (above B1) will move up and Point E1 right toward Point C1. Also Point M1 slides down the voltage-limited circle. As a result, the demagnetizing current component with respect to torque decreases and the maximum torque by SFWC is reduced too under same current and voltage constraints.

It can thus be concluded that the voltage constant V_{FWC} is larger, the efficiency of the SFWC-controlled PMSM is higher due to less copper losses; but the available maximum torque smaller resulting in the reduced output power at high speeds.

Therefore, there is a tradeoff on selecting the voltage constant between the maximum torque capability and the operation efficiency of PMSM. According to the specified torque/load profile with speeds, V_{FWC} can be properly selected to meet the system requirement for both torque and efficiency.

As the speed ω_r goes higher and higher such that the radius of the voltage-limited circle is nearly zero, both Point C1 and E1 will approach Point A fast and meanwhile Point M1 to B1. Then the effect of the voltage constant on the maximum torque and efficiency will play less even little role than that at lower speeds. For the motors with the feature of $\lambda_m / L_s < I_{smax}$, i.e., graphically Point A locates inside the current-limited circle, the voltage limit will eventually dominates and then the efficiency and maximum torque of PMSM not be effected much at high speeds by the voltage constant in the speed/flux-weakening controller.

It should be noted that the stator resistance is neglected in the formulation of the voltage-limited ellipses/circles when discussing the current trajectories of PMSM. Considering the effect of resistance on the flux-weakening operation, especially at high speeds, is beyond the scope of this chapter. But it will be listed for the future work to continue the investigation of the proposed control concept.

In the following, two examples will be given for the optimized design of SFWC based on the selection of V_{FWC}, considering either torque controllability or optimal operation efficiency of PMSM in the flux-weakening region.

The design optimization of SFWC can be formulated as a general nonlinear programming problem such that optimal solutions exist. Here, the principle variable is selected as the voltage constant V_{FWC} and performance constraints are the current and voltage limits. The objective function can be either the torque or the operation efficiency to be maximized. Quite a few comprehensive optimization techniques are available to obtain solutions to the derivatives of objective functions, which, however, may take excessive computation efforts and become time-consuming due to their mathematical complexities. Differently, we can simplify this procedure using an intuitive graphic method based on current trajectories, which is understandable and easily performed. It can be proven that optimization results by the graphic method are equivalent to those from closed-form solutions to the derivatives of objective functions.

Design-A:

To explore the allowable maximum torque under the current and voltage constraints, the voltage constant V_{FWC} can be selected as a function of rotor speed:

$$V_{FWC} = \frac{V_{s\max}}{(\omega_r L_s)/R_s} \tag{4.32}$$

As it is, in the i_{qs}-i_{ds} plane, Point F1 will be with the same coordinates as Point B1 at speed ω_1, which is the ideal operating point with allowable maximum torque in the flux-weakening region. It implies the fast response in transient due to the largest available torque, resulting in good dynamic performance of speed regulation.

However, with light load and/or at lower speeds, the motor efficiency is low in this case due to more copper losses generated than that of PMSM operating at the related points such as Point S on the ideal current trajectory as shown in Figure 4.6.

Figure 4.10 shows the current trajectories of SPM motor with allowable maximum torque.

Design-B:

Operation efficiency of PMSM can be optimized by selecting the voltage constant V_{FWC} adaptive to the load level, related to the feedback of the steady-state quadrature-axis current I_{qs}. The principle of this optimization is to use high-value V_{FWC} when the load is light while smaller V_{FWC} for heavy loads. The relationship between the constant V_{FWC} and current I_{qs}.is

$$V_{FWC} = I_{qs}(R_s - h \cdot \omega_r L_s) + hV_{s\max} \qquad (0.8 < h < 1) \tag{4.33}$$

It can be seen that the maximum value of V_{FWC} is hV_{smax} when $I_{qs} = 0$. The factor h is determined by the voltage margin due to fluctuations of dc bus voltage and/or ohmic drop on stator resistors, which is normally in the range of $0.8 < h < 1$. When the torque reaches its allowable maximum, the value of V_{FWC} equals

$$V_{FWC,\min} = \frac{R_s}{\omega_r L_s} V_{s\max}$$

which is the minimum value with respect to the operating speed ω_r. It varies with the speed and changes little when the speed is high such that $R_S << \omega_r L_s$. In the real implementation, the coefficient of I_{qs} in (4.33) can be properly design with a constant ρ and then the equation (4.33) is simplified by using linear relationship as

$$V_{FWC} = \rho \cdot I_{qs} + hV_{s\max} \qquad (0.8 < h < 1) \tag{4.34}$$

Figure 4.11 shows the current trajectory of SPM motor with optimized operation efficiency. When the voltage constant V_{FWC} is selected in accordance with (4.33), Point F1 will move along the vertical line $i_{ds} = -\lambda_m / L_s$ between its highest location, Point F, and Point B, which relates to the maximum and minimum value of V_{FWC} respectively. So does Point E1 between Point E and E'1. The current trajectory is then formed by intersection of constant-torque curves and a set of load lines in parallel with respect to different V_{FWC} at the given speed ω_r. It is clearly seen that the magnitude of current vector $\boldsymbol{i}_{s1}$ is smaller than that of $\boldsymbol{i'}_{s1}$ with the same produced torque as T_{e1}, which effects both iron and copper losses in the motor. Therefore, the motor efficiency at Point S1 is comparatively higher than at Point S′1. For the allowable maximum torque, T_{e2} as shown in Figure 4.11, the operating point is designed to Point B where Point F1, M1 and S1 merge together for the ideal operation with optimal efficiency and torque productivity.

It should be noted that the optimization by (4.33) is able to improve the operation efficiency of PMSM in steady state compared with in the constant V_{FWC} -based design or *Design-A*. Nevertheless, there is still margin (as seen from Figure 4.11) to further improve the operation efficiency by extending this design methodology so as to achieve the optimal efficiency regardless of operating speed and load level.

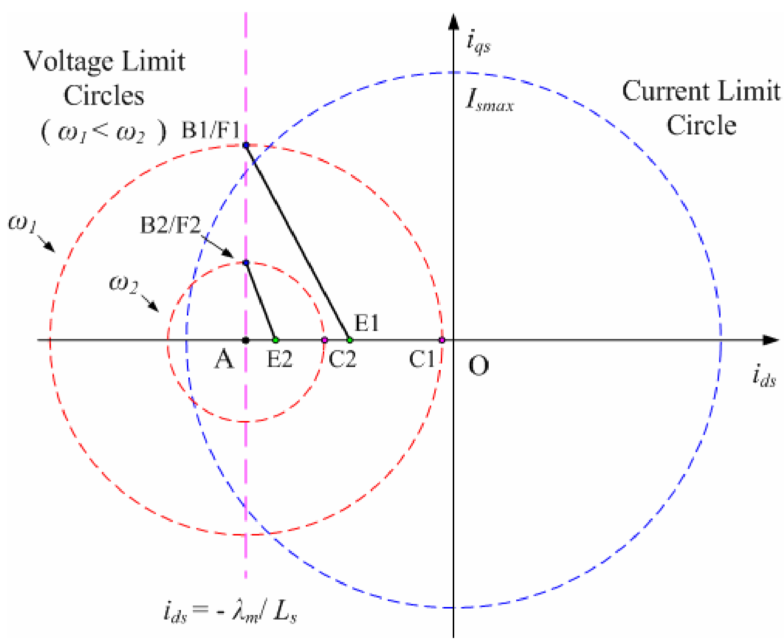

Figure 4.10: Current trajectories of SPM motor with allowable maximum torque.

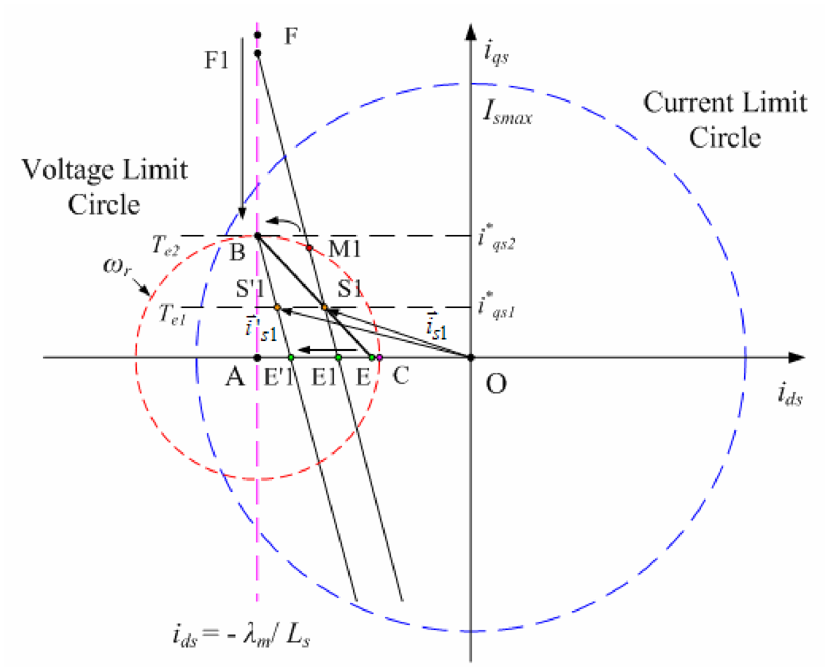

Figure 4.11: Current trajectory of SPM motor with optimized operation efficiency.

4.8 Simulation and Experimental Results

4.8.1 Simulation results

Computer simulations have been conducted to verify the control performance of the speed/flux-weakening controller. Matlab/Simulink® with SimPowerSystems Blockset is used as simulation platform. A Simulink model of PMSM drive system including SFWC is built and shown in Appendix A. The machine parameters of the simulated SPM motor and drive system are given in Table 4.2. And the simulation parameters of Simulink are given in Table 4.3.

SPM	Value (Unit)	System	Value (Unit)
R_s	16 (Ω)	Vdc	310 (V)
L_s	60 (mH)	f_{PWM}	20 (kHz)
λ_m	0.2232 (Wb)	PWM	SVPWM
P	24 (pair)	J	0.04 (kg.m^2)
I_{base}	7 (A)	B	0.005 (N.m.s)
f_{base}	500 (Hz)		
n_{base}	1,250 (rpm)		

Table 4.2: Parameters of the simulated SPM motor and drive system.

Solver Type:	Variable-step	Ode23t [Modified Stiff/trapezoidal]	
Max step size	1e-6	Relative tolerance	1e-4
Min step size	auto	Absolute tolerance	auto
Initial step size	1e-6		

Table 4.3: Simulation parameters of Simulink.

Figure 4.12 and Figure 4.13 show the simulation results in which the motor is first accelerated from 0 to 1,000 rpm and then stays for 0.5 second and finally decelerates down to 0 rpm without load. The rate of acceleration is the same as that of deceleration. The onset of flux-weakening operation is set at speed 0.18 in per unit. The voltage constant is set with $V_{FWC} = 0.5$ in per unit, i.e., $m = 0.5$ as defined in (4.31), for the speed/flux-weakening controller.

The dc bus voltage is 310V consistently. We can observe the automatically generated demagnetizing current i_{ds} by SFWC and its good performance of speed regulation within the wide speed range in the flux-weakening region.

It should be noticeable that current transients exist during the transition from normal to flux-weakening operation of the SPM motor and vice versa. A straightforward method is used for initiating the transition, by which the speed/flux-weakening controller is activated once the motor speed reaches the preset onset speed during acceleration and inversely deactivated during deceleration. A smooth transition can be made by advanced control algorithms which, however, may not be the interest of this dissertation.

Figure 4.14 shows the robustness of the simulated drive system with respect to disturbances from load and dc bus voltage. In the simulation, the SPM motor is accelerated from 0 to 500 rpm and maintains at this speed after the time t =1.75 s. The dc bus voltage is initially 310V and increased to 320V with a ramp from t =2.0 to 2.2 s, and then decreases to 280V gradually where the dc bus voltage stays thereafter. The load torque is initially 0 N.m and stepped to 1 N.m at time t =2.5 s. We can observe that the speed error is much less than 0.001 in per unit at 500 rpm, which refers to 1.25 rpm, in both steady state and transient in the flux-weakening region. It indicates that the speed regulation in the flux-weakening region functions very well with either dc bus or load disturbance. The proposed speed/flux-weakening controller is therefore proven to be adaptive to variations of dc bus voltage and load level.

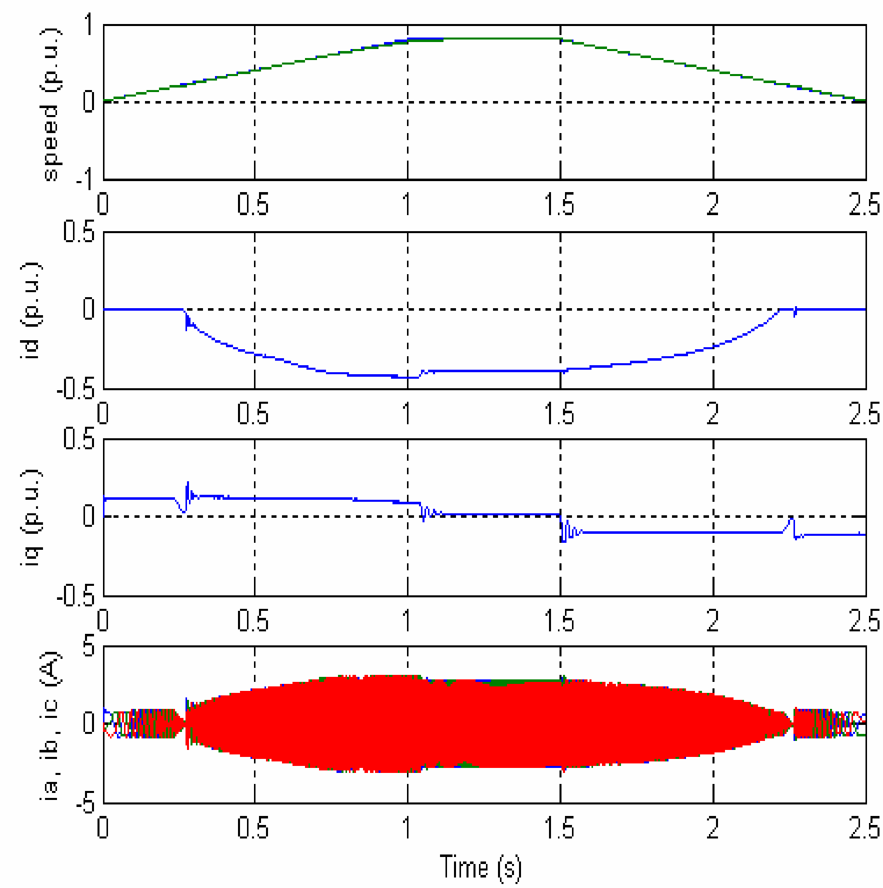

Figure 4.12: Simulation results of SPM with speed ramping up and down: speed command ω^*_r and feedback ω_r (top), i_{ds} (2nd), i_{qs} (3rd) and three-phase stator current i_{as}, i_{bs}, i_{cs} (5.0 A/div, bottom).

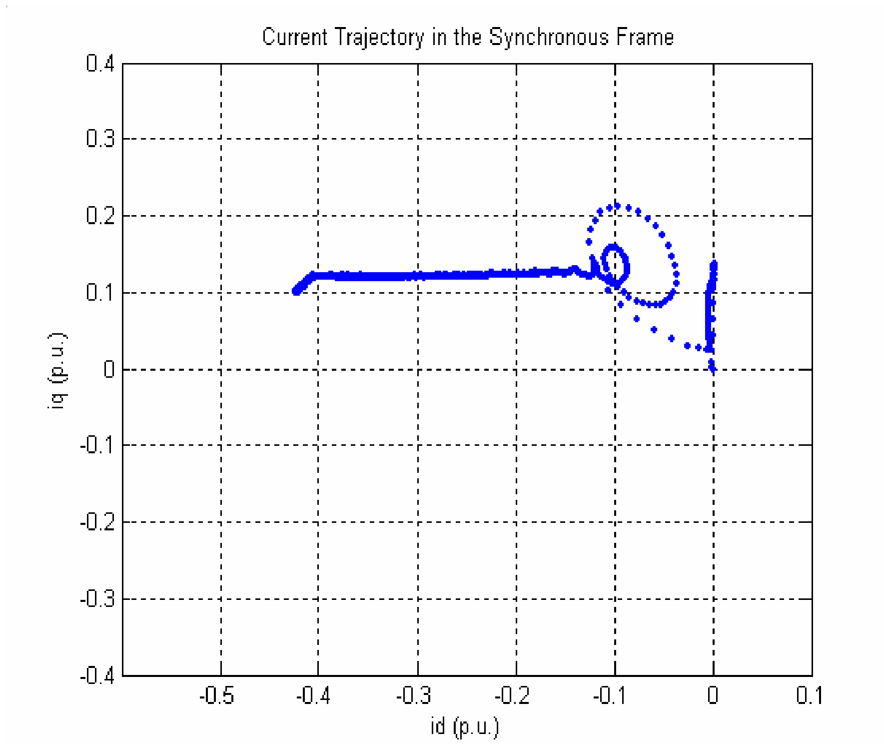

Figure 4.13: Simulated current trajectory of SPM during acceleration.

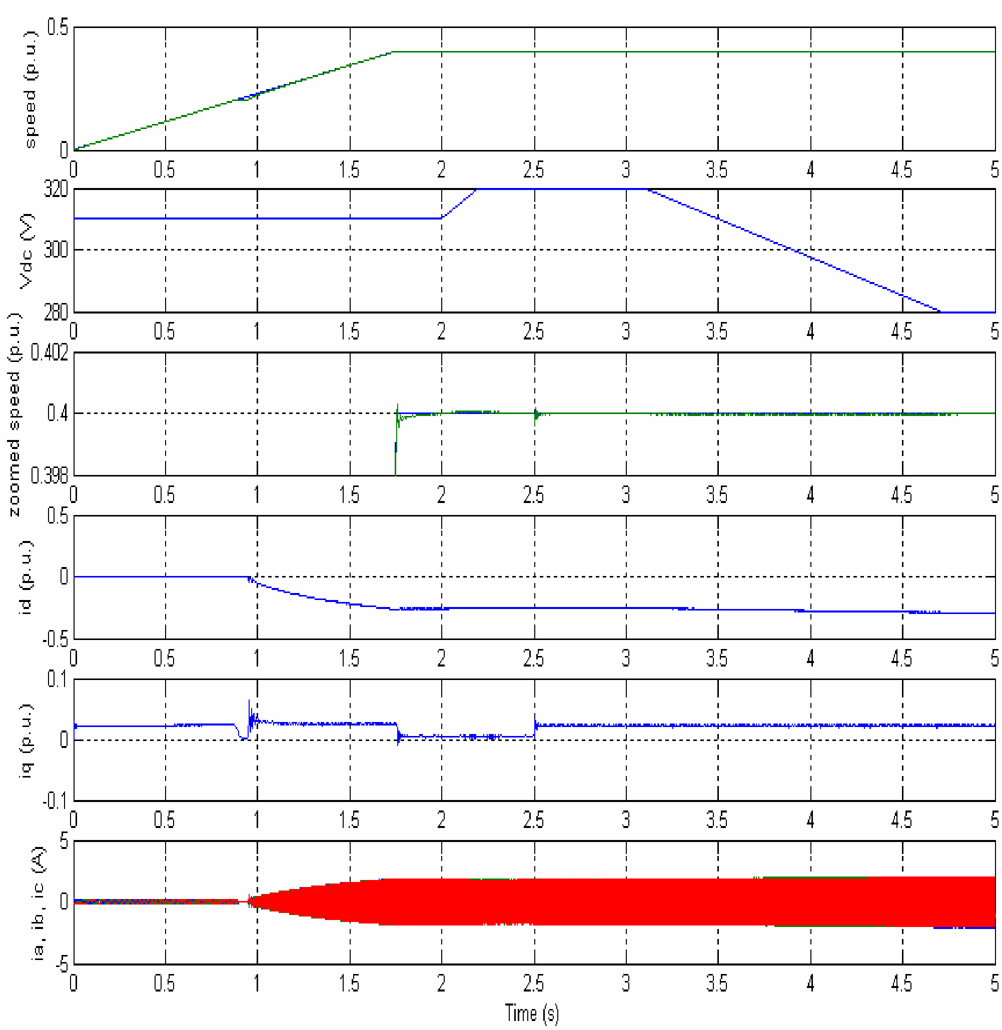

Figure 4.14: Simulation results of SPM drive system with disturbances of dc bus voltage and load: speed command ω^*_r and feedback ω_r (top), V_{dc} (2nd), zoomed speed command and feedback (3rd), i_{ds} (4th), i_{qs} (5th) and phase currents i_{as}, i_{bs}, i_{cs} (5.0 A/div, bottom).

4.8.2 Experimental results

Experimental tests have been extensively performed on a prototype PMSM drive system which consists of: 1) a three-phase IGBT power inverter with rated 310V dc bus voltage, which is a low-power universal power stage with interface peripherals manufactured by Spectrum Digital®; 2) a digital controller based on an eZdspF2812 board with Texas Instruments® TMS320F2812 DSP; 3) a dynamometer as load; and 4) a PM motor coupled with a dynamometer (please refer to Appendix B). Two different PM motors are used as control target respectively to verify the flux-weakening control concept and the related optimum design. One is a SPM motor and the other is an IPM motor. The machine parameters of the two motors are listed in Table 4.4. Note that the magnet materials of the two types of PMSM are different. The SPM uses ferrite while IPM takes advantage of Nd-Fe-B.

SPM	Value (Unit)	IPM	Value (Unit)
R_s	16.5 (Ω)	R_s	9.5 (Ω)
L_s	60 (mH)	L_d	50 (mH)
		L_q	65 (mH)
λ_m	0.2232 (Wb)	λ_m	0.3151 (Wb)
P	24 (pair)	P	24 (pair)

Table 4.4: Parameters of the tested SPM and IPM motor.

Using the fixed voltage constant $V_{FWC} = 0.5V_{smax}$, the experimental results of the two PM motors are shown in Figure 4.15 through Figure 4.27 except in Figure 4.22 and 4.23.

Figure 4.15 and Figure 4.16 show the experimental results when the SPM motor is accelerated from 50 to 1025 rpm and stays for 25 seconds and then decelerated to 50 rpm. The dc bus voltage varies between 320V and 280V due to fluctuation of input ac voltage to the power inverter and torque changes with the acceleration and deceleration. The load torque is 0.5 N.m constantly. We can observe the automatically generated demagnetizing current i_{ds} and the good performance of speed control within the wide speed range including flux-weakening region. Similarly the results of testing on the IPM motor are shown in Figure 4.17 through 4.20. By comparing the results of computer simulation in Figure 4.12 and 4.13 to the experimental ones in Figure 4.15 and 4.17, it is clearly seen that the experimental results agree to the large extent with the simulation results, indicating that the proposed flux-weakening control scheme is valid and the real-time implementation of the speed/flux-weakening controller is successful.

Moreover, the current and speed trajectories of IPM during acceleration are illustrated in Figure 4.21. It is interesting to find the relationship between the direct-axis current and the speed in real time in the i_{ds}-i_{qs} plane. Obviously the speed trajectory verifies the relationship shown in Figure 4.4.

Figure 4.22 shows the experimental results of efficiency-optimized SFWC when the SPM motor is running at 500 rpm with no load in (a), and 2 N.m in (b) referring to about 30% allowable maximum torque with respect to speed. It can be seen that the magnitude difference of phase currents, i.e., drops, after the efficiency-optimized algorithm is activated. Without load the r.m.s value of phase current is averagely 1.25 A before the optimized algorithm activated while 0.9 A thereafter. With 2 N.m, it is 1.36 A before while 0.98 A after. Similar tests have been done and results shown in Figure 4.23 when the motor speed is at 1,000 rpm in two cases: with no load and 1 N.m referring to 1/3 allowable maximum respectively. Without load the r.m.s value of phase current is 1.35 A before the optimized algorithm activated at 1,000 rpm while 1.08 A after. Furthermore, the phase current is measured 1.36 A before efficiency optimization while 1.12 A after when the motor is loaded. In both cases, the copper losses have been much reduced by applying the efficiency optimization and consequently the operation efficiency of the motor is improved by more than 10%.

The robustness of the SPM drive system with SFWC has been demonstrated through a series of tests at two different speeds, i.e., 500 and 1,000 rpm, with disturbances from dc bus voltage and/or load. The experimental results are shown in Figure 4.24 through 4.27 respectively.

In Figure 4.24, experimental results in five scenarios of disturbance from dc bus voltage V_{dc} are included: (a) V_{dc} varies from about 330 V down to 250 v and then up to 310 V; (b) V_{dc} changes from 310 V up to 330 V; (c) V_{dc} changes from 330 V down to 310 V; (d) V_{dc} changes from 310 V down to 250 V; and (e) V_{dc} changes from 250 V up to 310 V. It is clearly seen that the magnitude of phase currents varies with dc bus voltage adaptively, but the motor speed keeps regulated and unchanged at 500 rpm with the constant load of 1 N.m. Similar tests are repeated but at 1,000 rpm and the experimental results are shown in Figure 4.23. The load is added with the same torque as at 500 rpm. The consistency of experimental results in Figure 4.24 and 4.25 is obvious.

Figure 4.26 and 4.27 show the experimental results of SFWC with variations of load at 500 and 1,000 rpm respectively. Step load of 5 N.m is added and then removed at 500 rpm which relates to the 95% allowable maximum torque with respect to speed. At 1,000 rpm, similarly, step load from zero to 2 N.m to zero is applied. It shows that the speed is well regulated, especially at steady state regardless of load disturbances. In addition, the good dynamic performance of the drive system with SFWC is seen through the tests.

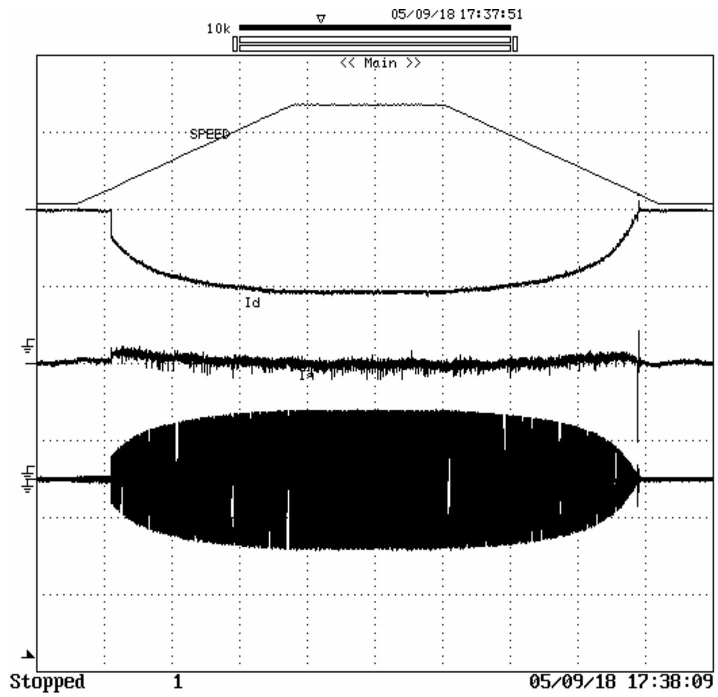

Figure 4.15: Experimental results of SPM during acceleration and deceleration with 0.5-N.m load: speed ω_r (757 rpm/div, top), i_{ds} (1.7 A/div, 2nd), i_{qs} (1.7 A/div, 3rd) and stator phase current i_{as} (2.0 A/div, bottom), 10 s/div.

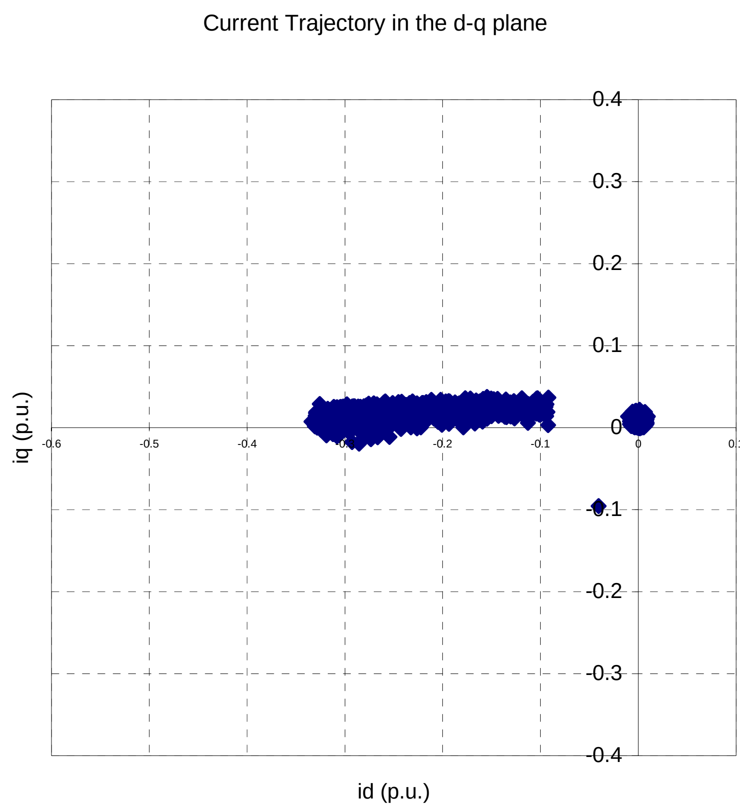

Figure 4.16: Current trajectory of SPM in the i_{ds}-i_{qs} plane during acceleration.

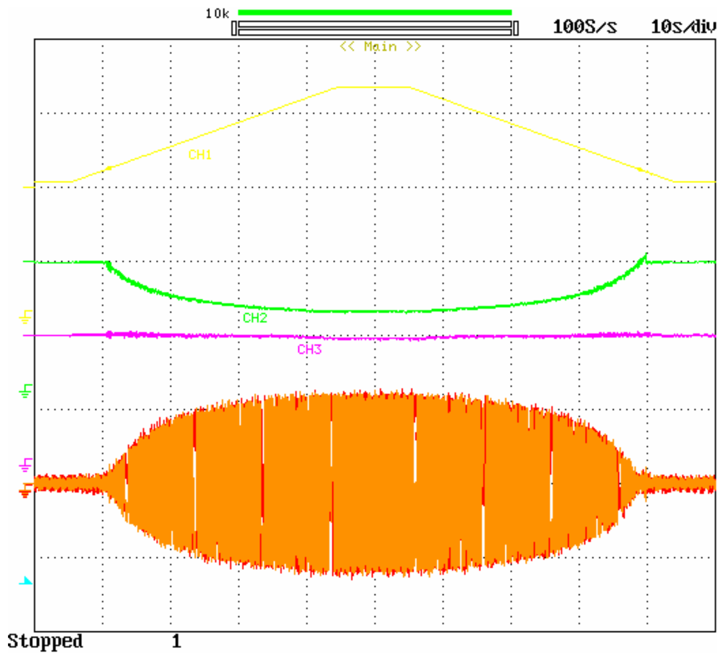

Figure 4.17: Experimental results of IPM during acceleration and deceleration with 0.5-N.m load: speed ω_r (757 rpm/div, top), i_{ds} (3.4 A/div, 2nd), i_{qs} (3.4 A/div, 3rd) and stator phase current i_{as}, i_{bs} (2.0 A/div, bottom), 10 s/div.

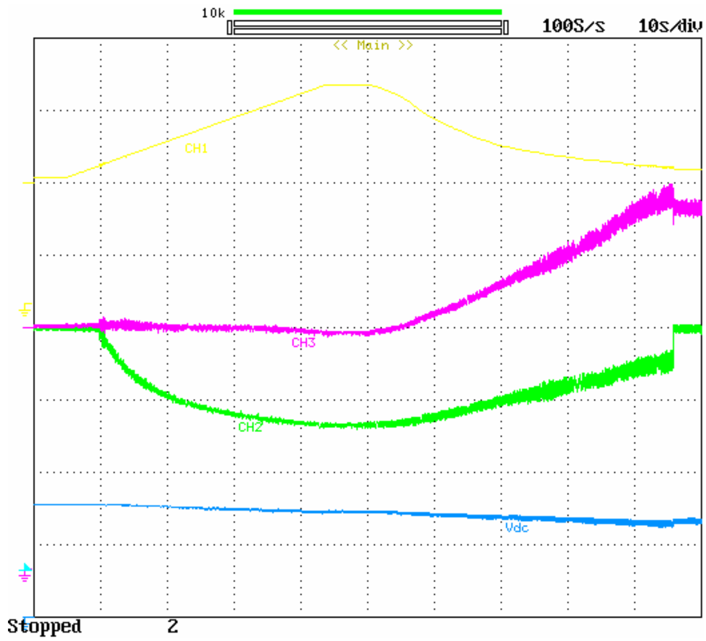

Figure 4.18: Experimental results of IPM during acceleration with 0.5-N.m load and deceleration with an increasing braking torque: speed ω_r (757 rpm/div, CH1), current i_{ds} (1.7 A/div, CH2), i_{qs} (1.7 A/div, CH3) and dc bus voltage V_{dc} (200 V/div, Vdc), 10 s/div.

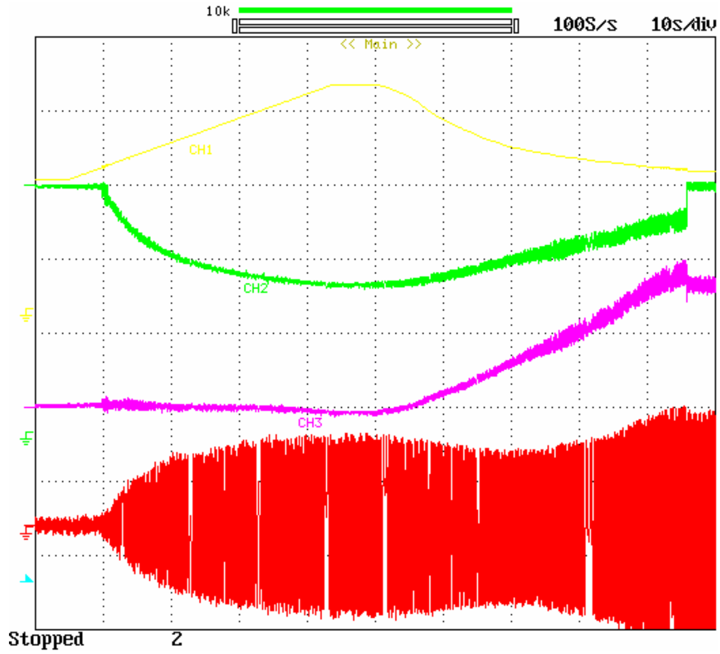

Figure 4.19: Experimental results of IPM during acceleration with 0.5-N.m load and deceleration with an increasing braking torque: speed ω_r (757 rpm/div, CH1), current i_{ds} (1.7 A/div, CH2), i_{qs} (1.7 A/div, CH3) and stator phase current i_{as} (2.0 A/div, bottom), 10 s/div.

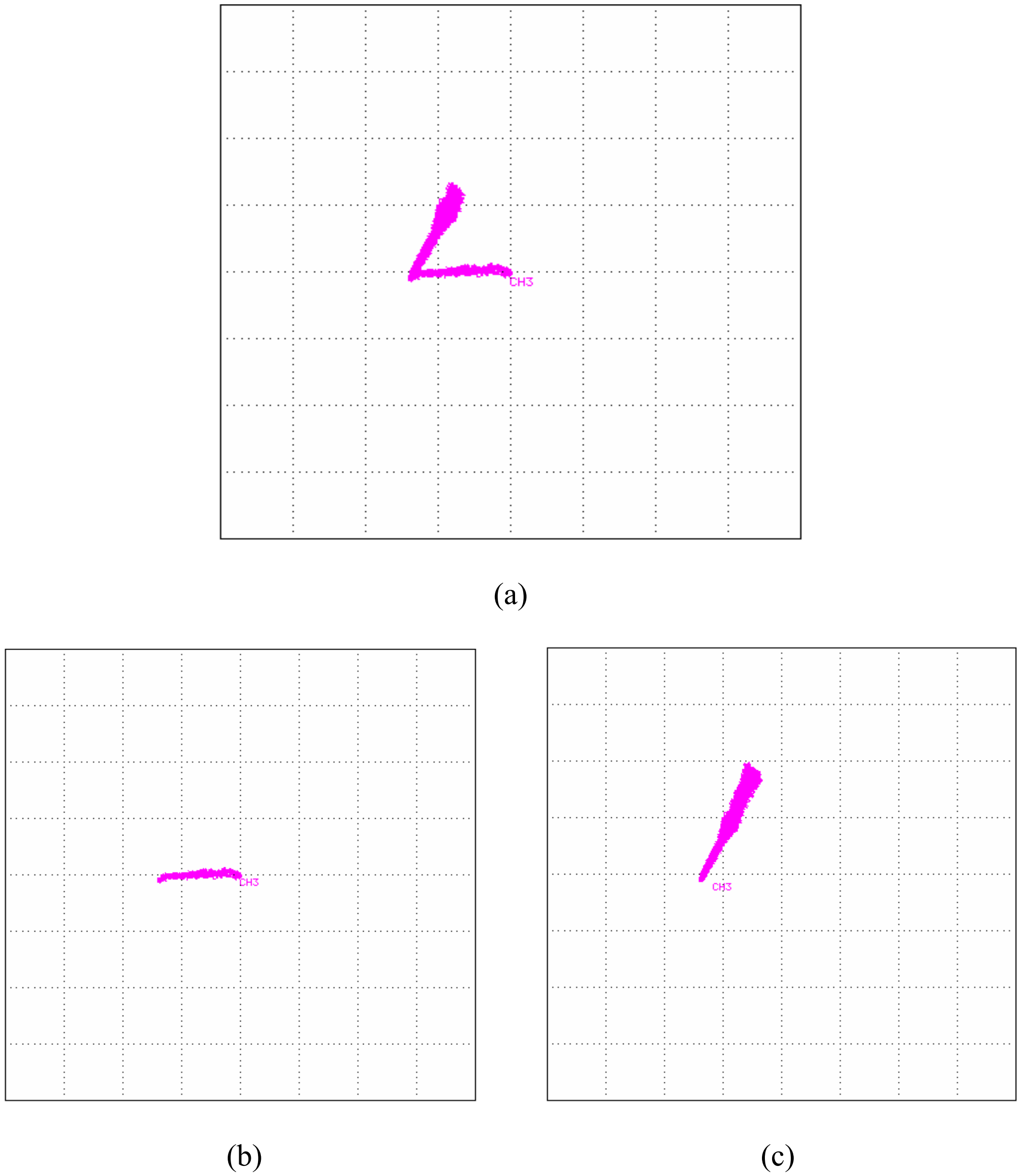

Figure 4.20: Current trajectory of IPM in the i_{ds}-i_{qs} plane during acceleration with 0.5-N.m load and deceleration with an increasing braking torque: (a) acceleration and deceleration; (b) acceleration; and (c) deceleration with an increasing braking torque, (1.7 A/div).

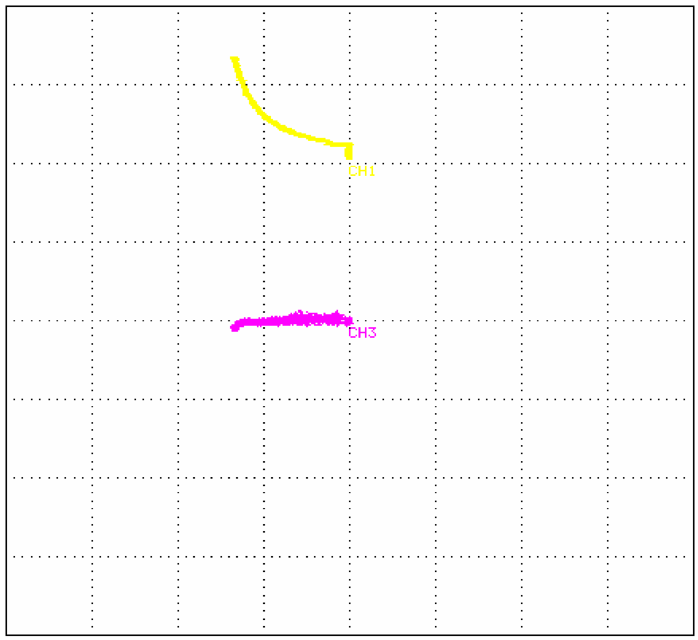

Figure 4.21: Current and speed trajectories of IPM during acceleration: speed ω_r (757 rpm/div, top), and current i_{qs} (1.7 A/div, bottom).

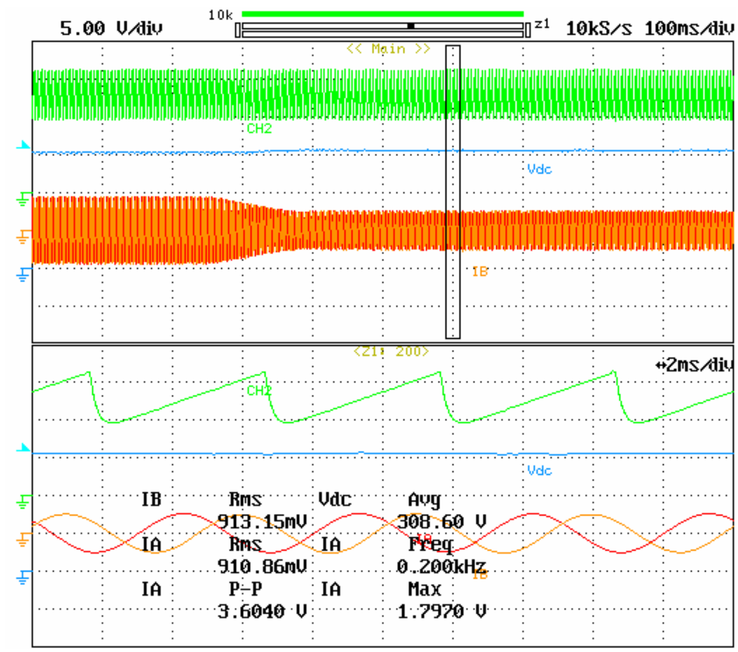

(a)

Figure 4.22: Experimental results of efficiency-optimized SFWC at 500 rpm: rotor position θ_r (top), V_{dc} (100 V/div, mid), and stator phase current i_{as}, i_{bs} (2.0 A/div, bottom): (a) without load, and (b) with load,100 ms/div.

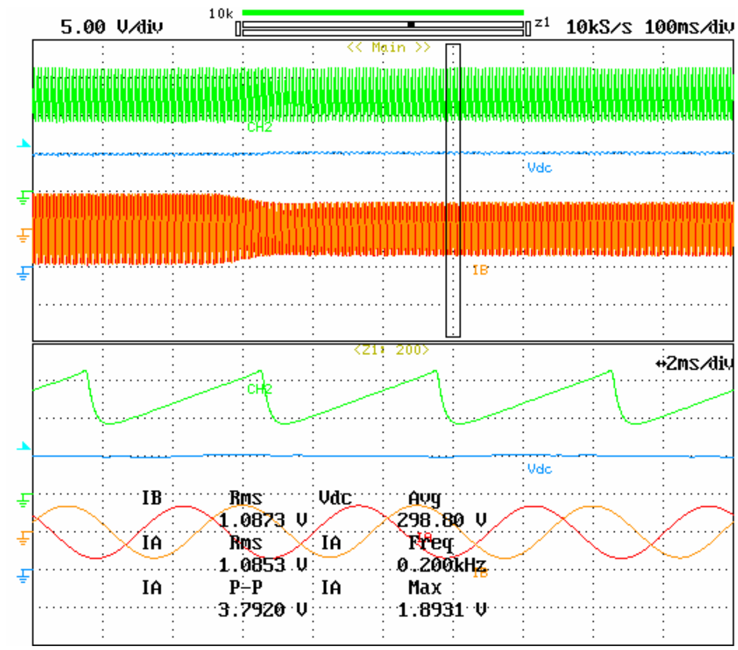

(b)

Figure 4.22: (continued) Experimental results of efficiency-optimized SFWC at 500 rpm: rotor position θ_r (top), V_{dc} (100 V/div, mid), and stator phase current i_{as}, i_{bs} (2.0 A/div, bottom): (a) without load, and (b) with load, 100 ms/div.

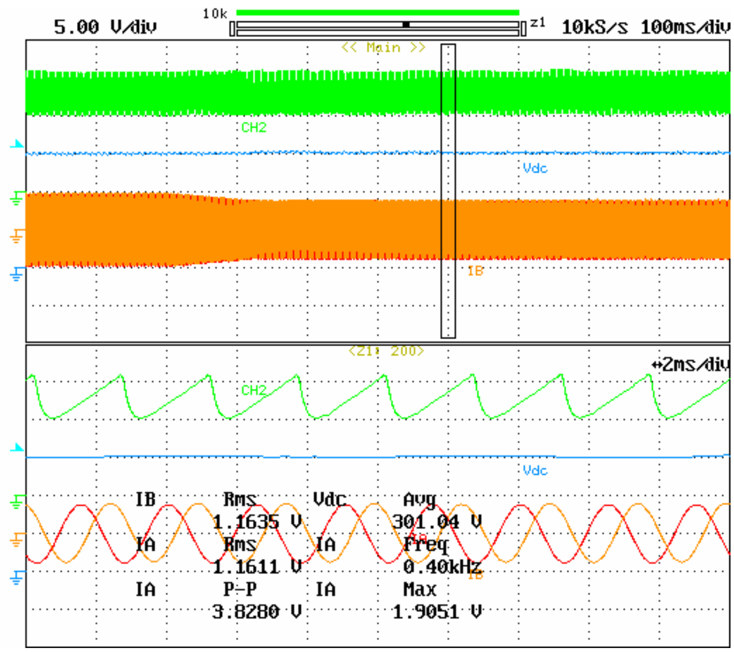

(a)

Figure 4.23: Experimental results of efficiency-optimized SFWC at 1,000 rpm: rotor position θ_r (top), V_{dc} (100 V/div, mid), and stator phase current i_{as}, i_{bs} (2.0 A/div, bottom); (a) without load, and (b) with load, 100 ms/div.

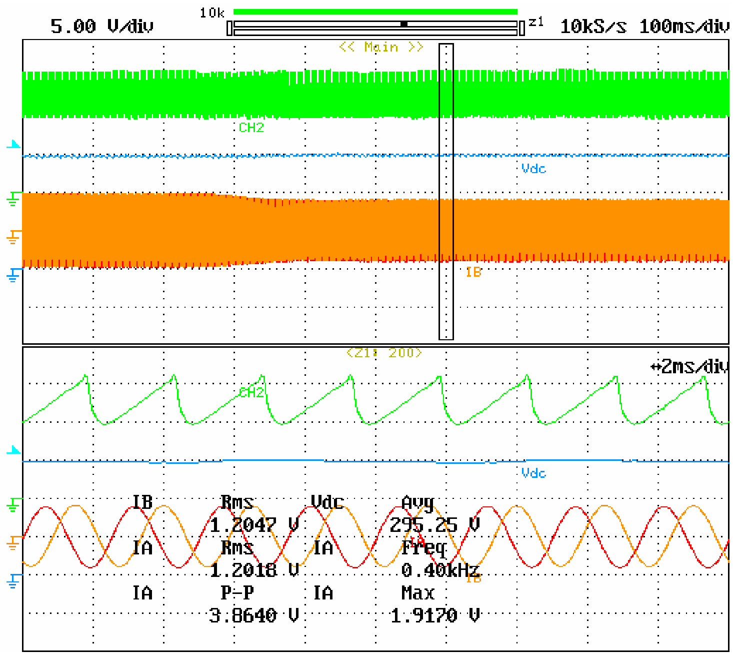

(b)

Figure 4.23: (continued) Experimental results of efficiency-optimized SFWC at 1,000 rpm: rotor position θ_r (top), V_{dc} (100 V/div, mid), and stator phase current i_{as}, i_{bs} (2.0 A/div, bottom); (a) without load, and (b) with load, 100 ms/div.

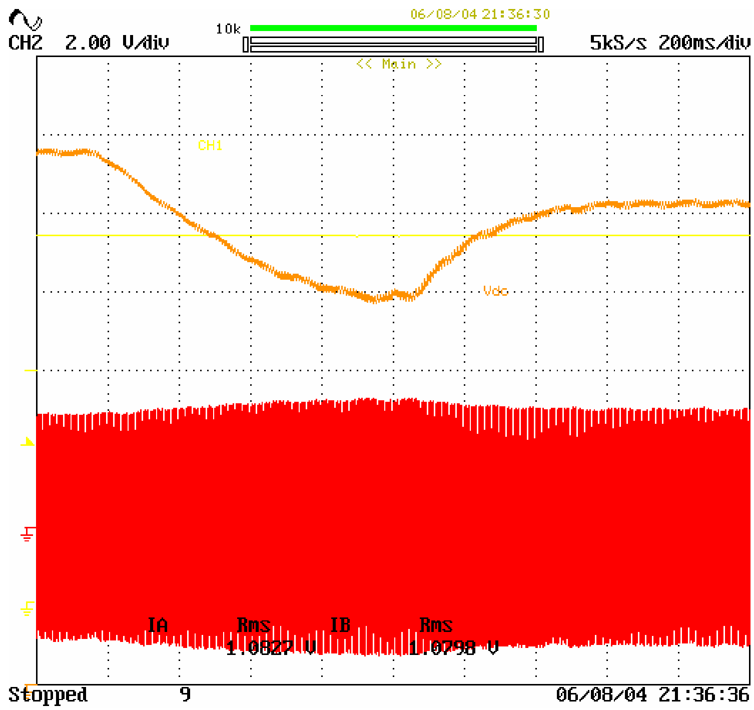

(a)

Figure 4.24: Experimental results of SFWC with variation of dc bus voltage at 500 rpm: speed ω_r (189 rpm/div, CH1), V_{dc} (50 V/div, Vdc), and phase current i_{as}, i_{bs} (1.0 A/div, bottom), 200 ms/div.

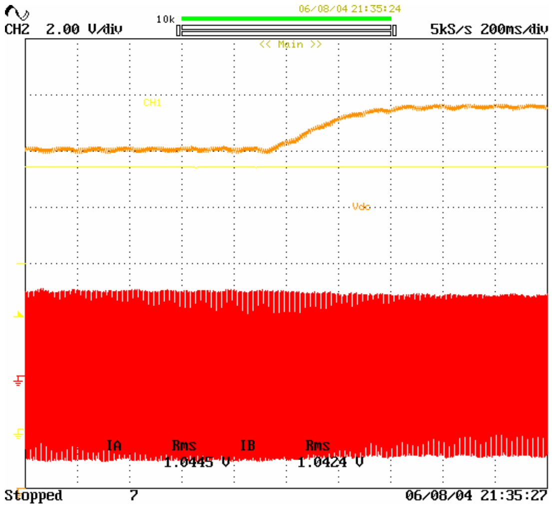

(b)

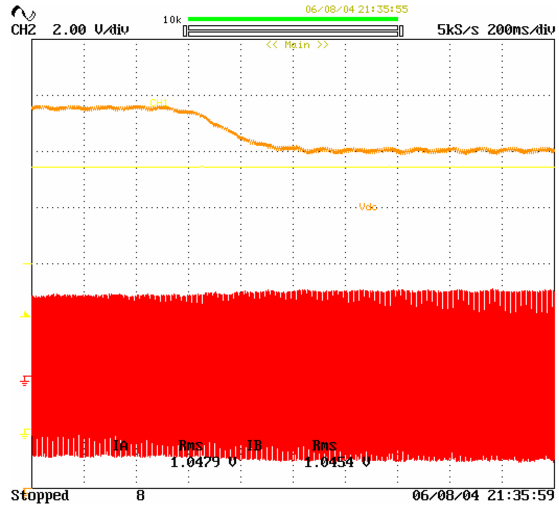

(c)

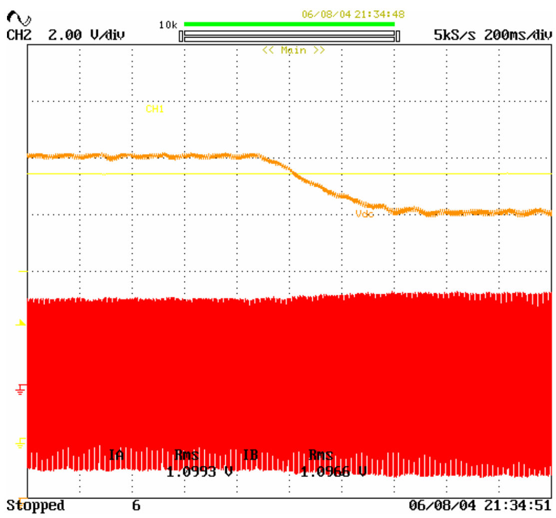

(d)

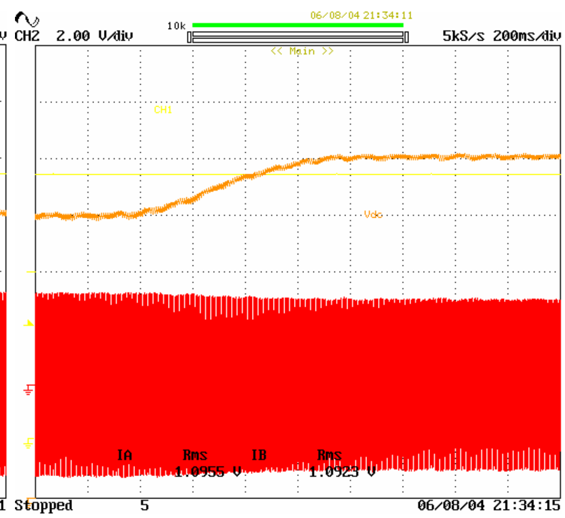

(e)

Figure 4.24: (continued) Experimental results of SFWC with variation of dc bus voltage at 500 rpm: speed ω_r (189 rpm/div, CH1), V_{dc} (50 V/div, Vdc), and phase current i_{as}, i_{bs} (1.0 A/div, bottom), 200 ms/div.

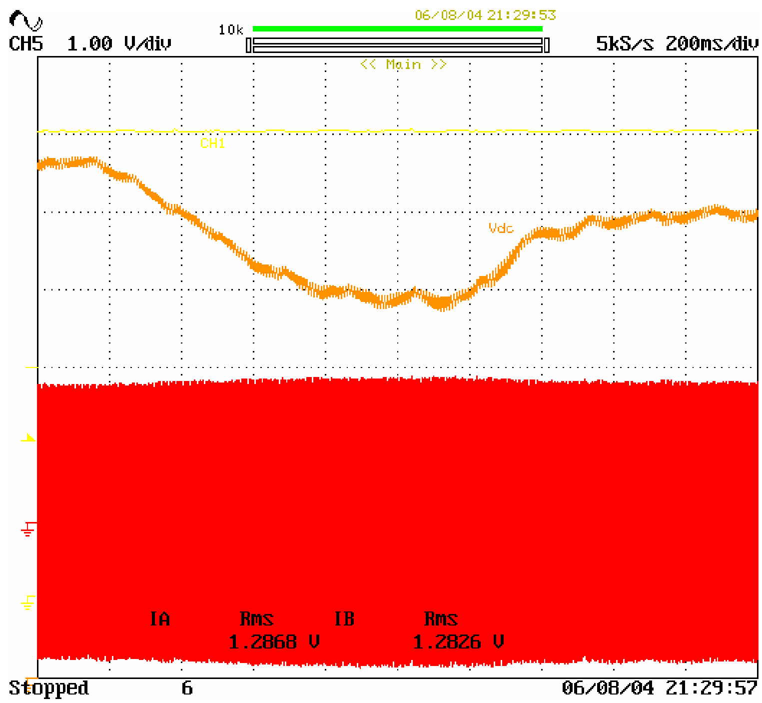

(a)

Figure 4.25: Experimental results of SFWC with variation of dc bus voltage at 1,000 rpm: speed ω_r (189 rpm/div, CH1), V_{dc} (50 V/div, Vdc), and phase current i_{as}, i_{bs} (1.0 A/div, bottom), 200 ms/div.

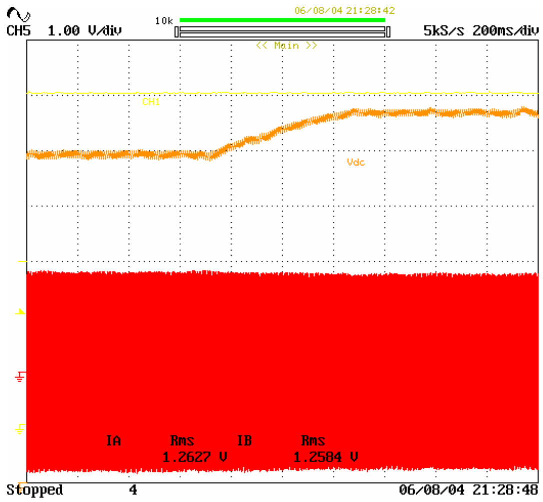

(b)

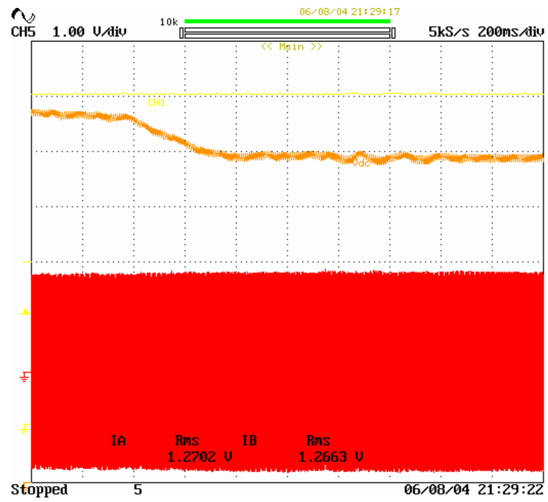

(c)

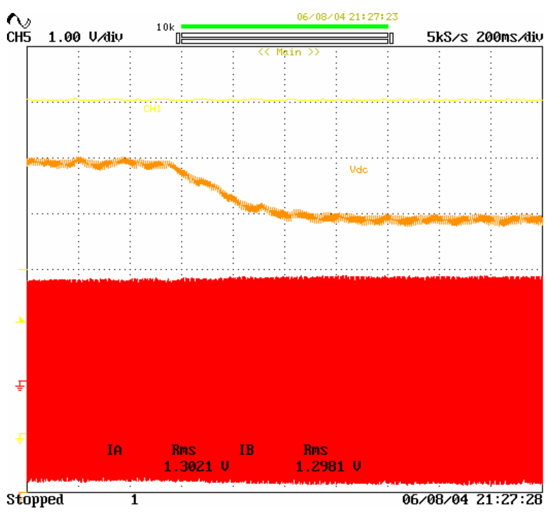

(d)

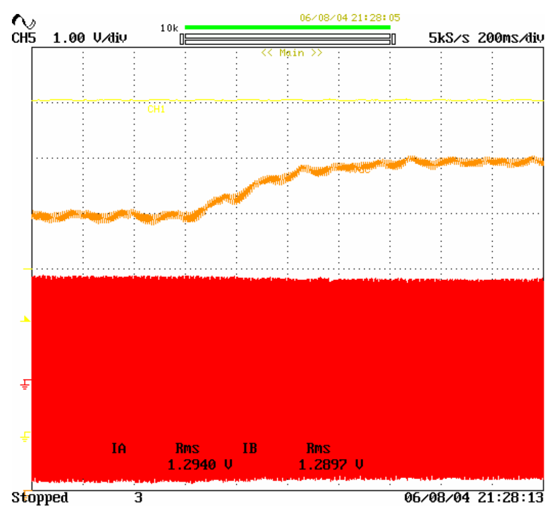

(e)

Figure 4.25: (continued) Experimental results of SFWC with variation of dc bus voltage at 1,000 rpm: speed ω_r (189 rpm/div, CH1), V_{dc} (50 V/div, Vdc), and phase current i_{as}, i_{bs} (1.0 A/div, bottom), 200 ms/div.

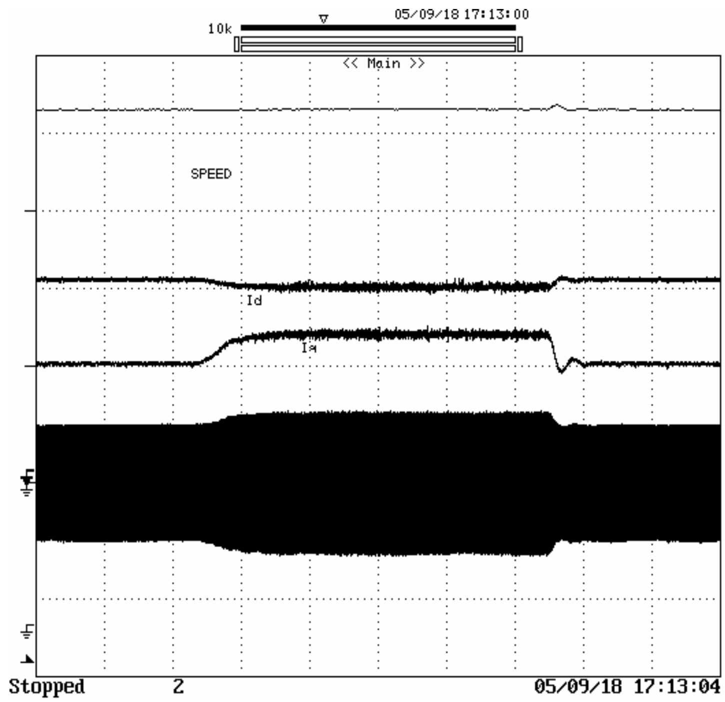

Figure 4.26: Experimental results of SFWC with variation of load at 500 rpm: speed ω_r (378 rpm/div, top), i_{ds} (1.7 A/div, 2nd), i_{qs} (1.7 A/div, 3rd) and stator phase current i_{as}, i_{bs} (2.0 A/div, bottom), 200 ms/div.

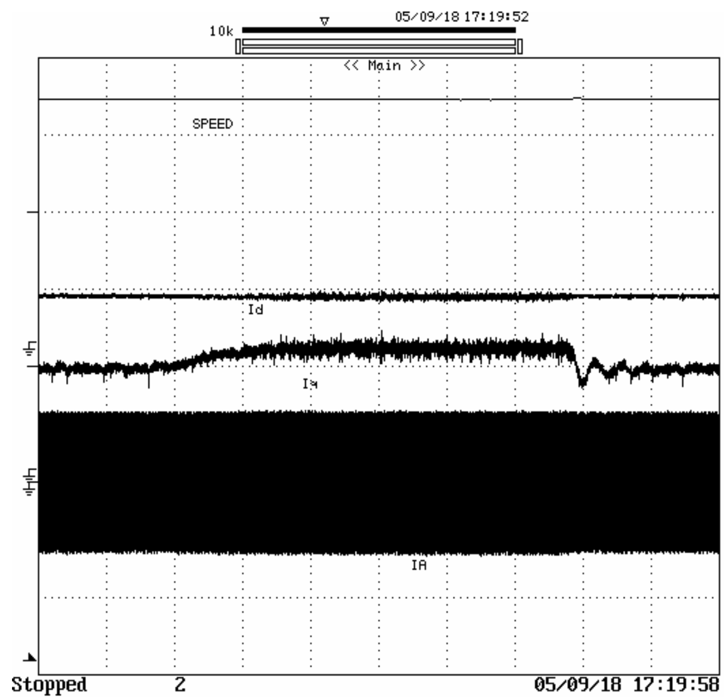

Figure 4.27: Experimental results of SFWC with variation of load at 1,000 rpm: speed ω_r (757 rpm/div, top), i_{ds} (1.7 A/div, 2nd), i_{qs} (1.7 A/div, 3rd) and stator phase current i_{as}, i_{bs} (2.0 A/div, bottom), 200 ms/div.

4.9 Summary

In this chapter, a robust flux-weakening control scheme has been studied, which incorporates the speed regulation of the PMSM drive system. It utilizes none of accurate machine models but the cross-coupling effects inherent to PMSM, and thus it is robust and insensitive to the variation of machine parameters and operating conditions. This flux-weakening control scheme is adaptive in the sense of automatic generation of the desired demagnetizing current considering both current and voltage constraints over full speed range.

In contrast to employing the conventional two-loop current regulation, the PMSM drive with the developed speed/flux-weakening controller is able to achieve both flux-weakening and speed control simultaneously, as well as preventing from saturation of current regulators in the flux-weakening region. This feature will bring the advantage of reduced computation/execution time to cost-effective drive systems

Graphic method is introduced and used throughout this chapter. The aim of this intuitive method is twofold: to analyze the flux-weakening operation of PMSM and design its control; and to further optimize the design, which are all based on the current trajectories.

Finally, an efficiency-optimized design is conducted and its effectiveness demonstrated by experimental results.

CHAPTER 5

SLIDING MODE OBSERVER FOR POSITION-SENSORLESS CONTROL OVER WIDE SPEED RANGE

This chapter will present a sliding mode technique for position-sensorless control of PMSM over wide speed range. Such technique provides an alternative to the observation of rotor position adaptive to operating speed of PMSM. The design of sliding mode observer (SMO) is based on the machine model derived in Chapter 3. A concept of feedback of equivalent control is highlighted and the selection of feedback gain discussed for the speed adaptation. Existence condition of sliding mode and proof of its stability will be given using Lyapunov method.

5.1 Theoretical Background for Sliding Mode

In this chapter, we will exclusively deal processes with affine control systems which can be described by nonlinear differential equations in an arbitrary *n*-dimensional state space with *m*-dimensional control: [1]

$$\dot{x} = f(x,t) + B(x,t)u + h(x,t) \tag{5.1}$$

where $x \in \Re^n$ is state vector, $u \in \Re^m$ is control vector, and $h(x,t) \in \Re^n$ represents all the disturbances to the system. The symbol t denotes the time.

Assuming that all the disturbances act in the control space, $h(x,t) \in \Re^n$ satisfies the following condition for each state x and t,

$$h(x,t) \in span\ \{B(x,t)\} \tag{5.2}$$

Thus, there exists a control u such that $Bu=-h(x,t)$ and hence the system is invariant to the disturbance $h(x,t)$.

The control can be selected as a discontinuous function of the state in the form of

$$u_i = \begin{cases} u_i^+(x,t) & if\ s_i(x) > 0 \\ u_i^-(x,t) & if\ s_i(x) < 0 \end{cases} \quad (i = 1,2,...m)$$

$$s^T(x) = (s_1(x), s_2(x), ..., s_m(x)) \tag{5.3}$$

where $u_i^+(x,t)$ and $u_i^-(x,t)$ are continuous state functions with $u_i^+(x,t) \neq u_i^-(x,t)$ while the control u_i may undergo discontinuities on the surface $s_i(x)=0$ in the state space; the $s_i(x)$ is also continuous state function. $s(x)>0$(or $s(x)<0$) means that each component $s_i(x)>0$(or $s_i(x)<0$), $i=1,2,...,m$.

By enforcing sliding mode in systems with discontinuous control, sliding mode occurs eventually in the intersection of m surfaces $s_i(x)=0$ ($i=1,2,...,m$) and the order of the motion equations is m that may be less than the order of original system. This order reduction leads to decoupling and simplification of control design procedure.

Furthermore, the control component u_i has the input $s(x)$ decay to zero during sliding mode whereas its output takes finite values with precise average superimposed by high-frequency components. This implies high gain is implemented to suppress the influence of disturbances and uncertainties in the plant behavior. The invariance effect is in turn attained using finite control actions, which is different in continuous high-gain control systems. It should be noticed that sliding mode is independent of the disturbances $h\,(x,t)$ For the design of an invariance system, there is no need to measure $h\,(x,t)$. But an upper bound of $h\,(x,t)$ is needed for the guarantee of sliding mode.

The motion projection of (5.1) on the s-space can be expressed by

$$\dot{s} = G(f + h) + GBu \tag{5.4}$$

where $G = {\partial s}/{\partial x}$ assuming $det\,(GB) \neq 0$ for all state x and time t.

Let $\dot{s} = 0$, the so-called equivalent control u_{eq} can be calculated as

$$u_{eq} = -(GB)^{-1} G(f + h) \tag{5.5}$$

Substitution of (5.5) into system (5.1) yields the sliding mode motion equation in the manifold $s\,(x) = 0$ as

$$\dot{x} = f - B(GB)^{-1} Gf \tag{5.6}$$

Note that the control action is implemented through (5.3) instead of (5.5). Equation (5.6) is used for analysis of system behavior during sliding mode. By introducing a boundary layer $x\,(t,\Delta)$ (width Δ>0) of the manifold $s\,(x) = 0$, for the affine systems (5.1), the sliding mode equation is found uniquely in the framework and it coincides with (5.6) resulting from the equivalent control method. It is concluded that any solution in the boundary layer tends to a solution $x^*(t)$ to equation (5.6) regardless of what kind of imperfection has caused the motion in the boundary layer and how the boundary layer is reduced to zero.

The motion in sliding mode is a sort of certain idealization. It is assumed that the discontinuous control changes at high, theoretically infinite, frequency such that the state velocity vector is oriented precisely along the intersection of discontinuity surfaces. However, in reality, various imperfections (including hysteresis, time delay and small time constants neglected in the ideal model) make the state oscillate in some vicinity of the intersection, i.e., boundary layer, and the control components are switched at finite frequency, alternatively taking the values $u_i^+(x,t)$ and $u_i^-(x,t)$. The motion in sliding mode is actually determined by the low-frequency component of the oscillations while its high-frequency component is filtered out by a plant under control. Physically understanding, the equivalent control is close to the slow part of the real control which may be derived by filtering out the high-frequency component using a low-pass filter (LPF). The extracted information can be used for designing state observers with sliding modes, improvement of feedback control system performance and chattering suppression.

On the above discussion, when the state $x(t)$ reaches the manifold and then enforced on it by the discontinuous control, we say, the sliding mode occur and then the system features the order reduction and invariance properties. The sliding mode dynamics depend on the switching surface equation and not on the control. Hence the design procedure can be decoupled into two stages: first, select equation of sliding mode, i.e., equation (5.6), to design the dynamics of the motion in accordance with performance criterion; second, find the discontinuous control such that the state would reach the manifold $s(x) = 0$ and sliding mode exists in this manifold.

Previous studies show that sliding mode observers have attractive advantages of robustness to disturbances and low sensitivity to parameter variations when sliding mode truly happens. In principle, sliding mode approaches can only be achieved by discontinuous control and switching at infinite frequency. In reality, however, no such sliding mode will take place in implementation due to the limited switching frequency and current sampling rate. As a result, the discretization chattering problem normally exists. The boundary solution has been used to solve the chattering problem by replacing the discontinuous control with a saturation function which approximates the sign function in a boundary layer of sliding mode manifold. In such a way, the invariance property of sliding mode is partially preserved in the sense that the state trajectories are confined to a small vicinity of the manifold. However, the state behavior and further convergence to zero cannot be guaranteed.

For SMO-based sensorless control of PMSM, two challenges have to be dealt with properly: first, the very small magnitude of the back-EMF at low speeds; and second, the sufficient high switching gain satisfying the necessary conditions for the SMO convergence in the high-speed range. It is known that the minimum operating speed and the quality of the estimated rotor position at low speeds depend on the quantization error of discrete-time controller. On the other hand, the high switching gain may cause large ripples, i.e., oscillation, in the high-speed range, resulting in large estimation error.

5.2 Sliding Mode Observer

The sliding mode observer for estimating rotor position angle is based on a stator current estimator using discontinuous control. Due to the fact that only stator currents are directly measurable in a PMSM drive, the sliding mode manifold $s(x) = 0$ is selected on the real stator current trajectory. In this way, when the estimated currents, i.e., state, reach the manifold and then the sliding mode happens and has been enforced, the current estimation error becomes zero and the estimated currents track the real ones regardless of certain disturbances and uncertainties of the drive system.

Considering the machine model in the stationary reference frame, referring to the equations (3.31) and (3.32) as in Chapter 2, (repeated here for convenience)

$$\dot{\vec{i}}_{\alpha\beta s} = -L_{\alpha\beta s}{}^{-1} r_{\alpha\beta s} \cdot \vec{i}_{\alpha\beta s} + L_{\alpha\beta s}{}^{-1}(\vec{v}_{\alpha\beta s} - \vec{e}_{\alpha\beta s}) \tag{3.31}$$

and its matrix form

$$\begin{bmatrix} \dot{i}_{\alpha s} \\ \dot{i}_{\beta s} \end{bmatrix} = \begin{bmatrix} -R_s/L_s & 0 \\ 0 & -R_s/L_s \end{bmatrix} \begin{bmatrix} i_{\alpha s} \\ i_{\beta s} \end{bmatrix} + \begin{bmatrix} 1/L_s & 0 \\ 0 & 1/L_s \end{bmatrix} \left(\begin{bmatrix} v_{\alpha s} \\ v_{\beta s} \end{bmatrix} - \begin{bmatrix} e_{\alpha s} \\ e_{\beta s} \end{bmatrix} \right) \tag{3.32}$$

the sliding mode current estimator is designed with the same structure as PM machines without saliency:

$$\dot{\hat{\vec{i}}}_s = -L_{\alpha\beta s}{}^{-1} r_{\alpha\beta s} \cdot \hat{\vec{i}}_s + L_{\alpha\beta s}{}^{-1}(\vec{v}^*{}_s + l \cdot \vec{Z}_{eq} + \vec{Z}) \tag{5.7}$$

or

$$\dot{\hat{\vec{i}}}_s = A \cdot \hat{\vec{i}}_s + B(\vec{v}^*{}_s + l \cdot \vec{Z}_{eq} + \vec{Z})$$

where

$$A = \begin{bmatrix} -R_s/L_s & 0 \\ 0 & -R_s/L_s \end{bmatrix} \qquad B = \begin{bmatrix} 1/L_s & 0 \\ 0 & 1/L_s \end{bmatrix} \qquad K = \begin{bmatrix} k & 0 \\ 0 & k \end{bmatrix}$$

$$\vec{i}_s = \vec{i}_{\alpha\beta s} = \begin{bmatrix} i_{\alpha s} \\ i_{\beta s} \end{bmatrix} \qquad \vec{v}^*{}_s = \begin{bmatrix} v^*{}_{\alpha s} \\ v^*{}_{\beta s} \end{bmatrix} \qquad \hat{\vec{i}}_s = \begin{bmatrix} \hat{i}_{\alpha s} \\ \hat{i}_{\beta s} \end{bmatrix}$$

$$\vec{Z} = \begin{bmatrix} z_{\alpha s} \\ z_{\beta s} \end{bmatrix} = -K \cdot sign(\hat{\vec{i}}_s - \vec{i}_s) = -k \begin{bmatrix} sign(\hat{i}_{\alpha s} - i_{\alpha s}) \\ sign(\hat{i}_{\beta s} - i_{\beta s}) \end{bmatrix}$$

And, the matrix form of (5.7) is

$$\begin{bmatrix} \dot{\hat{i}}_{\alpha s} \\ \dot{\hat{i}}_{\beta s} \end{bmatrix} = \begin{bmatrix} -R_s/L_s & 0 \\ 0 & -R_s/L_s \end{bmatrix} \begin{bmatrix} \hat{i}_{\alpha s} \\ \hat{i}_{\beta s} \end{bmatrix} + \begin{bmatrix} 1/L_s & 0 \\ 0 & 1/L_s \end{bmatrix} \left(\begin{bmatrix} v^*_{\alpha s} \\ v^*_{\beta s} \end{bmatrix} + l \cdot \begin{bmatrix} z_{eq\alpha} \\ z_{eq\beta} \end{bmatrix} + \begin{bmatrix} z_{\alpha s} \\ z_{\beta s} \end{bmatrix} \right) \tag{5.8}$$

In the above equations, l is the feedback gain of the equivalent control vector $\vec{Z}_{eq}$; and k, normally positive ($k > 0$), is the switching gain of the discontinuous control $\vec{Z}$. The superscript '*' denotes a command variable. The hat '^' indicates the estimated variables. The equivalent control $\vec{Z}_{eq}$ can be obtained by using a low-pass filter in the form of

$$\vec{Z}_{eq} = \begin{bmatrix} Z_{eq\alpha} \\ Z_{eq\beta} \end{bmatrix} = \begin{bmatrix} -k \cdot sign(\hat{i}_{\alpha s} - i_{\alpha s}) \cdot \dfrac{\omega_c}{s + \omega_c} \\ -k \cdot sign(\hat{i}_{\beta s} - i_{\beta s}) \cdot \dfrac{\omega_c}{s + \omega_c} \end{bmatrix} \quad \omega_c : \; freq\_cutoff \tag{5.9}$$

The time constant of the LPF must be sufficiently small to preserve the slow component, i.e., the equivalent control, undistorted but large enough to eliminate the high-frequency component. On demand, the vicinity of the sliding mode manifold of width Δ, where the state oscillates, should be reduced to make the real motion close to ideal sliding mode. For reduction of Δ, the switching frequency of the control should be increased or the switching gain reduced, otherwise the state would oscillate out of the boundary layer. Thus, the time constant of the LPF should be designed properly to extract the slow component equal to the equivalent control and to filter out the high-frequency component.

Therefore, the cutoff frequency ω_c of the LPF should be designed properly according to the fundamental frequency of the tracked stator currents.

By subtracting equation (3.31) from (5.7) with the assumption of $\vec{v}_{\alpha\beta s} = \vec{v}^*{}_s$, we can obtain the dynamic sliding mode motion equation as expressed in

$$\dot{S} = A \cdot S + B \cdot (\vec{e}_{\alpha\beta s} + l \cdot \vec{Z}_{eq} + \vec{Z}) \tag{5.10}$$

where the current error vector $S = \vec{\hat{i}}_s - \vec{i}_s$.

If the switching gain of $\vec{Z}$, i.e., k, is large enough to guarantee

$$\dot{S}^T \cdot S < 0 \tag{5.11}$$

then, sliding mode occurs and we get

$$\vec{e}_{\alpha\beta s} = \begin{bmatrix} e_{\alpha s} \\ e_{\beta s} \end{bmatrix} = -(1+l)\vec{Z}_{eq} \tag{5.12}$$

Furthermore, the rotor position angle $\hat{\theta}_r$ can be estimated from (5.12) as

$$\hat{\theta}_r = -\tan^{-1}(\frac{e_{\alpha s}}{e_{\beta s}}) = -\tan^{-1}(\frac{Z_{eq\alpha}}{Z_{eq\beta}}) \tag{5.13}$$

To solve the chattering problem in a digitalized control system with finite switching frequency, the sign function for the discontinuous control is replaced by a saturation function as shown in Figure 5.1. When the amplitude of current error is less than E_0, i.e., width of the boundary layer, the discontinuous control $\vec{Z}$ changes to a saturation function as

$$\vec{Z} = -k_s \cdot (\vec{\hat{i}}_s - \vec{i}_s) \tag{5.14}$$

where $k_s = k / E_0$.

Finally, a block diagram of the proposed sliding mode observer is shown in Figure 5.2.

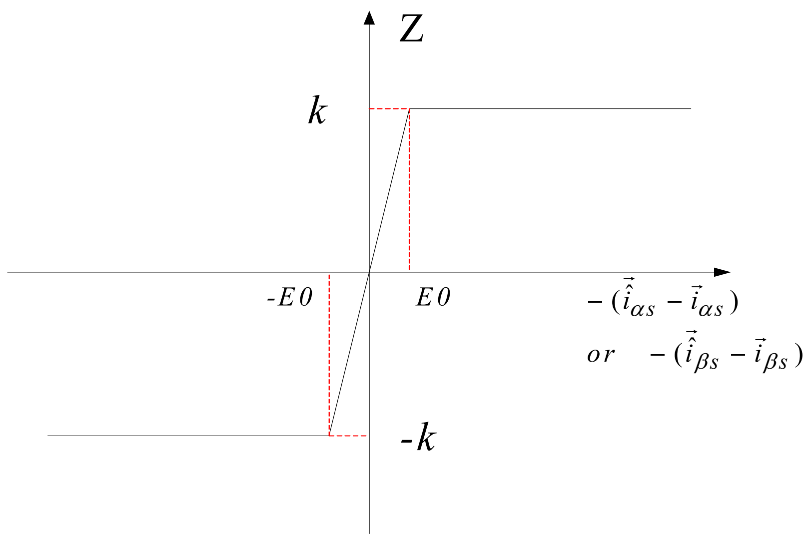

Figure 5.1: Diagram of saturation function.

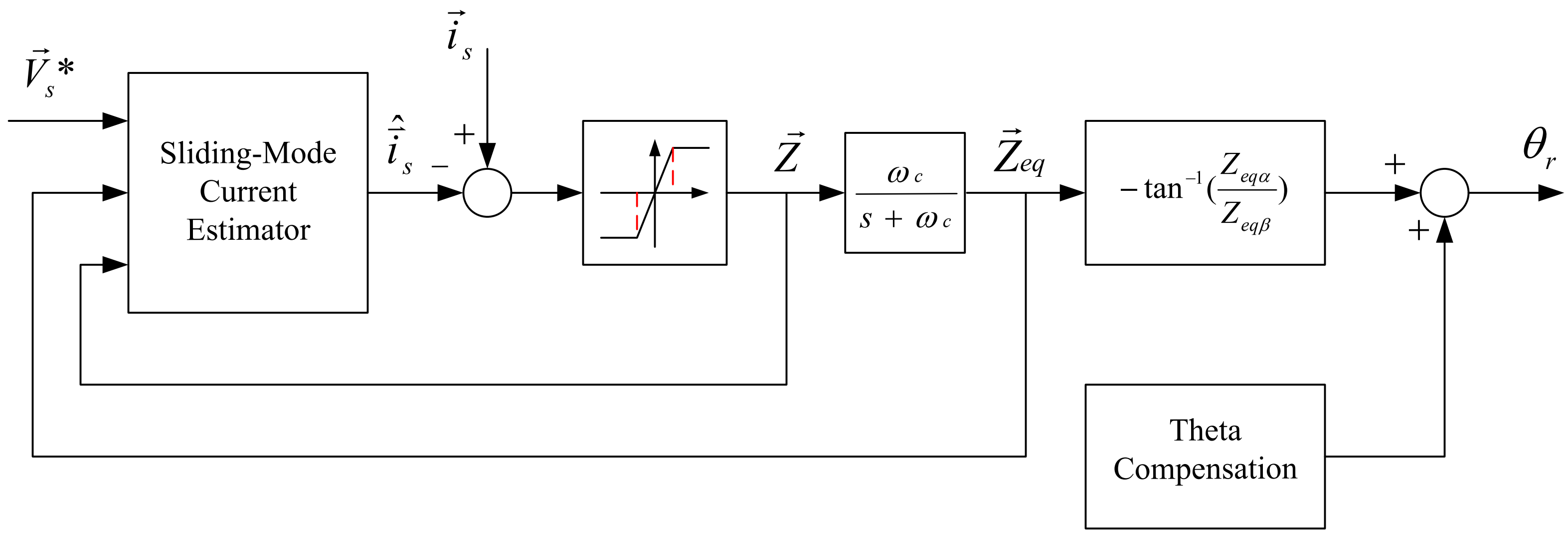

Figure 5.2: Block diagram of the proposed sliding mode observer.

5.3 Stability Analysis

Let the positive definite function

$$V = \frac{1}{2} \cdot S^T \cdot S > 0 \tag{5.15}$$

be a Lyapunov function candidate. Its time derivative along the system trajectories is of the form

$$\dot{V} = S^T \cdot \dot{S} = S^T AS + S^T B \cdot (\vec{e}_{\alpha\beta s} + l \cdot \vec{Z}_{eq} + \vec{Z}) \tag{5.16}$$

Considering (5.9) and the time constant of LPF, $\mu = 1/\omega_c$, we get

$$\begin{aligned} \dot{V} &= S^T \cdot \dot{S} \\ &\Rightarrow S^T AS + S^T B \cdot \vec{e}_{\alpha\beta s} - k(\frac{l}{\mu s + 1} + 1) S^T B \cdot sign(S) = F1 + F2 \end{aligned} \tag{5.17}$$

where

$$F1 = S^T AS$$

$$\begin{aligned} F2 &= 1 \cdot \!/\! L_s \left\{ \begin{aligned} &\bar{i}_{\alpha s}\left[e_{\alpha s} - k \cdot \frac{\mu s + 1 + l}{\mu s + 1} sign(\bar{i}_{\alpha s}) \right] \\ &+ \bar{i}_{\beta s}\left[e_{\beta s} - k \cdot \frac{\mu s + 1 + l}{\mu s + 1} sign(\bar{i}_{\beta s}) \right] \end{aligned} \right\} \\ &= 1 \cdot \!/\! L_s \left\{ \begin{aligned} &\bar{i}_{\alpha s} \cdot \left[e_{\alpha s} \mp k \cdot \frac{\mu s + 1 + l}{\mu s + 1} \right] \left(\begin{matrix} \bar{i}_{\alpha s} > 0 \\ \bar{i}_{\alpha s} < 0 \end{matrix} \right) \\ &+ \bar{i}_{\beta s} \cdot \left[e_{\beta s} \mp k \cdot \frac{\mu s + 1 + l}{\mu s + 1} \right] \left(\begin{matrix} \bar{i}_{\beta s} > 0 \\ \bar{i}_{\beta s} < 0 \end{matrix} \right) \end{aligned} \right\} \end{aligned}$$

From the equation (5.7), we know that the matrix A is negative definite and B positive definite. Consequently *F1* is negative.

Assuming μ is very small, i.e., $\mu << 1$, with regard to the high cutoff frequency ω_c of LPF, the part *F2* will be negative definite if the following satisfies.

$$\begin{cases} k \cdot \dfrac{\mu s + 1 + l}{\mu s + 1} > \left| e_{\alpha s} \right| \\ k \cdot \dfrac{\mu s + 1 + l}{\mu s + 1} > \left| e_{\beta s} \right| \end{cases} \Rightarrow k \cdot (1 + l) > \left| \vec{e}_{\alpha\beta s} \right|_{\max} \tag{5.18}$$

The above constraint equation forms the necessary existence condition of the sliding mode observer. That means the product of the switching gain *k* and (1+*l*) must be larger than the maximum peak value of the back-EMK should sliding mode occur. This provides one criteria for the selection of switching gain of the discontinuous control and the feedback gain of the equivalent control.

It also implies that the feedback gain *l* must be larger than –1 with any positive switching gain *k*, i.e., $l > -1$, which is the limit of the feedback gain of the equivalent control.

Therefore, the time derivative of Lyaponov function *V* is negative with enough large positive switching gain *k* satisfying (5.18), which testifies to convergence to $S(t) = 0$ within finite time and thereby the existence of sliding mode.

In the boundary layer, the discontinuous control $\vec{Z}$ is replaced by the saturation function which approximates the *sign*(*s*) term in a E_0-vicinity of the sliding mode manifold $S(t)$=0. Considering the problem 'in the large', i.e., for $|S(t)| > E_0$, we have

$sat(\mathrm{S}) = sign(\mathrm{S})$. However, in a small E_0-vicinity of the origin, the so-called boundary layer, $sat(\mathrm{S}) \neq sign(\mathrm{S})$ is continuous.

Then, substitute (5.14) into (5.10) instead of the sign function to yield

$$\dot{S} = \left[A - (l+1) \cdot k_s \cdot B\right] \cdot S + B \cdot \vec{e}_{\alpha\beta s} \tag{5.19}$$

Direct examination of the above shows the system trajectories are firstly guaranteed to converge to the boundary layer. Because the system is continuous and linear within the boundary layer, the eigenvalue placement for the linear system can be implemented to accelerate the convergence rate of SMO at high speeds and guarantee further convergence to zero. Hence, the invariance property of sliding mode control is partially preserved in the sense that the system trajectories are confined to a vicinity of the sliding manifold $S(t)$=0, instead of exactly to $S(t)$=0 as in ideal sliding mode. Within the vicinity, the system behavior of further convergence to zero can also be guaranteed.

5.4 Selection of Feedback Gain of Equivalent Control

As aforementioned, the feedback gain l of equivalent control $\vec{Z}_{eq}$ plays important role on the existence condition of sliding mode and further convergence rate in the boundary layer of the manifold $S(t)$=0. It is thus expected that through selecting the feedback gain l can the flexibility of selecting the switching gain k result and the improvement of tracking performance of stator currents and thereafter of the estimation quality of rotor position.

Next, the discussion will be focused on two proposals of selecting the feedback gain l with respect to rotor speed.

Proposal A:

- Below the base speed: **0 > *l* > -1**

From (5.12), we can see that the magnitude of the equivalent control $\vec{Z}_{eq}$ is always larger than that of the back-EMF when the gain l is in the range of $0 > l > -1$. The rotor position of PMSM is calculated from $\vec{Z}_{eq}$. Although the back-EMF is small at low speeds, $\vec{Z}_{eq}$ is enlarged instead by selecting the feedback of equivalent control in this case. The rotor position angle is calculated by using the equivalent control. Therefore, with same quantization limit in a digitalized control system, the proposed sliding mode observer is able to work at lower speeds, or equivalently to extend the minimum operating speed.

- Above the base speed, i.e., flux-weakening region: ***l* > 0**

The eigenvalues of the coefficient matrix of S in (5.19) can be calculated by solving the equation

$$\det\{\ [A-(l+1)\cdot k_s\cdot B]-\lambda I\ \}=0 \tag{5.20}$$

where I is the identity matrix. Then we get

$$\lambda_{1,2}=-\frac{R_s+{(1+l)k}/{E_0}}{L_s}$$

It can be seen that the eigenvalues of $A-(l+1)\cdot k_s \cdot B$ become smaller and smaller with the feedback gain l increasing, i.e., move away from the imaginary axis in the s-plane, resulting in faster convergence rate of $S(t)$ to zero. This characteristic is critical to the high-speed operation of any observer-based control system.

On the other hand, the switching gain k can be designed with smaller value than those in conventional sliding mode observers, satisfying the same existence condition of sliding mode as defined by (5.18). By this approach, using same low-pass filter without changing its cutoff frequency, the ripples, i.e., high-frequency component, superimposed on the equivalent control $\vec{Z}_{eq}$ can be reduced, and as a result the estimated rotor position angle are smoother.

Proposal B:

The existence condition by (5.18) can be rewritten as

$$k \cdot (1+l) > |\omega_r| \lambda_m \tag{5.21}$$

If the feedback gain l is selected as the function of the rotor speed ω_r, i.e.,

$$l = |\omega_r| - 1 \tag{5.22}$$

the switching gain k has to satisfy the following to guarantee the sliding mode happen.

$$k > \lambda_m \tag{5.23}$$

Consequently the equivalent control $\vec{Z}_{eq}$ can be deducted from (5.12)

$$\vec{Z}_{eq} = -\lambda_m \begin{bmatrix} -\sin(\theta_r) \\ \cos(\theta_r) \end{bmatrix} \tag{5.24}$$

It is interesting to find that the equivalent control $\vec{Z}_{eq}$ has the constant magnitude, unlike the back-EMF of which the magnitude varies with the rotor speed and may change greatly when the rotor speed range is large, e.g., the speed ratio is 5:1 or higher. Moreover, the magnitude of $\vec{Z}_{eq}$ is the same as that of the rotor flux linkage λ_m. Therefore, two advantages will come with this method:

1) At low speeds when the back-EMF is too small to be estimated or sensed, the equivalent control still works for the estimation of rotor position due to its constant magnitude independent of speed. Thus the sliding mode observer is a sort of rotor flux observer. Therefore, this feedback method is expected to work at lower speeds than other conventional back-EMF-based observers. In reality, the minimum operating speed will also depend on the precision of speed and quantization error, which might not be zero.

2) It is easier to design the switching gain k in the real implementation. The consistence of estimation performance is guaranteed due to the constant magnitude of the equivalent control over wide speed range. The chattering problem normally at low speeds due to the high switching gain in conventional sliding observers does not exist.

In addition, the magnitude of the equivalent control may be directly used for the indication of the temperature of rotor because the rotor flux is subject to change with temperature according to the characteristics of magnet materials. However, it is cancelled in the calculation of the rotor position angle as in (5.13).

5.5 SMO-Based Sensorless Control of PMSM

Figure 5.3 shows a block diagram of the overall SMO-based sensorless PMSM drive system, which consists of a speed PI regulator, a flux-weakening controller, two current PI regulators in the synchronous reference frame, a speed calculator implemented by a Phase-Locked Loop (PLL) and a rotor position estimator by the sliding mode observer. In addition, conventional modules for vector control such as Clark, Park and inverse Park transformation, space vector PWM generation module, and a three-phase power inverter are included as well as the controlled PMSM. When the speed of the PMSM is very close to but still lower than its base speed, the flux-weakening controller will be activated, which automatically generates the required demagnetizing current command for the flux-weakening operation. Note that the control structure can be modified with the speed/flux-weakening controller as proposed in Chapter 4, which achieves speed regulation in the flux-weakening region, using only two PI-regulators as shown in Figure 4.3.

Near standstill, the back-EMF of the PMSM is too small to be estimated accurately. Therefore, an open-loop starting algorithm with a ramp speed command profile is designed to kick off the motor from standstill and accelerate it up to a specific speed, i.e., 25 rpm, at which the proposed sliding mode observer is activated. A relatively smooth start can be achieved by this method and considered adequate for startup without fast acceleration.

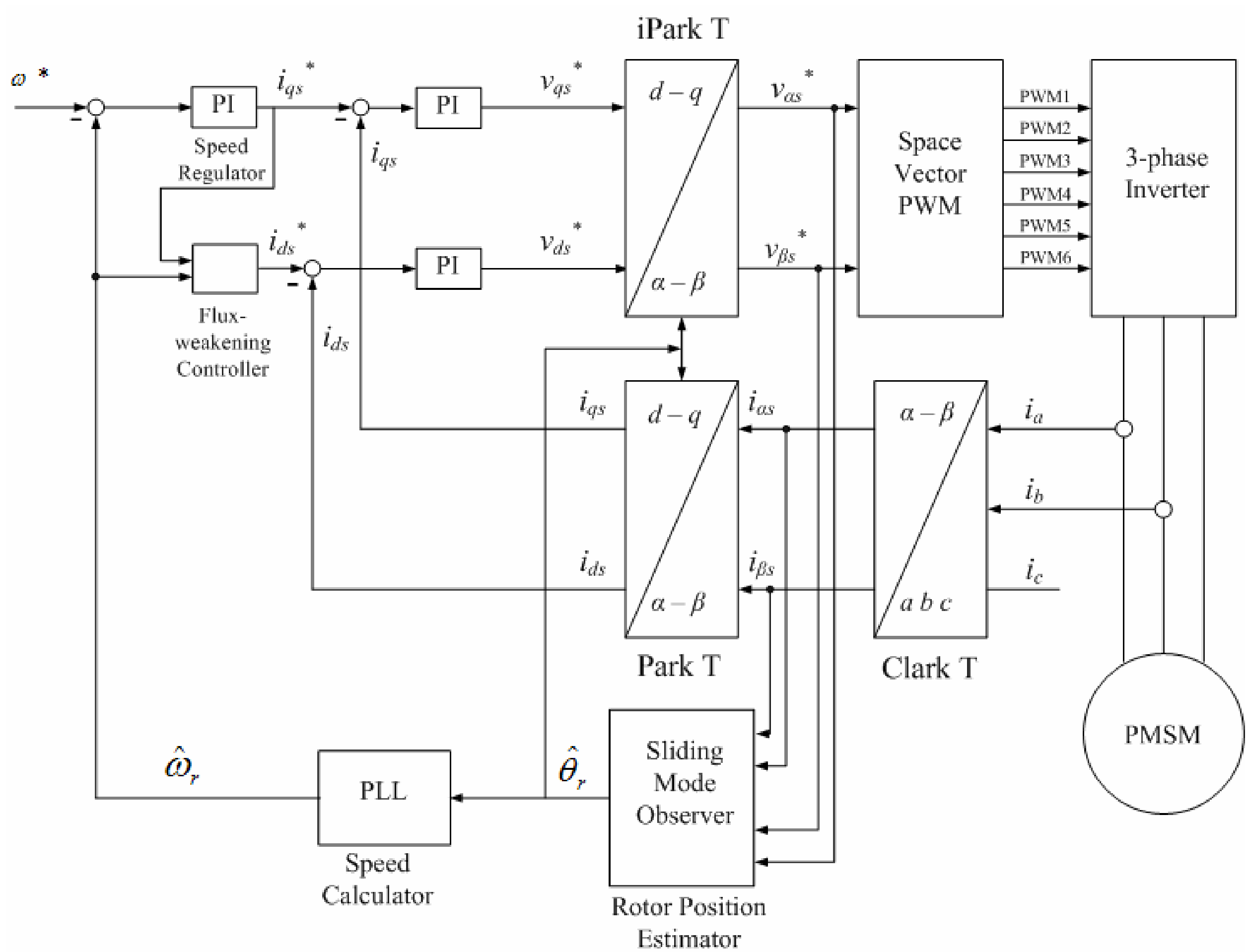

Figure 5.3: Block diagram of the overall SMO-based sensorless PMSM drive system.

5.6 Simulation and Experimental Results

5.6.1 Simulation results

Computer simulations have been performed to verify the estimation performance of the sliding mode observer and to examine the related sensorless control of PMSM drive system. Same as in Chapter 4, Matlab/Simulink® with SimPowerSystems Blockset is used as simulation platform. A Simulink model of PMSM drive system including the sliding mode observer is also shown in Appendix A. The parameters of the tested SPM motor and drive system are same as in Table 4.2. The dc bus voltage of the power inverter is 310 V. The space vector PWM generation module is employed and its execution updated every 50 μs with respect to the output PWM switching frequency of 20 kHz. Variables in the speed and current regulators are represented in per unit. The speed base is chosen to be 1,250 rpm and current base 7 A. The switching gain k of the sliding mode observer is 800. The cutoff frequency of the low-pass filter for obtaining the equivalent control is 4,000 π.rad/s while the maximum fundamental frequency of phase currents is 1,000 π.rad/s. The simulation parameters of Simulink are as same as in Table 4.3.

Figure 5.4 shows the simulation results when the motor is running at 50 rpm with the feedback gain l = -0.5 in (a) and at 1,000 rpm with l = 1 in (b). In the two cases, the waveforms of actual and estimated variables such as rotor position angle and stator current i_{as} almost overlap together with very small errors (much smaller than 0.01). In the figure, 0.01 of angle error represents 0.57 electrical degree. In addition, the control Z_a , i.e., Z_{as}, has been sampled in real time at a minimum frequency of 1 GHz while all other signals are sampled at fixed 100 kHz. Note that, in both figures (a) and (b), Z_a is plotted in sample dots but not aligned with other signals in time.

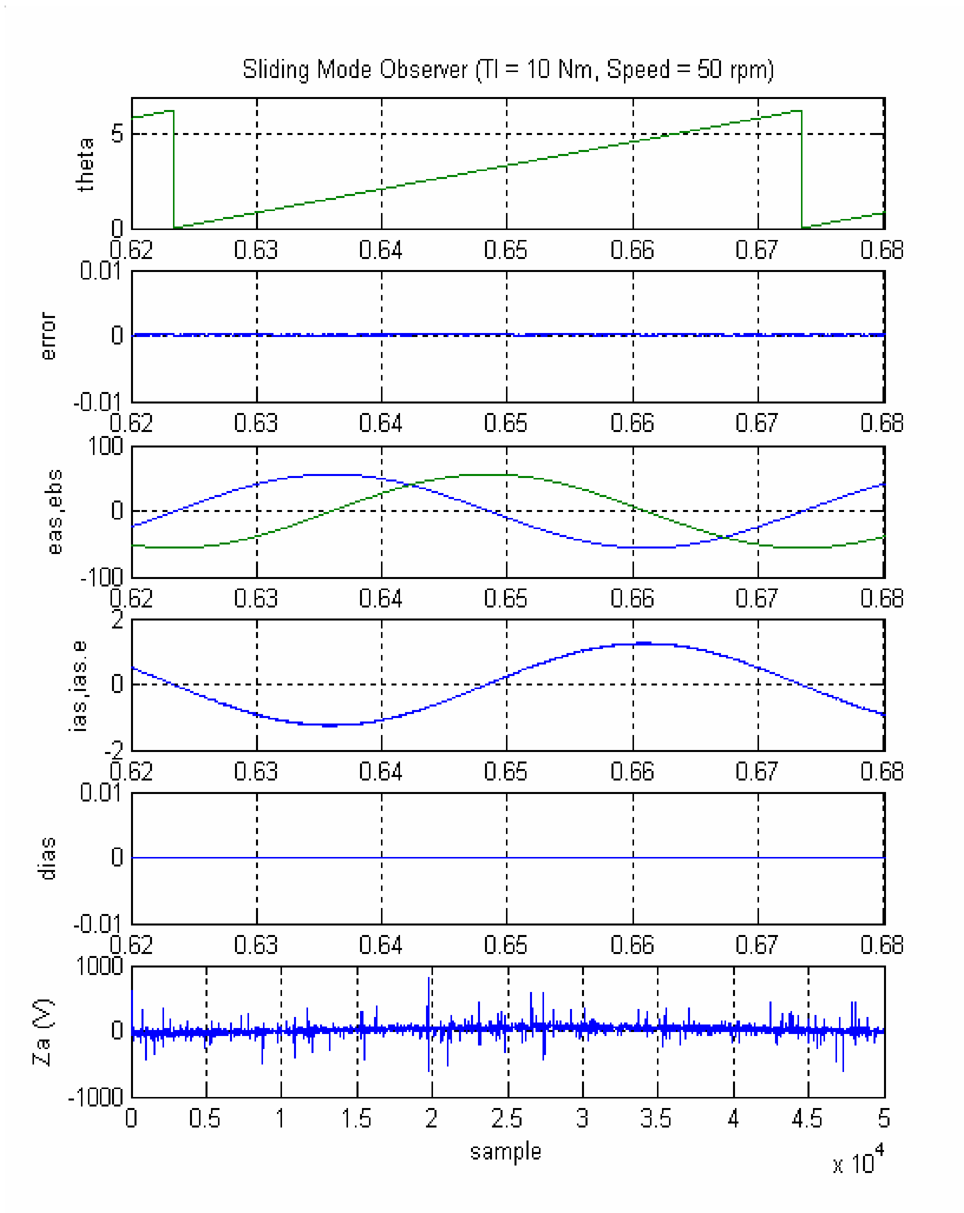

(a)

Figure 5.4: Simulation results of SMO.

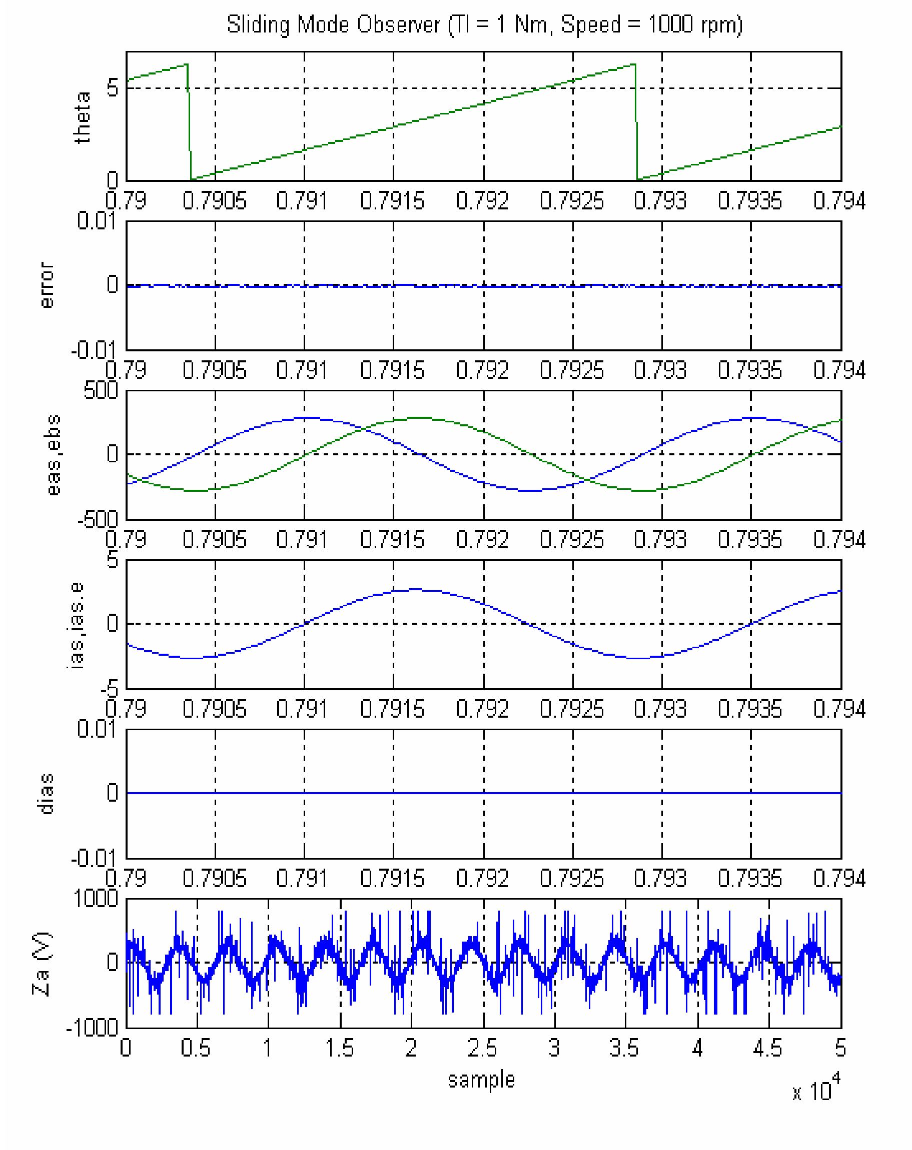

(b)

Figure 5.4: (continued) Simulation results of SMO: actual and estimated angle (top); estimation error (2nd); estimated back-EMF (3rd); measured and estimated current i_{as} (4th) and error (5th), and sliding mode control Z_a (bottom); (a) l=-0.5 at 50 rpm, (b) l=1 at 1,000 rpm.

Simulation results of SMO with adaptive feedback gain are shown in Figure 5.5. The motor is accelerated from 0 to 250 rpm constantly. We can observe that the estimated rotor position angle tracks the real one very well. And the magnitude of the equivalent control Z_{eq} is constant, with the same value as the rotor flux linkage. The feedback gain l increases with the rotor speed accordingly.

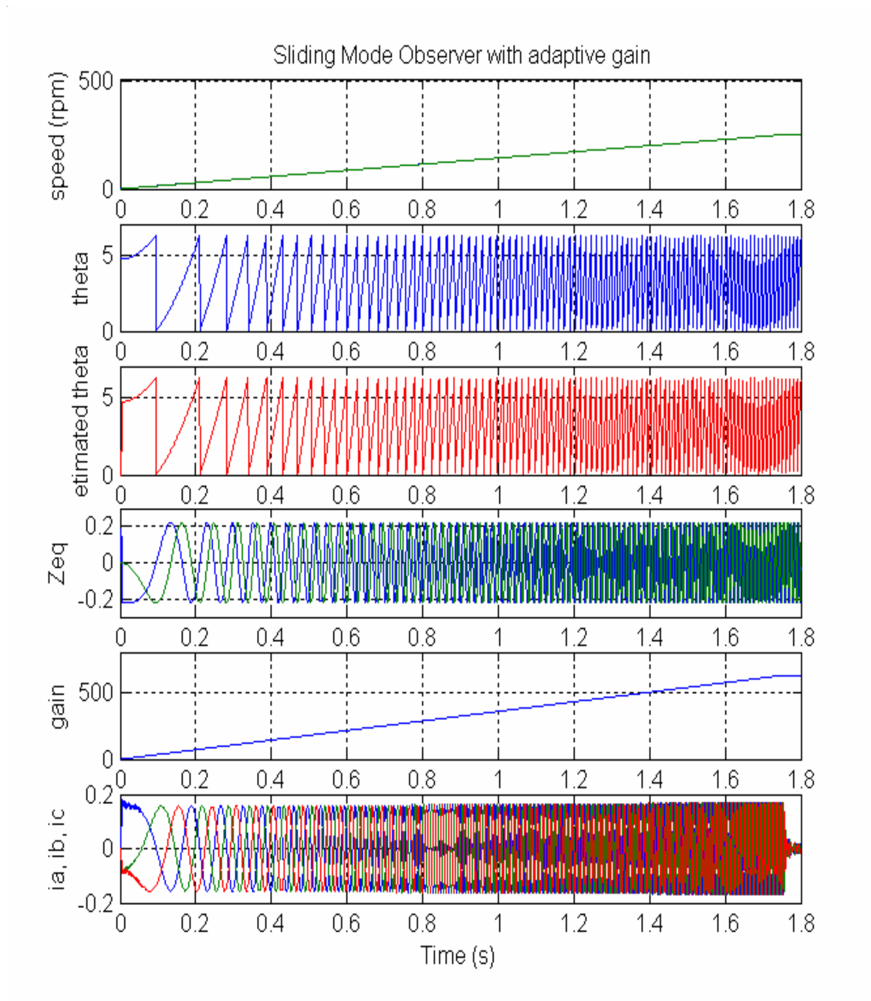

Figure 5.5: Simulation results of SMO with adaptive feedback gain: Rotor speed (top), real rotor position angle (2nd), estimated rotor position angle (3rd), equivalent control (4th), feedback gain (5th) and three phase currents (bottom).

5.6.2 Experimental results

The same experimental drive system as described in Chapter 4 has been set up to verify the effectiveness of the proposed sliding mode observer for the sensorless control of PMSM. In the tests, only the SPM motor was used as control target.

In Figures 5.6 through 5.10, the real rotor position angle $\theta_{encoder}$ is measured by an incremental encoder and the estimated one, $\hat{\theta}_{SMO}$, by the proposed sliding mode observer.

Figure 5.6 shows the experimental results when the motor is running at 50 rpm (about 20% base speed) with no load (i.e., 0 N.m) in (a) and a constant load of 10 N.m (30% allowable maximum torque) in (b). Figure 5.7 illustrates traces at 500 rpm (about 200% base speed) with no load in (a) and 2 N.m (30% maximum torque) in (b) and Figure 5.8 at 1,000 rpm (400% base speed) with no load in (a) and 1 N.m (50% maximum torque) in (b) respectively. We can observe the well-behaved rotor position estimation from the SMO and the well-regulated sinusoidal current waveforms. The estimated angle $\hat{\theta}_{SMO}$ aligns with $\theta_{encoder}$ well. It indicates that the proposed sliding mode observer works properly at different load levels and speeds covering full operating speed range. It is noticed that the monitoring rotor position signals output from the PWM-simulated D/A channels in Figure 5.7 and Figure 5.8 are rounded at the bottom corner due to the limited bandwidth of monitor circuits. More details of the measured and estimated rotor position angle have been recorded by real-time data logging algorithm with 20 kHz sampling rate as shown in Figure 5.9 and Figure 5.10.

Figure 5.9 and Figure 5.10 show the experimental results in per unit when the motor is running at 50 rpm with constant load of 10 N.m and at 1,000 rpm with 1 N.m respectively, under the same operating conditions as in the computer simulation, of which results are shown in Figure 5.4. For both cases, the actual and estimated rotor position angles are shown in (a), the error of estimated position angle in (b), the estimated back-EMF $e_{\alpha s}$ and $e_{\beta s}$ in (c), the sampled and estimated stator current $i_{\alpha s}$ in (d), and the current error in (e). It can be seen that the peak-to-peak value of estimation error of angle is less than 0.01 in per unit and the maximum current error less than 0.08. In the figures, 0.01 of angle error represents 3.6 electrical degree and 0.08 of current error represents 0.56 A. In addition, the angle displacement of about 10 degrees was observed at 50 rpm with large produced torque (10 N.m) but only 5 degree at 1,000 rpm with small torque (1 N.m). It is found to that the displacement results from the distortion of the rotor frame due to the torsion, which is relative to the torque produced on the rotor. At this point, it can be concluded that even with a high-resolution encoder, the "error of the estimated rotor position" would be large under heavy load condition in such kind of PMSM drive system, which is caused by the deformed rotor instead.

As seen, the estimated back-EMF waveforms of $e_{\alpha s}$ and $e_{\beta s}$ are so sinusoidal that the rotor position angle can be calculated accurately. Also, the estimated currents trace the sampled ones with minor errors according to the current level. The current error, reflecting the chattering in SMO, would be determined by the current level and settings of the saturation function.

Load test is carried out to investigate the dependency of SMO on load level. The experimental results shown in Figure 5.11 indicate the satisfactory position estimation by the proposed SMO and the resulting good current regulation under load conditions. Additionally, the effect of the feedback gain of equivalent control on the estimated angle can be sensed from Figure 5.11. It should be noted that, for the two estimated angle $\hat{\theta}_{SMO}$ and $\hat{\theta}'_{SMO}$, the system operating conditions including the cutting-off frequency of the low-pass filter in SMO are same in the tests except the feedback gain only.

Figure 5.12 shows the transient response when the motor is running at 50 rpm during step changes in load torque from zero to 10 N.m to zero. As observed, the speed is well regulated regardless of load disturbance.

In conclusion, the proposed siding mode observer works under load conditions within a wide speed range, i.e., from 50 rpm to 1,000 rpm with respect to the output fundamental frequency of 400 Hz. The experimental results match the simulation results mostly and demonstrate that the sliding mode observer is valid and the real-time implementation successful.

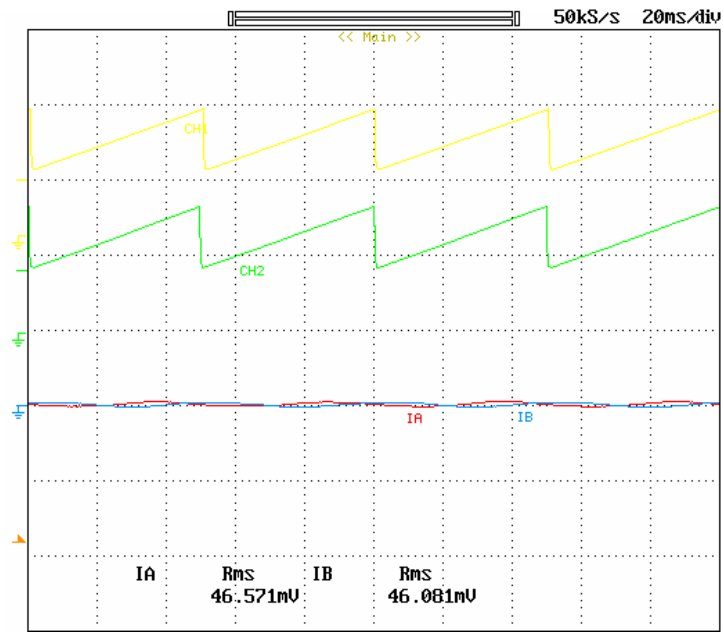

(a)

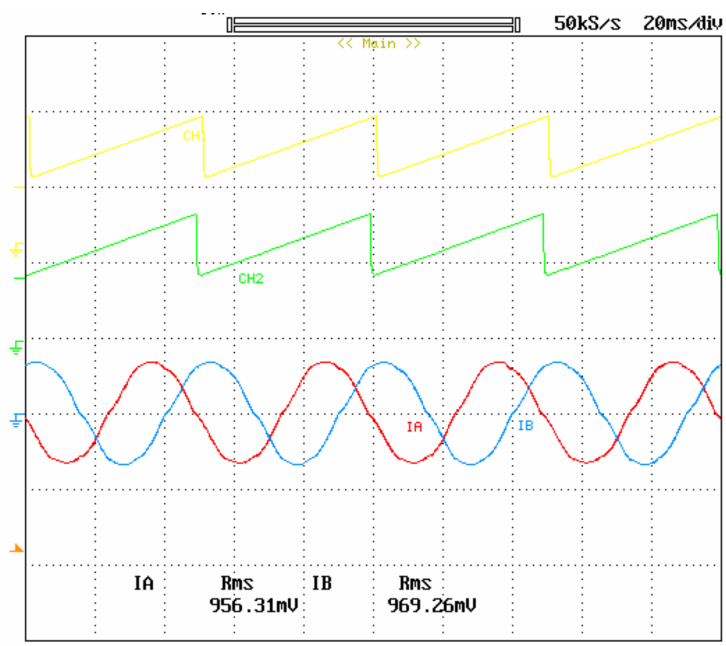

(b)

Figure 5.6: Rotor position angle $\theta_{encoder}$ (top), $\hat{\theta}_{SMO}$ (mid), i_{as} and i_{bs} (2.0 A/div, bottom) at 50 rpm: (a) 0 N.m, (b) 10 N.m.

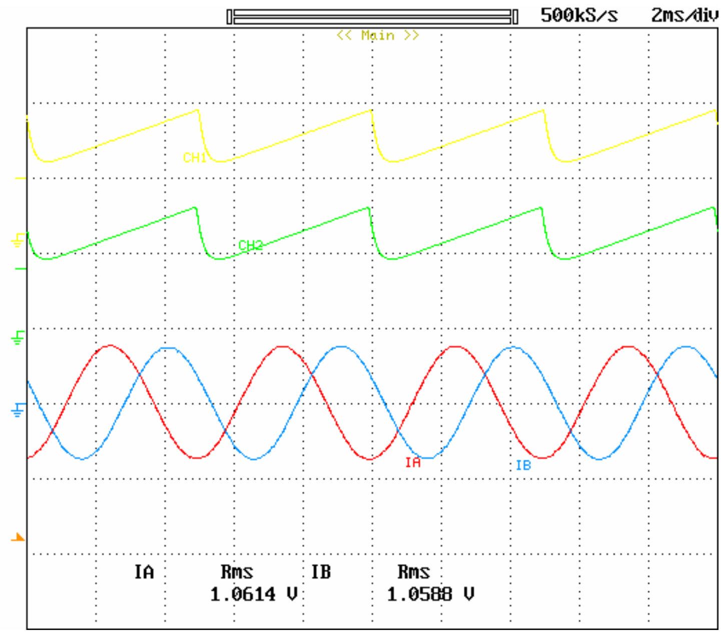

(a)

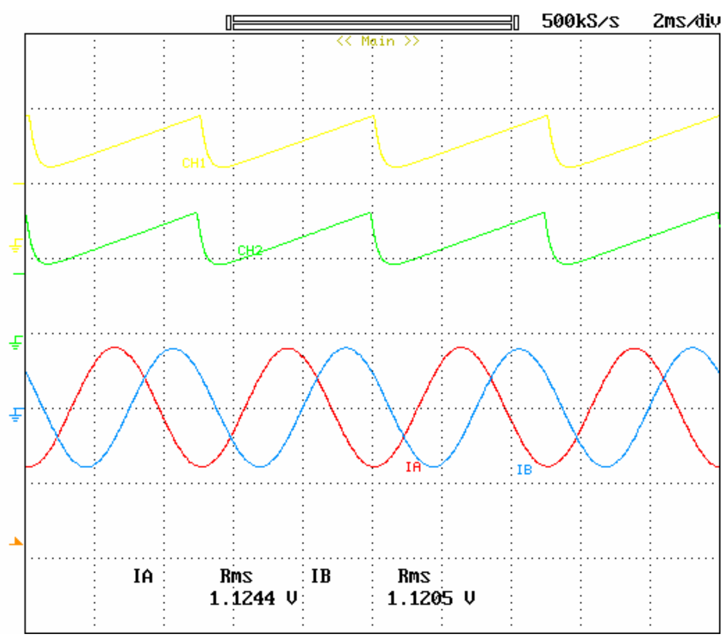

(b)

Figure 5.7: Rotor position angle $\theta_{encoder}$ (top), $\hat{\theta}_{SMO}$ (mid), i_{as} and i_{bs} (2.0 A/div, bottom) at 500 rpm: (a) 0 N.m, (b) 2 N.m.

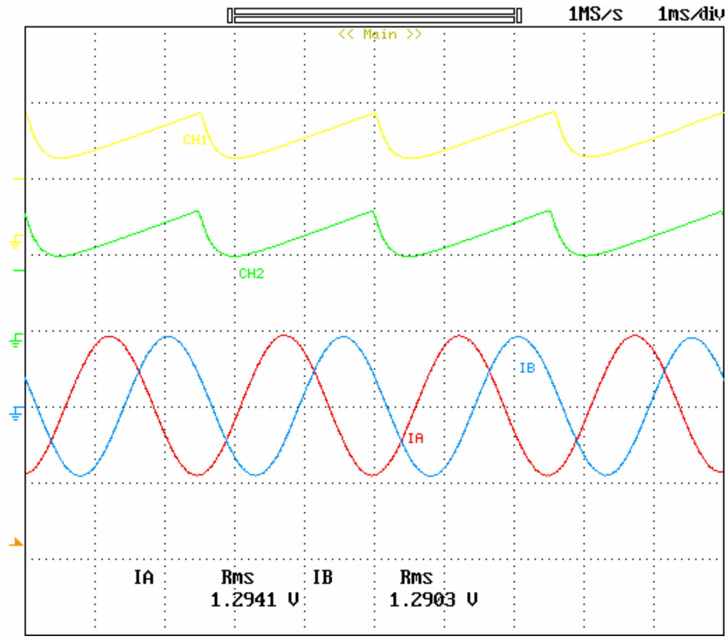

(a)

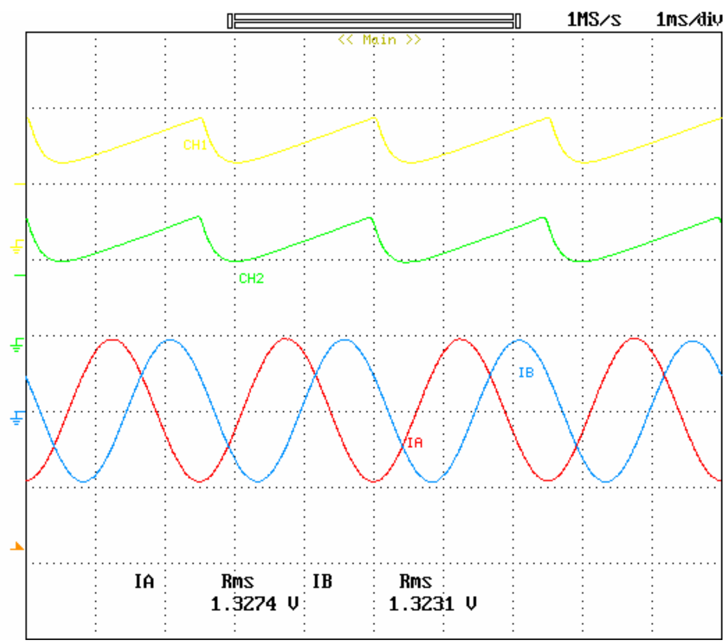

(b)

Figure 5.8: Rotor position angle $\theta_{encoder}$ (top), $\hat{\theta}_{SMO}$ (mid), i_{as} and i_{bs} (2.0 A/div, bottom) at 1,000 rpm: (a) 0 N.m, (b) 1 N.m.

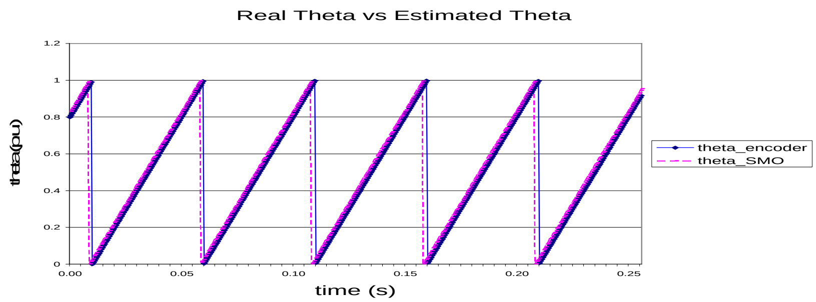

(a)

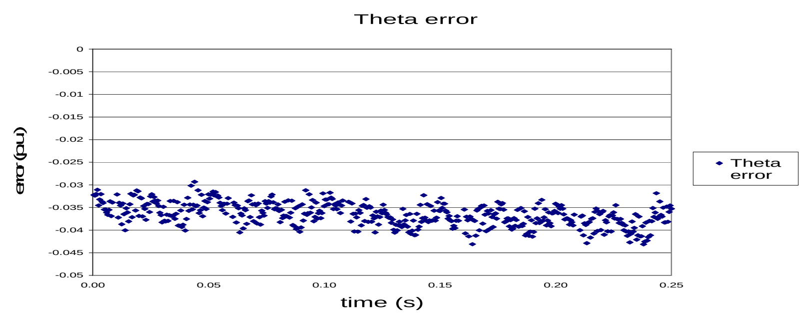

(b)

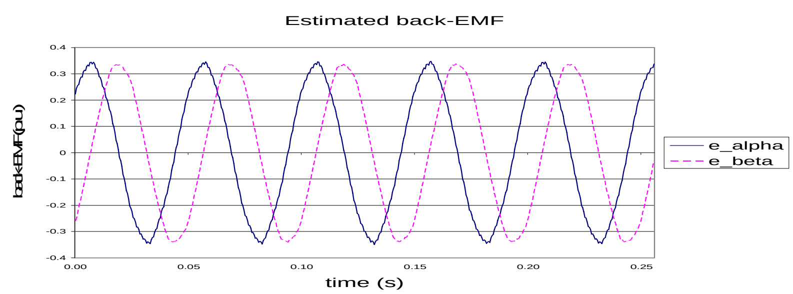

(c)

Figure 5.9: Experimental results of SMO at 50 rpm with 10-N.m load: (a) actual and estimated angle; (b) estimation error of angle; (c) estimated back-EMF; (d) sampled and estimated current i_{as}; (e) current error.

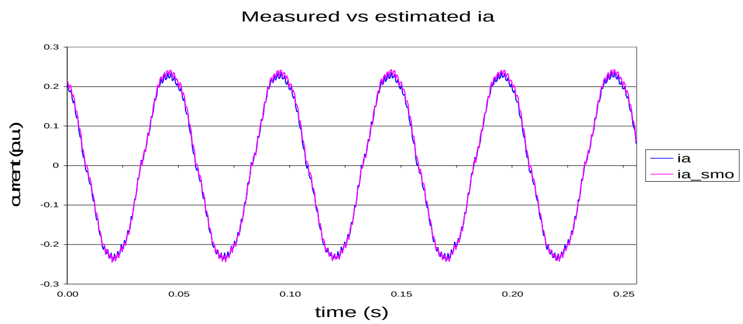

(d)

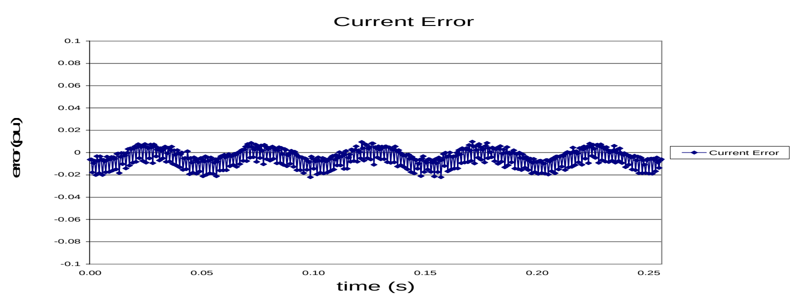

(e)

Figure 5.9: (continued) Experimental results of SMO at 50 rpm with 10-N.m load: (a) actual and estimated angle; (b) estimation error of angle; (c) estimated back-EMF; (d) sampled and estimated current i_{as}; (e) current error.

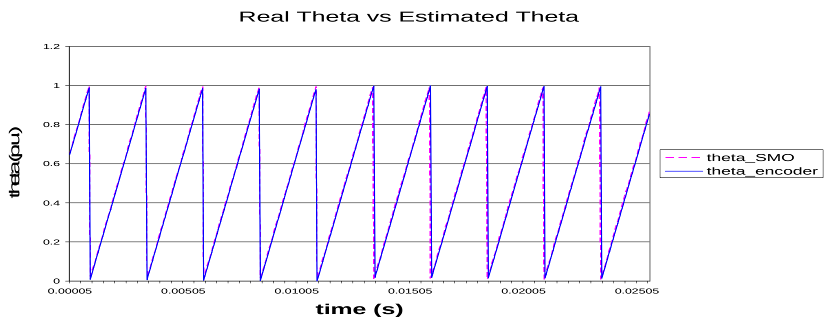

(a)

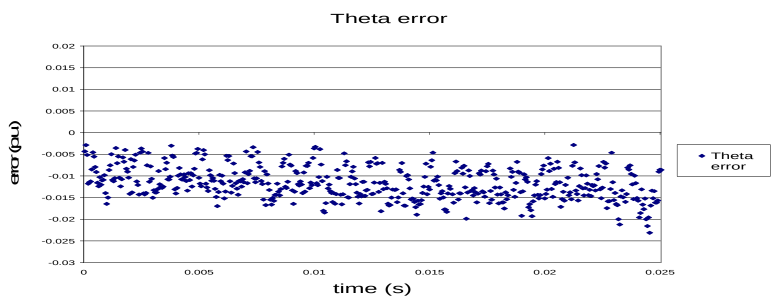

(b)

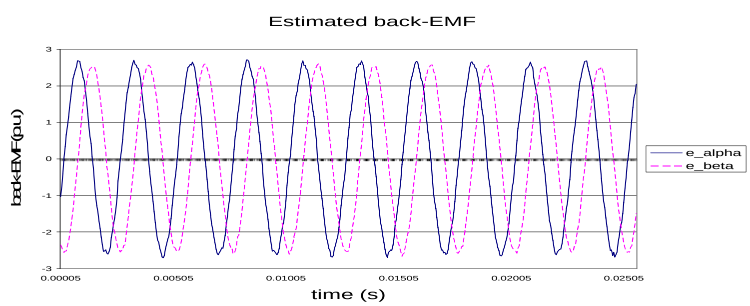

(c)

Figure 5.10: Experimental results of SMO at 1,000 rpm with 1-N.m load: (a) actual and estimated angle; (b) estimation error of angle; (c) estimated back-EMF; (d) sampled and estimated current i_{as}; (e) current error.

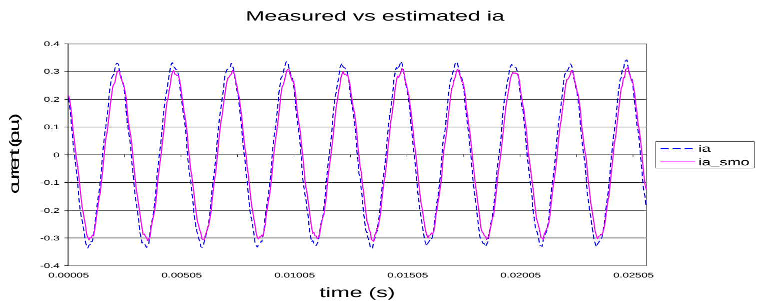

(d)

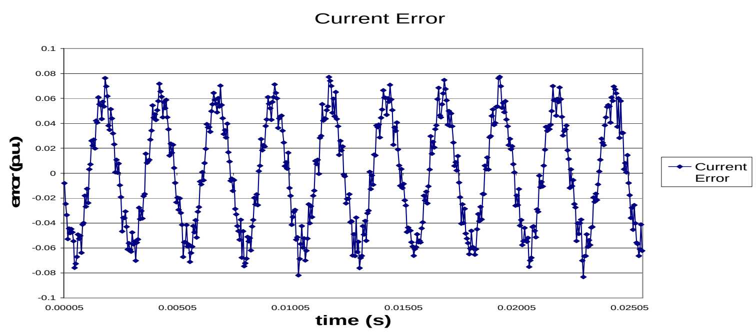

(e)

Figure 5.10: (continued) Experimental results of SMO at 1,000 rpm with 1-N.m load: (a) actual and estimated angle; (b) estimation error of angle; (c) estimated back-EMF; (d) sampled and estimated current i_{as}; (e) current error.

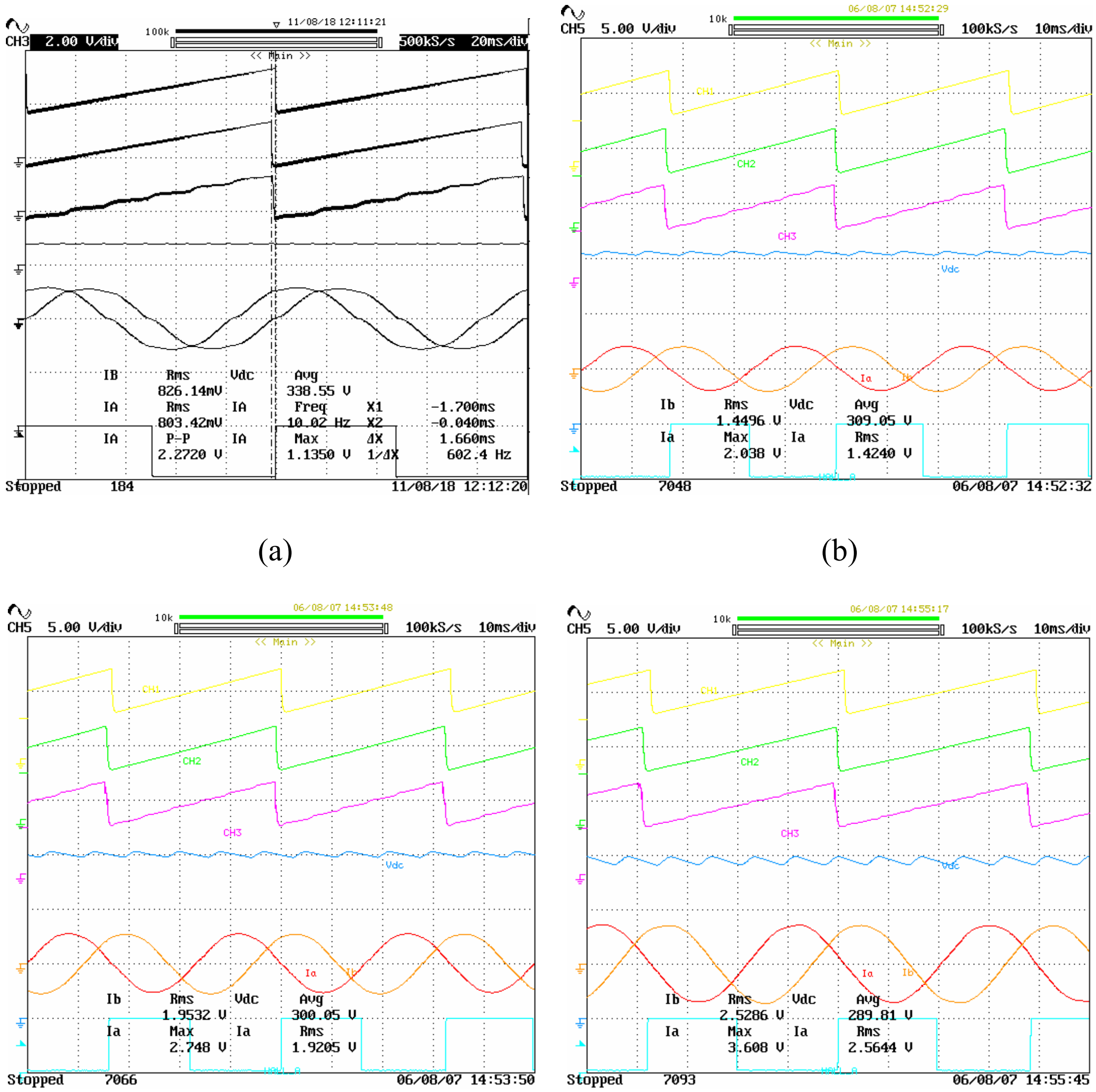

(a) (b)

(c) (d)

Figure 5.11: Experimental results of SMO under load conditions: Rotor position angle $\theta_{encoder}$ (top), $\hat{\theta}_{SMO}$ (l = -0.875, 2nd), $\hat{\theta}'_{SMO}$ (l = 0, 3rd), V_{dc} (100 V/div, 4th), i_{as} , i_{bs} (2.0 A/div in (a), 5.0 A/div in (b)-(d), 5th), and *Hall_A* (bottom): (a) 10-N.m load at 25 rpm, (b) 20-N.m load at 75 rpm, (c) 25-N.m load at 75 rpm, and (d) 30-N.m load at 65 rpm.

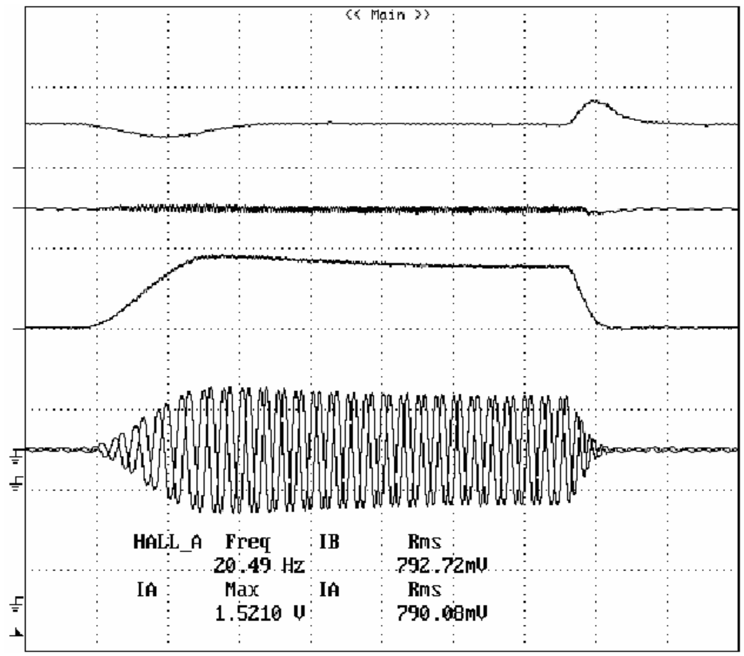

Figure 5.12: Dynamic performance of PMSM drive system during step changes in load torque: rotor speed $n_{encoder}$ (*95 pm/div*, top), i_{ds} (*1.7A/div*, 2nd), i_{qs} (*1.7A/div*, 3rd) and i_{as} and i_{bs} (2.0 A/div, bottom) 200ms/div

5.7 Summary

A sliding mode observer for position-sensorless control of PMSM has been developed. A concept of feedback of equivalent control is presented. By this approach, the sliding mode observer is able to work over wide speed range including flux-weakening region. Moreover, the flexibility to design the sliding mode observer is discussed, which benefits from the selection of equivalent control feedback gain. With the proposed sliding mode observer, the estimation error of rotor position angle can be reduced in both low-speed and high-speed range. The stability analysis of the SMO is conducted by a Lyapunov function and further convergence within the boundary layer is also proved.

In addition, in-depth design guidelines of the proposed sliding mode observer are given taking the performance of low-pass filter into consideration. The PMSM sensorless control drive system is also introduced, which employs the sliding mode observer for wide-speed operation.

It should be noticed that a sliding mode observer with adaptive gains to speed has been proposed. This observer provides a way to achieve rotor flux estimation as well as the rotor position. It is different from conventional back-EMF-based approaches and expected to bring new advantages to the sensorless control of PMSM.

Finally, the validity of the proposed observer has been demonstrated by both computer simulation and experimental results.

CHAPTER 6

CONCLUSIONS AND FUTURE WORK

6.1 Conclusions

This dissertation covers two major issues and solutions dealing with position sensorless vector control of permanent magnet synchronous machines (PMSM) over wide speed range including flux-weakening region. Two related control techniques have been extensively studied and the following conclusions can be drawn upon the fulfillment of the dissertation research:

- A robust flux-weakening control scheme of PMSM is proposed. With the current control strategy, i.e., adjusting the direct-axis voltage but fixing the applied quadrature-axis voltage of PMSM at a specific value, the demagnetizing stator current for the flux-weakening operation can be automatically generated based on the inherent cross-coupling effects in PMSM. The developed speed/flux-weakening controller is able to achieve both flux-weakening and speed control simultaneously without the knowledge of accurate machine parameters and dc bus voltage of power inverter.

Moreover, no saturation of current regulators occurs under any load conditions, resulting in control robustness in the flux-weakening region.

- A sliding mode observer has been developed for the estimation of rotor position angle in the position-sensorless vector control of PMSM without saliency. A concept of feedback of equivalent control is applied to extend the operating range of sliding mode observer and improve its estimation performance. Compared to conventional sliding mode observers, the proposed one features the flexibility to design parameters of sliding mode observer with wide operating speed range.
- Other contributions in this dissertation include: 1) applying graphic method to analyze and design the flux-weakening control of PMSM, 2) a flux-based sliding mode observer with adaptive feedback gain, 3) modeling and operation analysis of PMSM with comparison in two categories: surface-mounted permanent-magnet motors (SPM) and interior permanent-magnet motors (IPM).

6.2 Future Work

Future research may be of interest concentrating on the following:

- Develop a sliding mode observer for IPM motors based on the concept of feedback of equivalent control.
- Explore the possibility of extending the proposed SMO model to IPM drives.

- Develop transition control for smooth switching between constant-torque and constant-power operation of PMSM.
- Investigate the performance dependency of SWFC on the parameters of PMSM.
- Comprehensive trade-off study on the selection of the voltage constant for various optimal goals of PMSM drives.
- Investigate the effects of saturation of magnetic circuits on the flux-weakening operation of PMSM and its control.

REFERENCES

[1] Peter Vas, *Sensorless and Direct Torque Control*, 1st Edition, Oxford University Press, 1998.

[2] Vadim Utkin, J. Guldner and Jingxin Shi, *Sliding Mode Control in Electromechanical Systems*, 1st Edition, Taylor & Francis, Philadelphia, 1999.

[3] B. K. Bose, "Power electronics and motion control—Technology status and recent trends," *IEEE Trans. Ind. Applicat.*, vol. 29, pp. 902–909, Sept. /Oct., 1993.

[4] T. A. Lipo, "Recent progress in the development of solid state ac motor drives," *IEEE Trans. Power Electron.,* vol. 3, pp. 105-117, April, 1988.

[5] W. Leonhard, "Adjustable speed ac drives," *Proceedings of IEEE,* vol. 76, pp. 455-471, April, 1988.

[6] B. K. Bose, "Variable frequency drives-technology and applications," *in Proc. ISIE 93(Budapest),* June, 1993, pp 1-18.

[7] B. K. Bose, "Power electronics-an emerging technology," *IEEE Trans. Ind. Elec.,* vol. 36, No. 3, pp. 403-41, Aug. 1989.

[8] R. Gabriel, W. Leonhard, and C. Nordby, "Field oriented control of standard AC motor using microprocessor," *IEEE Trans. Ind. Applicat.,* vol. IA-16, pp. 186–192, 1980.

[9] L. Harnefors, "Design and analysis of general rotor-flux oriented vector control systems," *IEEE Trans. Ind. Electron.,* vol. 48, pp. 383–389, Apr. 2001.

[10] M. Schroedl, "Sensorless control of AC machines at low speed and standstill based on the "INFORM" method," in *Conf. Rec. IEEE-IAS Annu. Meeting,* vol. 1, 1996, pp. 270–277.

[11] P. L. Jansen and R. D. Lorentz, "Transducerless position and velocity estimation in induction and salient AC machines," *IEEE Trans. Ind. Applicat.,* vol. 31, pp. 240–247, Mar./Apr. 1995.

[12] P. L. Jansen, R. D. Lorenz, and D. W. Novotny, "Observer-based direct field orientation: Analysis and comparison of alternative methods," *IEEE Trans. Ind. Applicat.,* vol. 30, pp. 945–953, July/Aug. 1994.

[13] T. M. Jahns and V. Blasko, "Recent advances in power electronics technology for industrial and traction machine drives," *Proc. IEEE*, vol. 89, pp. 963–975, June 2001.

[14] Thomas M. Jahns, "Motion control with permanent-magnet ac machines," in *Proc. IEEE,* vol. 82, Aug. 1994, pp. 1241-1252.

[15] T. M. Jahns "Flux-weakening regiem operation of an interior permanent-magnet synchronous motor drives," *IEEE Trans. Ind. Applicat.,* vol. IA-23, pp. 681-689, July/Aug. 1987.

[16] B. Sneyers, D. W. Novotny and T. A. Lipo, "Field weakening in buried permanent magnet ac motor drives," *IEEE Trans. Ind. Applicat.,* vol. IA-21, pp. 398-407, Mar./Apr. 1991.

[17] T. M. Jahns, G. B. Kliman and T. W. Neumann, "Interior permanent-magnet synchronous motors for adjustable-speed drive," *IEEE Trans. Ind. Applicat.,* vol. IA-22, pp. 738-747, July/Aug. 1986.

[18] L. Xu, L. Ye, L. Zhen and A. El-Antably, "A new design concept of permanent magnet machine for flux weakening operation," *IEEE Trans. Ind. Applicat.,* vol. 31, pp. 373-378, March/April, 1995.

[19] J. A. Tapia, F. Leonardi, and T. A. Lipo, "Consequent-pole permanent-magnet machine with extended field-weakening capability," *IEEE Trans. Ind. Applicat.,* vol. 39, pp. 1704-1709, Nov./Dec., 2003.

[20] W. L. Soong and T. J. Miller, "Field-weakening performance of brushless synchronous AC motor drives," *Proc. IEE—Elect. Power Applicat.*, vol. 141, no. 6, pp. 331–340, Nov. 1994.

[21] S. R. Macminn and T. M. Jahns, "Control techniques for improved high-speed performance of interior PM synchronous motor drives," *IEEE Trans. Ind. Applicat.,* vol. 2, pp. 997-1004, Sept./Oct. 1991.

[22] T. Sebastian and G. R. Slemon, "Operating limits of inverter-driven permanent magnet motor drives," *IEEE* CH2272-3/86, pp. 800-805, 1986.

[23] R. Dhaouadi and N. Mohan, "Analysis of current-regulated voltage-source inverters for permanent magnet synchronous motor drives in normal and extended speed ranges," *IEEE Trans. Energy Conv.,* vol. 5, pp. 137-144, Mar. 1990.

[24] S. Morimoto, M. Sanada and K. Takeda, "Wide-speed operation of interior permanent magnet synchronous motors with high-performance current regulator," *IEEE Trans. Ind. Applicat.,* vol. 30, pp. 920-926, July/Aug. 1994.

[25] S. Morimoto, Y. Takeda, T. Hirasa, and K. Taniguchi, "Expansion of operating limits for permanent magnet by current vector control considering inverter capacity," *IEEE Trans. Ind. Applicat.*, vol. 26, pp. 866-871, Sept./Oct. 1990.

[26] S. D. Sudhoff, K. A. Corzine and H. J. Hegner, "A flux-weakening strategy for current-regulated surface-mounted permanent-magnet machine drives," *IEEE Trans. Energy Conv.,* vol. 10, pp. 431-437, Sept. 1995.

[27] Y. Sozer and D. A. Torrey, "Adaptive Flux weakening control of permanent magnet synchronous motors," in *Conf. Rec. IEEE-IAS Annu. Meeting*, vol. 1, St. Louis, MO, 1998, pp. 475–482.

[28] Y. S. Kim, Y. K. Choi and J. H. Lee, "Speed-sensorless vector control for permanent-magnet synchronous motors based on instantaneous reactive power in the wide-speed region," *IEE Proc-Electr. Power Appl.,* vol. 152, No. 5, pp. 1343-1349, Sept. 2005.

[29] J. M. Kim and S. K. Sul, "Speed control of interior permanent magnet synchronous motor drive for the flux weakening operation," *IEEE Trans. Ind. Applicat.,* vol. 33, pp. 43-48, Jan./Feb. 1997.

[30] J. H. Song, J. M. Kim, and S. K. Sul, "A new robust SPMSM control to parameter variations in flux weakening region," *IEEE IECON*, vol. 2, pp. 1193-1198, 1996.

[31] J. J. Chen and K. P. Chin, "Automatic flux-weakening control of permanent magnet synchronous motors using a reduced-order controller," *IEEE Trans. Power Electron.*, vol. 15, pp. 881-890, Sept. 2000.

[32] R. Wu, et al., "Permanent magnet motor drive without a shaft sensor," *IEEE Trans. Ind. Applicat.*, vol. 27, pp. 1005-1011, Sept./Oct. 1991.

[33] L. Xu and C. Wang, "Implementation and experimental investigation of sensorless control schemes for PMSM in super-high variable speed operation," in *Conf. Rec. IEEE-IAS Annu. Meeting*, vol. 1, 1998, pp. 483–489.

[34] M. Schroedl, "Sensorless control of AC machines at low speed and standatill based on the "INFORM" method," in *Conf. Rec. IEEE-IAS Annu. Meeting*, vol. 1, 1996, pp. 270-277.

[35] M. J. Corley and R. D. Lorenz, "Rotor position and velocity estimation for permanent magnet synchronous machine at standstill and high speed," in *Conf. Rec. IEEE-IAS Annu. Meeting*, vol. 1, 1996, pp. 36-41.

[36] R. Mizutani, T. Takeshita and N. Matsui, “Current model-based sensorless drives of salient-pole PMSM at low speed and standstill,” *IEEE Trans. Ind. Applicat.*, vol. 34, pp. 841-846, July/August, 1998.

[37] A. Consoli, G. Scarcella and A. Testa, “Industry application of zero-speed sensorless control techniques for PM synchronous motors,” *IEEE Trans. Ind. Applicat.*, vol. 37, pp. 513-521, March/April, 2001.

[38] M. Tursini, R. Petrella and F. Parasiliti, “Initial rotor position estimation method for PM motors,” *IEEE Trans. Ind. Applicat.*, vol. 39, pp. 1630-1640, Nov./Dec., 2003.

[39] J. Jang, S. Sul, J. Ha and et al, “Sensorless drive of surface-mounted permanent-magnet motor by high-frequency signal injection based on magnetic saliency,” *IEEE Trans. Ind. Applicat.*, vol. 39, pp. 1031-1039, July/August, 2003.

[40] J. Jang, J. Ha and A. Testa, “Analysis of permanent-magnet machine for sensorless control based on high-frequency signal injection,” *IEEE Trans. Ind. Applicat.*, vol. 40, pp. 1595-1603, Nov./Dec., 2004.

[41] K. W. Lim, K. S. Low and M. F. Rahman, “A position observer for permanent magnet synchronous motor drive,” *IECON Annu. ConferenceRecord* , pp. 1004–1008, 1994.

[42] J. S. Kim and S. K. Sul, “High performance PMSM drives without rotational position sensors using reduced order observer,” in *Proc. Conf. IEEE IAS Annu. Meeting*, 1995, pp. 75–82.

[43] J. Kim and S. Sul, “New approach for high-performance PMSM drives without rotational position sensors,” *IEEE Trans. Power Electron.*, vol. 12, pp. 904–911, Sept. 1997.

[44] G. Zhu, A. Kaddouri, and et al, “Nonlinear state observer for the sensorless control of a permanent-magnet AC machine,” *IEEE Trans. Ind. Electron.*, vol. 48, pp. 1098-1108, Dec. 2001.

[45] Y. Yamamoto, Y. Yoshida and T. Ashikaga, “Sensorless control of PM motor using full order flux observer,” *IEEJ Trans. Ind. Applt.*, vol. 124, pp. 743-749, Aug. 2004.

[46] S. Shinnaka, “New “D-state-observer”-based vector control for sensorless drive of permanent-magnet synchronous motors,” *IEEE Trans. Ind. Applicat.*, vol. 41, pp. 825-833, May./June. 2005.

[47] R. Dhaouadi, N. Mohan, and L. Norum, “Design and implementation of an extended Kalman filter for the state estimation of a permanent magnet synchronous motor,” *IEEE Trans. Power Electron.*, vol. 6, pp. 491–497, July 1991.

[48] S. Bolognani, R. Oboe, and M. Ziglitto, “Sensorless full-digital PMSM drive with EKF estimation of speed and rotor position,” *IEEE Trans. Ind. Electron.*, vol. 46, pp. 184–191, Feb. 1999.

[49] A. Qiu and B. Wu, “Sensorless control of permanent magnet synchronous motor using extended Kalman filter,” in *Proc. Conf. Of CCECE 2004,* Niagara Falls, pp. 1557-1562.

[50] E. Cerruto, A. Consoli, A. Raciti, and A. Testa, “A robust adaptive controller for PM motor drives in robotic applications,” *IEEE Trans. Power Electron.*, vol. 10, pp. 62-71, Jan. 1995.

[51] K. J. Åström and B. Wittenmark, “A survey of adaptive control applications,” in *Proc. 34th IEEE Conf. Decision and Control* New Orleans, LA, 1995, pp. 649-654.

[52] F. J. Lin and S. L. Chiu, “Adaptive fuzzy sliding mode control for PM synchronous servo motor drives,” *Proc. IEE—Contr. Theory Applicat.*, vol. 145, no. 1, pp. 63–72, 1998.

[53] I. C. Baik, K. H. Kim, and M. J. Youn, “Robust nonlinear speed control of PM synchronous motor using adaptive and sliding mode control techniques,” *Proc. IEE—Elect. Power Applicat.*, vol. 145, no. 4, pp. 369–376, 1998.

[54] T. Furuhashi, et al., “Position-and-velocity sensorless control for brushless DC motors using an adaptive sliding mode observer,” *IEEE Trans. Ind. Electrons*, vol. 39, pp. 89-95, April, 1992.

[55] V. I. Utkin, “Sliding mode control design principles and applications to electric drives,” *IEEE Trans. Ind. Electron., vol.* 40, pp. 23–36, Feb. 1993.

[56] Z. M. Peixoto, et al., “Speed control of permanent magnet motors using sliding mode observers for induced emf, position and speed estimation,” in *Conf. Rec. IEEE-IAS Annu. Meeting*, vol. 2, 1995, pp. 1023–1028.

[57] Y. S. Han, J. S. Choi and Y.S. Kim, “Sensorless PMSM drive with a sliding mode control based adaptive speed and stator resistance estimator,” *IEEE Trans. Magnetics,* vol. 36, pp. 3588-3591, Sept. 2000.

[58] Z. Yan, C. Jin, and V. I. Utkin, “Sensorless sliding-mode control of induction motors,” *IEEE Trans. Ind. Electron., vol.* 47, pp. 1286–1297, Dec. 2000.

[59] R. G. Berstecher, R. palm and H. D. Unbehauen, “An adaptive fuzzy sliding mode controller,” *IEEE Trans. Power Electron.*, vol. 48, pp. 18-31, 2001.

[60] C. Li and M. Elbuluk, “A sliding mode observer for sensorless control of permanent magnet synchronous motors,” in *Conf. Rec. IEEE-IAS Annu. Meeting*, vol. 2, 2001, pp. 1273–1278.

[61] Z. Yan and V. Utkin, "Sliding mode observers for electric machines-an overview," in *Conf. Rec. IEEE-IES 28th Annu. Meeting IECON02*, vol. 3, 2002, pp. 1842–1847.

[62] M. Elbuluk and C. Li, "Sliding mode observer for wide-speed sensorless control of PMSM drives," in *Conf. Rec. IEEE-IAS Annu. Meeting*, vol. 1, 2003, pp. 480–485.

[63] K. Kang, J. Kim and et al, "Sensorless control of PMSM in high speed range with iterative sliding mode observer," in *Conf. Rec.IEEE- APEC'04*, vol. 2, 2004, pp. 1111–1116.

[64] D. Schroëder, C. Schäffner, and U. Lenz, "Neural-net based observers for sensorless drives," in *Proc. 20th Int. Conf. Industrial Electronics Control and Instrumentation (IECON'94)*, vol. 3, Bologna, Italy, 1994, pp. 1599–1610.

[65] T. L. Hsien, Y. Y. Sun and M. C. Tsai, "H^{∞} control for sensorless permanent-magnet synchronous drive," *IEE Proc. Electr. Power Appl.* Vol. 144, No. 3, pp. 173-181, May, 1997.

[66] Y. Yi, D. M. Vilathgamuwa, and M. A. Rahman, "Implementation of an artificial-neural-network-based real-time adaptive controller for an interior permanent-magnet motor drive," *IEEE Trans. Ind. Appl.*, vol. 39, no. 1, pp. 96-104, Jan./Feb. 2003.

[67] Paul C. Krause, Oleg Wasynczuk and Scott D. Sudhoff, *Analysis of Electric Machinery*, IEEE Press, Inc. New York, 1986.

[68] D. W. Novotny and T. A. Lipo, *Vector Control and Dynamics of AC Drives*, Clarendon Press, Oxford, 1996.

[69] M. J. Corley and R. D. Lorenz, "Rotor position and velocity estimation for a salient-pole permanent magnet synchronous machine at standstill and high speeds," *IEEE Trans. Ind. Appl.*, vol. 34, no. 4, pp. 784–789, Jul./Aug. 1998.

[70] E. C. Lovelace, T. M. Jahns, and J. H. Lang, "Impact of saturation and inverter cost on interior PM synchronous machine drive optimization," *IEEE Trans. Ind. Appl.*, vol. 36, no. 3, pp. 723–729, May/June, 2000.

[71] R. Wu and G. R. Slemon, "A permanent magnet motor drive without a shaft sensor," *IEEE Trans. Ind. Applicat.*, vol. 27, pp. 1005–1011, Oct. 1991.

[72] A. M. EL-Refaie, and T. M. Jahns, "Scalability of surface PM machines with concentrated windings designed to achieve wide speed ranges of constant-power operation," *IEEE Trans. power Conversion*, vol. 21, no. 2, pp. 362–369, June, 2006.

[73] A. M. EL-Refaie, T. M. Jahns and D. W. Novotny, "Analysis of surface permanent magnet machines with fractional-slot concentrated windings," *IEEE Trans. Eng. Conversion*, vol. 21, no. 1, pp. 34–43, March, 2006.

[74] A. M. EL-Refaie, and T. M. Jahns, "Optimal flux weakening in surface PM machines using fractional-slot concentrated windings," *IEEE Trans. Ind. Applicat.*, vol. 41, no.3, pp. 790–800, May/June, 2005.

[75] Zoran Mihailovic, *Modelling and Control Design of VSI-Fed PMSM Drive Systems with Active Load*, MS thesis, Viginia Polytechnic Institute and State University, 1998.

APPENDIX A

SIMULATION MODELS

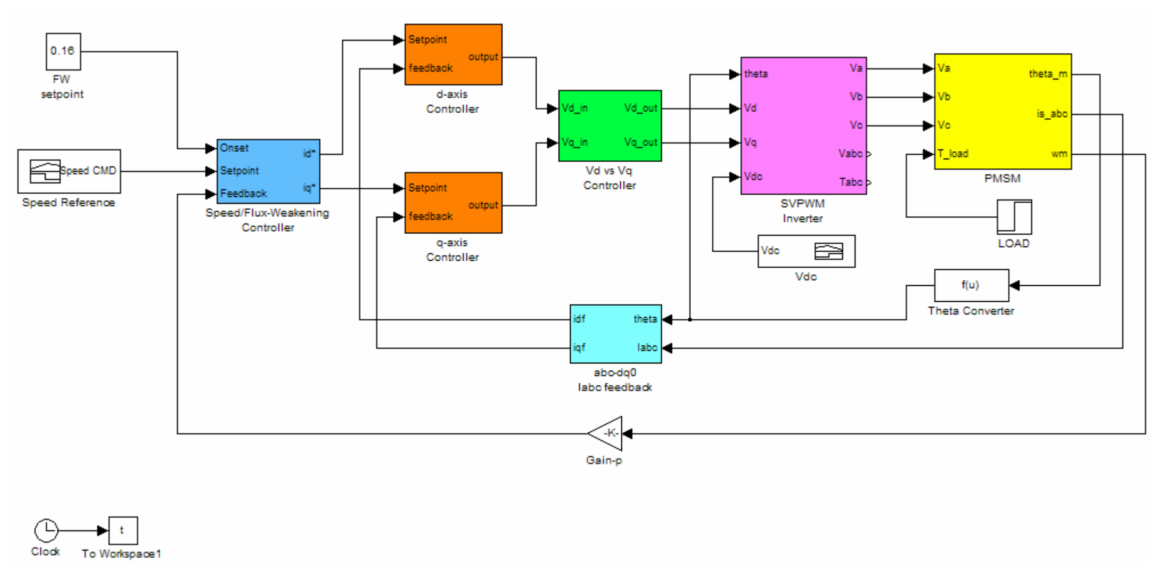

Figure A.1: Simulink model of PMSM drive system with Speed/Flux-Weakening Controller.

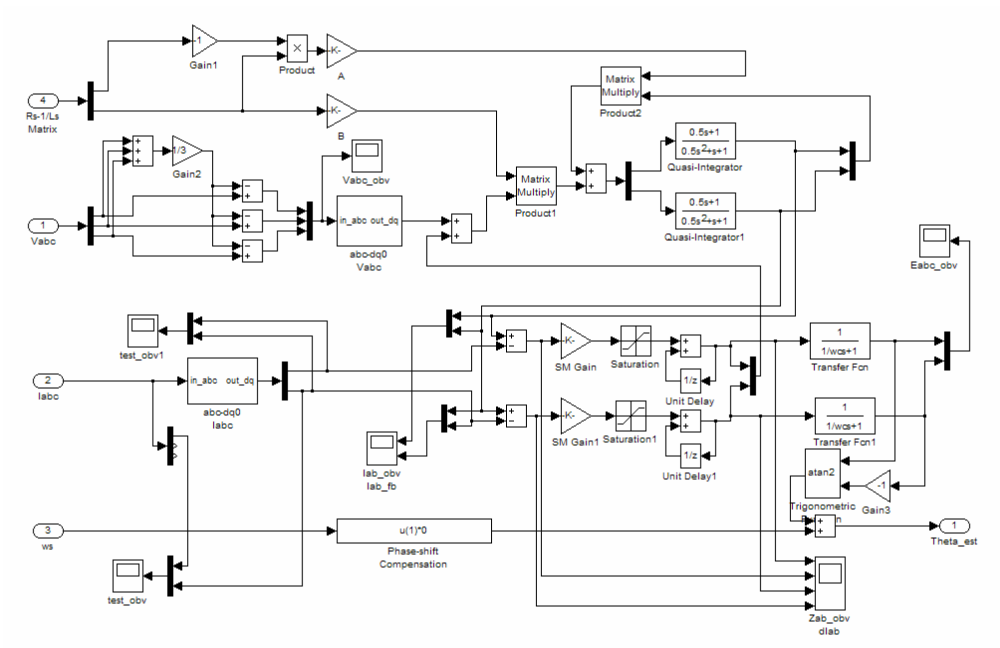

Figure A.2: Simulink model of the proposed sliding mode observer.

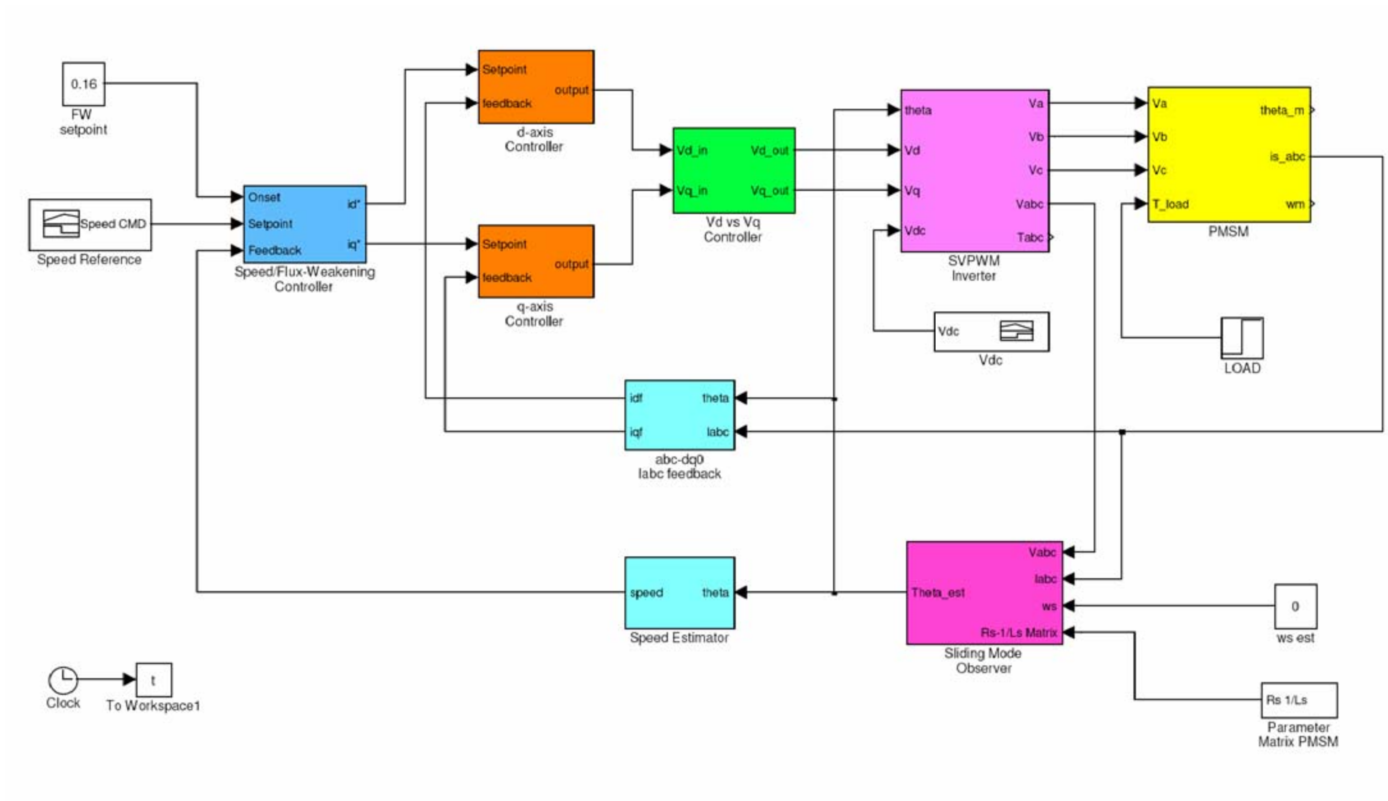

Figure A.3: Simulink model of the PMSM drive system with the proposed sliding mode observer.

APPENDIX B

EXPERIMENTAL SETUP

Precise load torque can be added by a MAGTROL hysteresis dynamometer, DSP6500. The input power and the efficiency of PMSM are measured by a power analyzer. The developed control algorithms are implemented in a 32-bit fixed-point DSP, Texas Instruments TMS320F2812, which has following characteristics:

- High-Performance Static CMOS Technology, 150 MHz (6.67-ns Cycle Time);
- High-Performance 32-Bit CPU;
- Flash Devices: Up to 128K x 16 Flash; and
- Analog-to-Digital Converter: 12-Bit, 200-ns conversion time per channel, 16 channels.

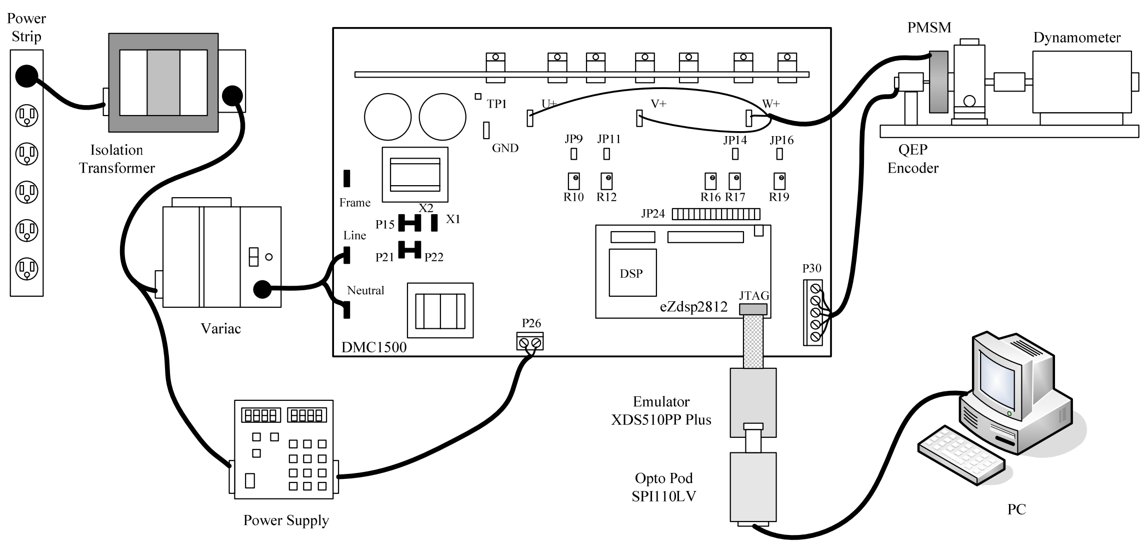

Figure B.1: Experimental setup and connection sketch.

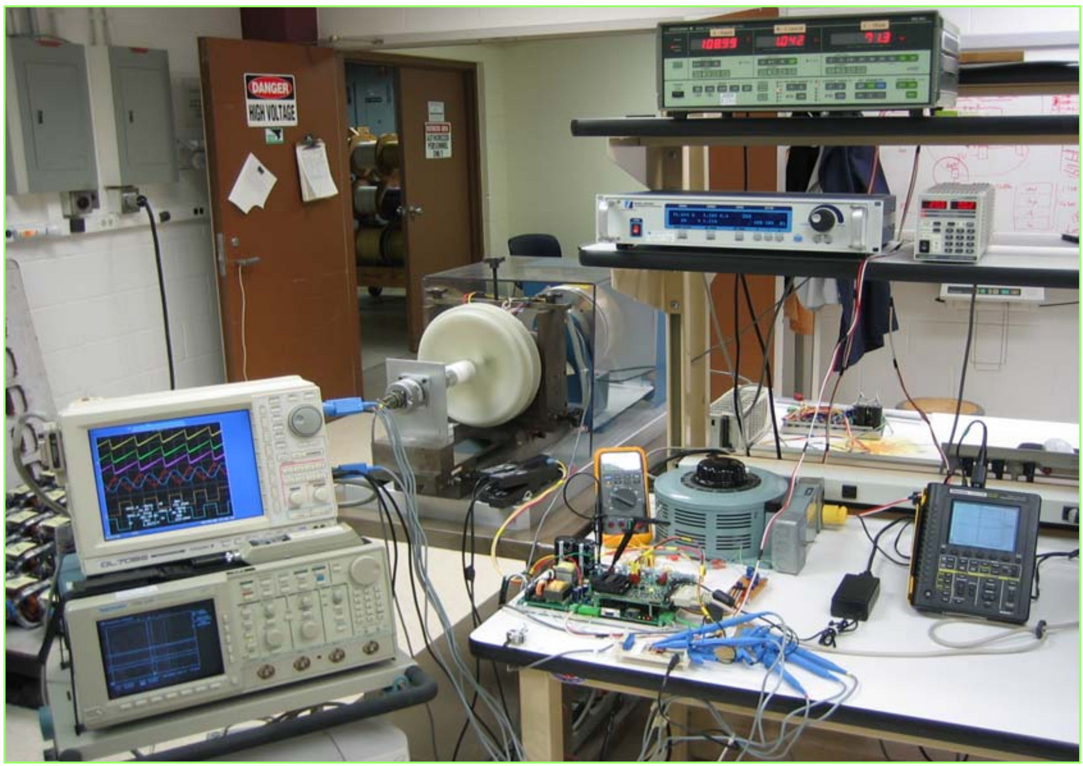

Figure B.2: Courtesy photo of bench setup.